

# **MICROMAGNETIC MODELLING OF THIN FILM MEDIA**

by

**Rita Maqsooda Ahmed**

**A thesis submitted in partial fulfilment of the requirements of the University of  
Central Lancashire for the degree of Doctor of Philosophy**

at

**Centre for Materials Science  
University of Central Lancashire**

**January 2001**

**Director of Studies**

**Dr. D. A. Parker**

# Abstract

The magnetic recording industry is continuously trying to increase the density of recording media. There is a continuous need, therefore, to fully understand the magnetic processes that occur in such media. To enable this understanding, theoretical studies are conducted in the form of micromagnetic modelling. This thesis is concerned with the micromagnetic modelling of thin film media. Experiments have shown that thin film media consists of closely packed, irregularly shaped grains with non-magnetic boundaries.

To simulate a model of the physical structure, the Voronoi Construction Technique was implemented to give the required irregular structure. The grains were assumed to have uniaxial anisotropy and the magnetisation within the grain was assumed to vary throughout. To achieve non-uniformity, the grains were divided into triangles and the magnetisation within each triangle was assumed to vary linearly. The effect on the magnetisation within the grains due to the influences from an externally applied field, an anisotropy field, a magnetostatic field and an exchange field was observed. The motion of the magnetic moments under these influences was modelled by the Landau-Lifshitz equation.

The most time consuming calculation in the modelling process is the magnetostatic field calculation. Therefore, continuous research into more efficient methods of calculating this field is carried out. The model initially uses a dipole approximation to calculate the total contribution from the magnetostatic field. A more accurate magnetostatic calculation, based on volume and surface charges of the triangles, was implemented to calculate the close range magnetostatic effects. The integrals were found to have singularities when the point of evaluation lay on one of the vertices of a triangle to be integrated. The Shift Method was introduced to overcome the problem which translated the problem vertex slightly away from the point of evaluation.

Vast differences in the hysteresis loops when using the two methods of calculating the magnetostatic field were seen. The dipole approximation appeared to be too inaccurate in calculating the magnetostatic field. With the introduction of the more accurate method, the model compared well against previous findings.

# Table of Contents

<b>1.</b>	<b>Introduction</b>	<b>1</b>
1.1	Introduction to Magnetism	1
1.2	Magnetic Recording	2
1.3	Overview of the Thesis	4
<b>2.</b>	<b>Thin Film Media</b>	<b>7</b>
2.1	Introduction	7
2.2	Manufacture of Thin Film Media	7
2.3	Microstructure of Thin Film Media	10
2.4	Characteristics of Thin Film Media	11
	2.4.1 Weiss's Theory	12
	2.4.2 The Demagnetising Field	14
2.5	Previous Work on Thin Film Media	16
<b>3.</b>	<b>Micromagnetic Modelling of the Thin Film</b>	<b>19</b>
3.1	Introduction	19
3.2	Generating the Physical Structure of Thin Film Media	20
	3.2.1 Definition of a Voronoi Diagram	21

3.2.2	The Voronoi Construction	21
<b>3.3</b>	<b>The Hysteresis Loop</b>	<b>25</b>
<b>3.4</b>	<b>Calculating the Total Effective Field</b>	<b>27</b>
3.4.1	The Anisotropy Field	29
3.4.2	The External Field	35
3.4.3	The Exchange Field	36
3.4.4	The Magnetostatic Field	38
<b>3.5</b>	<b>Modelling the Motion of the Magnetic Moment</b>	<b>38</b>
3.5.1	Solving The Landau Lifshitz Equation	41
<b>3.6</b>	<b>Summary</b>	<b>44</b>
<b>4.</b>	<b>Calculating the Magnetostatic Field</b>	<b>45</b>
<b>4.1</b>	<b>Introduction</b>	<b>45</b>
<b>4.2</b>	<b>Dipole Approximation</b>	<b>46</b>
<b>4.3</b>	<b>Exact Calculation</b>	<b>50</b>
4.3.1	Evaluating the Surface Integral	52
4.3.2	Evaluating the Line Integral	58
4.3.3	Incorporating the magnetostatic calculation into the model	64
4.3.4	Problems with the exact calculation	65
4.3.5	The Shift Method	68
<b>4.4</b>	<b>Summary</b>	<b>69</b>

<b>5.</b>	<b>Results</b>	<b>70</b>
<b>5.1</b>	<b>Introduction</b>	<b>70</b>
<b>5.2</b>	<b>A Comparison Between the Systems Studied</b>	<b>71</b>
<b>5.3</b>	<b>Introducing the Dipole Approximation into the Model</b>	
	<b>-The Basic Model</b>	<b>75</b>
<b>5.4</b>	<b>Introducing the Exchange Effect into the Model</b>	<b>83</b>
<b>5.5</b>	<b>The Enhanced Model</b>	<b>90</b>
5.5.1	Introducing the exact magnetostatic calculation into the model	90
5.5.2	The Shift Method	91
5.5.3	Investigating $r_1$	93
5.5.4	Comparing the basic magnetostatic model against the enhanced model	96
5.5.5	Investigating $h^*$ and $h_{int}$	100
5.5.6	Introducing the exchange interaction into the enhanced model	102
<b>5.6</b>	<b>Summary</b>	<b>108</b>
<b>6.</b>	<b>Conclusions and Further Work</b>	<b>109</b>
	<b>References</b>	<b>116</b>

# List of Figures

2.1	Cross section showing the general structure of a typical recording disk	8
2.2	Schematic diagram of a dc-sputtering system	9
2.3	TEM image of UC-processed CoCrTa thin film	10
2.4	The magnetisation process	13
2.5	A magnetised sample illustrating the demagnetising field ( $H_d$ )	14
2.6	Illustrating the shape effects of the demagnetising field	15
2.7	Possible domain structures for a magnetised sample	16
3.1	Construction of the Voronoi polygon around $p_i$	22
3.2	Initial real cell together with virtual cells	23
3.3	Initial Voronoi configuration used to represent the model	24
3.4	Voronoi construction of 40 grains	25
3.5	A typical hysteresis loop showing both the remanence and the coercivity	27
3.6	A typical enlargement of a section of the generated structure	28
3.7	The grain structure showing the natural division into triangles	29
3.8	A single domain particle	30
3.9	a: Hysteresis loop obtained when the external field is perpendicular to the easy axis	32
	b: Hysteresis loop obtained when the external field is applied parallel to the easy axis	32
3.10	Hysteresis loops illustrating the Stoner and Wohlfarth theory	33
4.1	Illustrating the average magnetisation for each triangle	47
4.2	Illustrating field at $P$ due to dipole at $Q$	47
4.3	Illustration showing the region to be integrated	51
4.4	Rotating the axes to simplify the integrals	52
4.5	Illustrating the $x$ component of the surface integral	52
4.6	Dividing triangle into regions $A$ and $B$ in order to calculate the $y$ component	55
4.7	A typical triangle illustrating magnetisation at the vertices	59
4.8	The cell represents the system of triangles and highlights the regions	

	where the exact and dipole calculations are carried out on a given point $P$	65
4.9	Illustrating the triangle to be integrated	66
4.10	Illustrating the Shift Method	68
5.1	Hysteresis loops from a system of 15 and 40 grains with random easy axes	73
5.2	Hysteresis loops from the system of 15 grains with 3 sets of random easy axes	74
5.3	Hysteresis loops from the system of 40 grains with 3 sets of random easy axes	75
5.4	Hysteresis loops to show the effect of increasing $h_{int}$	78
5.5	Graph to show remanence values against increasing values of $h_{int}$	78
5.6	Graph to show coercivity values against increasing values of $h_{int}$	79
5.7	Arrow plot taken at remanence when $h_{int}=0.0$	80
5.8	Arrow plot taken at coercivity when $h_{int}=0.0$	80
5.9	Arrow plot taken at remanence when $h_{int}=0.01$	81
5.10	Arrow plot taken at coercivity when $h_{int}=0.01$	81
5.11	Arrow plot taken at remanence when $h_{int}=0.03$	82
5.12	Arrow plot taken at coercivity when $h_{int}=0.03$	82
5.13	Graph to show the effects on the remanence as $C_1^*$ is increased	85
5.14	Graph to show the effects on the coercivity as $C_1^*$ is increased	85
5.15	Graph to show the effects on the remanence as $C_2^*$ is increased	86
5.16	Graph to show the effects on the coercivity as $C_2^*$ is increased	86
5.17	Arrow plot taken at remanence when $h_{int}=0.03$ , $C_1^*=0.02$ and $C_2^*=0.4$	87
5.18	Arrow plot taken at coercivity when $h_{int}=0.03$ , $C_1^*=0.02$ and $C_2^*=0.4$	87
5.19	Arrow plot taken at remanence when $h_{int}=0.03$ , $C_1^*=0.02$ and $C_2^*=1.0$	88
5.20	Arrow plot taken at coercivity when $h_{int}=0.03$ , $C_1^*=0.02$ and $C_2^*=1.0$	89
5.21	Introducing each of the interactions into the basic model	90
5.22	Results from calculating the surface integral with and without the shift method, where $P$ was placed at a distance from $Q$	92
5.23	Results from calculating the surface integral using the shift method, where $P$ was placed at a vertex of $Q$	92

5.24	Hysteresis loops illustrating the effect on the remanence and coercivity values as $r_1$ is varied	94
5.25	Hysteresis loops illustrating the introduction of the exact calculation in the model	95
5.26	Illustrating the effect on the remanence as $r_1$ is increased	95
5.27	Illustrating the effect on the coercivity as $r_1$ is increased	96
5.28	Hysteresis loops illustrating the effects when using the two methods of calculating magnetostatic field	97
5.29	Hysteresis loops illustrating the differences in the calculation of the near neighbours	98
5.30	Hysteresis loops illustrating the effects when using the shift method	99
5.31	Hysteresis loops illustrating the effects on varying $h^*$ and $h_{int}$	100
5.32	Arrow plot taken at remanence when $h^*=h_{int}=0.01$	101
5.33	Arrow plot taken at coercivity when $h^*=h_{int}=0.01$	102
5.34	Hysteresis loops illustrating the differences between the basic and the enhanced model when all the interactions are included	103
5.35	Graph to show the effect on the remanence as $C_2^*$ is increased in the enhanced model	104
5.36	Graph to show the effect on the coercivity as $C_2^*$ is increased in the enhanced model	105
5.37	Arrow plot taken at remanence when $h^*=h_{int}=0.01$ , $C_1^*=0.02$ and $C_2^*=0.4$	105
5.38	Arrow plot taken at coercivity when $h^*=h_{int}=0.01$ , $C_1^*=0.02$ and $C_2^*=0.4$	106
5.39	The enhanced model	107

# List of Tables

5.1	Table of remanence values for different values of $\theta$ , comparing the two systems against the expected values	72
5.2	Table of remanence and coercivity values for two systems with random easy axes, comparing against the values obtained by Stoner and Wohlfarth	73
5.3	Table to show the number of triangles within $r_1$ and $r_2$ with different values of $r_1$ against constant $r_2$	93

# Acknowledgements

I would like to thank my supervisor, Dr. Dave Parker for all his help and patience during the time spent on this project.

I would also like to thank all the people I have met during my time in the basement. A special thanks goes to Uncle Tim and Auntie Gill for being there when times were hard.

Thankyou to those who never gave up on me and to those who did, it made me stronger.

Finally, to Raj, I know I would not have come this far without him.

This thesis is dedicated to Amma and Abba. They have always been there for me and given me so much love and support throughout my life. I hope I have made them proud.

# 1. Introduction

Magnetic recording has just celebrated its centennial anniversary and so, with the start of the new millennium, what does the future hold for this industry? This thesis will not be concerned with answering such a big question, but will provide some fuel to allow the research into a particular area of magnetic recording to continue. The research area dealt with in this thesis is micromagnetic modelling of thin film media. This chapter starts with a brief introduction to magnetism to provide the basic theory behind the concepts used in micromagnetic modelling. Magnetic recording is then dealt with which details the types of media and devices used within the industry. It also describes the conditions required for optimum recording from both media and devices. The chapter concludes with an overview of the thesis describing the aims and objectives of the research undertaken.

## 1.1 Introduction To Magnetism

One of the first introductions mankind had to magnetism occurred centuries ago and was in the form of a material known as magnetite. This material is found naturally in a magnetised state and has the associated properties. At the time of discovery magnetite must have seemed magical. As its properties were discovered, such as its ability to indicate positions of north and south and thus the invention of the compass, research into this phenomenon began. In 1600, a book entitled 'On The Magnet' was published by William Gilbert who experimented with magnetite and envisaged the earth's magnetic field.

There are now many known magnetic materials and a definition needs to be sought to identify such a material. Jakubovics (1994) provides a simple definition by stating that if two objects are attracted to each other but also repel each other depending on their orientation, then these two objects may be called magnets. He goes on to describe other

objects that may be attracted to but not repelled by magnets and not attracted to or repelled by each other. He defines these objects as those that consist of magnetic materials.

The reasons why this definition might not be satisfactory are also provided by Jakubovics. His first reason is based on the fact that the magnetic state of a material can be altered in many ways, e.g. with temperature. He then introduces another force that could be mistaken for magnetism, the electrostatic force. This mistake is because many materials can simulate the attraction property of a magnet after they have been rubbed with another material.

There is a fundamental difference between these two forces. An electrostatic force can either be solely attractive or repulsive. It cannot be both. However, when two magnets attract each other, they will also repel each other if orientated differently. This difference can be explained by the concept of charges. The electrostatic force can be considered to be due to electric charges which can be separated to either like charges repelling or unlike charges attracting. The same concept can be used in magnetism, but in this case the magnetic charges cannot be separated. The magnetic dipole is the term used to describe a pair of magnetic charges located a small distance from each other which are equal in magnitude but oppositely charged.

The dipole can be considered as the most elementary unit in magnetism and it is with this that the theory of magnetism begins.

## **1.2 Magnetic Recording**

Magnetic recording systems have been described by Grundy (1998) as probably the most rapidly developing area of high technology in the world today. The main aim of the research into this industry is to store as much information onto the media as possible. This in turn leads to investigating the limit to the density of the stored information with respect to the noise factors and also the stability of the bits of information. This area of research can be divided into two categories, media and recording heads. Media covers

magnetic disks, as used in computer data storage, and magnetic tapes, used for audio and video storage. The area of recording heads is associated with the technologies dealing with the process of writing the information onto the media and also reading the stored information. Another important factor to be considered by the recording industry is that of cost.

There are numerous books on the magnetic recording process such as Jiles (1991), Mee and Daniels (1987) and Jakubovics (1994). The recording process is based around the theory of hysteresis properties of the magnetic media. Hysteresis will be discussed in detail in Chapter 3.3. Briefly, if a field has been applied to a magnetic material, the material has the ability to remain magnetised in the field direction once the applied field has been removed. Therefore data can be stored in the form of magnetic imprints on the magnetic material (Jiles, 1991).

Research into the recording industry is directed towards optimising the recording properties of the recording process together with the magnetic media. The recording device must be able to store the information using relatively small fields. The stored information must be able to be easily retrieved without any damage or loss of information. At the same time, the information must be able to be erased when required and possibly recorded over.

The recording industry is also constantly trying to increase the density of the recorded information by reducing the size of the bits. The size of the bits is primarily governed by what is known as the activation volume (O'Grady and Laidler, 1999). This represents the smallest volume of material that can reverse coherently and therefore the smallest possible size of a bit. The area studied in this thesis is thin film media and through experimental studies the material used has been found to consist of closely packed grains (Arnoldussen and Nunnelley, 1992). In granular material the activation volume may consist of several grains. The activation volume should be as small as possible and ideally should only consist of one grain. This requirement is hard to achieve as the grains interact magnetically with each other, see Chapter 3.

## 1.3 Overview Of The Thesis

A brief introduction to magnetism and recording has just been covered. This hopefully provided an understanding as to why research in the magnetic recording industry is carried out and its importance. Through work carried out by research centres, it is hoped that the magnetic recording industry will continue the success it has had during the last century. As the demand for improved recording media continues, the greater the need for its understanding. Research into magnetic recording can be achieved either experimentally or theoretically in the form of micromagnetic models. This hopefully provides enough reason as to why the research area of this thesis was studied. The research undertaken provides another stepping stone to help find improved and efficient micromagnetic models for thin film media and provides another solution to overcome problems discovered by fellow researchers in the field.

Chapter 2 provides a description of thin film media. Its purpose is to provide a background to the magnetic material modelled in this thesis in order that comparisons can be made. It begins with describing the manufacture of thin film, initially discussing its role in the magnetic recording disk. The microstructure of thin media is then discussed from an experimental point of view. This is of importance as it is this microstructure that needed to be simulated. The concept of ferromagnetism is also introduced in this chapter giving some light on theories such as spontaneous magnetism, domain walls and the demagnetising field. This chapter concludes with a review of previous work carried out on thin film media. This is aimed to give an insight into other micromagnetic models and the background to why the model in this thesis was developed.

Chapter 3 deals with the micromagnetic modelling of the thin film. The thin film can be thought of as a system of magnetically interacting particles. The chapter discusses the theoretical concepts used to model the magnetisation processes within such a system of magnetic particles. The technique used in generating the physical structure of the thin film is discussed first. The chapter then defines the principles behind the hysteresis loop, an illustration of how the magnetisation of a system varies under an applied external field. Each point on the loop is the average magnetisation taken over all the

particles in the system at a certain field point when all the particles have reached equilibrium. The factors affecting the magnetisation of each particle are the applied external field, the anisotropy field, the magnetostatic field and the exchange field. These are all discussed in detail as they contribute to what is termed in the chapter as the total effective field acting on a particle.

Once the total effective field is calculated it is necessary to study the motion of the magnetic moment as it experiences this field. The motion of the moment is described by the Landau-Lifshitz equation and solved using the Runge-Kutta Method. These are discussed in detail and conclude the chapter on micromagnetic modelling.

The main aim of this thesis is concerned with the magnetostatic calculation and as a result Chapter 4 has been dedicated to it. It proves to be the most time consuming of all the calculations. A lot of research is therefore dedicated to finding approximate solutions to the calculation and improving the computational time. The chapter begins by discussing an approximate approach to calculating the magnetostatic field which is based on dipoles. An exact magnetostatic calculation is then introduced based on volume and surface charges. The initial aim of the project is to calculate the close range magnetostatic field via the exact calculation and the dipole approximation is to be applied for the long range effects. Once implemented, the exact calculation proves to be not as exact as expected since singularities in the equation were found. This leads to the introduction of the Shift Method which provides one solution to overcome the problem discovered whilst using the exact calculation.

Chapter 5 deals with the results observed from the research in this thesis. The main results illustrate the behaviour of the micromagnetic model in the form of hysteresis loops and arrow plots. The initial studies were on a small system of 15 grains and after the model was tested it was applied to a larger system of 40 grains. The first results were on the effects of anisotropy and compared to the famous work carried out by Stoner and Wohlfarth (1991). Once agreement was sought the approximate magnetostatic calculation was introduced and applied to both short and long range effects. The effects on the hysteresis loops were studied as the strength of the magnetostatic field was varied. The exchange interaction was next introduced and observed. The main aim was to observe the effect of using the exact and approximate

magnetostatic calculations. The questions put forward were to check whether it was necessary to include the exact calculation in the model and whether the approximate calculation proved sufficiently accurate. The answers to the questions are first illustrated in this chapter and then discussed in the Chapter 6 together with further work to be continued after this study.

## **2. Thin Film Media**

### **2.1 Introduction**

When the term “thin film media” is used it usually refers to thin film materials used as coatings on tapes, flexible and rigid magnetic recording disks. The thin film material modelled in this thesis is used mainly as a coating on rigid disks. Over the last century there has been a desire to continuously increase the storage density of these disks with a rate of 60% per annum (Grundy,1998). This desire was fuelled by the fact that magnetic storage still provided the most economical means of data storage together with its rapid direct-access times. Towards the start of the new millennium the reported rate of increase was 100% (O’Grady and Laidler, 1999). Current values reported at the time of writing this thesis were 45Gb/in<sup>2</sup> (Seagate Corporation). With this rapidly increasing storage density comes the increasing need to understand more about thin film media and to improve on the models used to represent the magnetic material.

This chapter first describes the structure of a recording disk and illustrates the role thin film has within it. Next the manufacturing process of thin films is dealt with and introduces the sputtering technique. The actual microstructure of a thin film is then illustrated and describes some of the current compositions. This is of importance as it is this microstructure that has to be simulated. The characteristics of thin film media are then discussed and the chapter concludes with previous work on thin films.

### **2.2 Manufacture of Thin Film Media**

The thin film magnetic coating provides only one of the many layers that make up rigid magnetic recording disks. Figure (2.1) shows a cross section of the general structure of a typical recording disk.

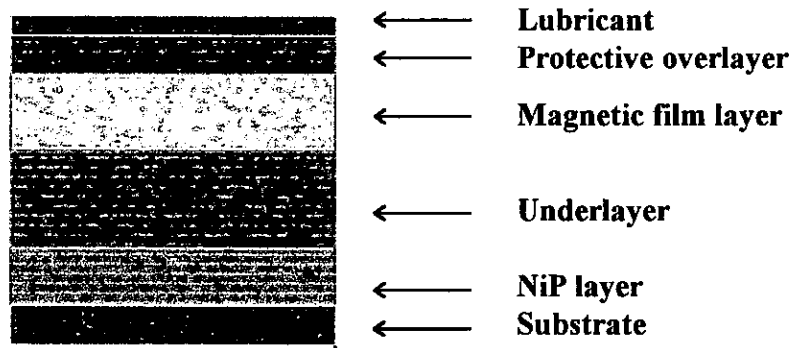


**Figure (2.1): Cross section showing the general structure of a typical recording disk**

The substrate is usually made up of an aluminium-magnesium alloy which is often chemically plated with a nickel-phosphorus alloy as a preparation for the subsequent layers. These layers have in the past been applied by chemical plating or electrodeposition techniques. Nowadays they are usually sputter deposited. The underlayer is regarded as the seed layer as it promotes the growth of the magnetic film layer above it. The most common underlayer used today is chromium and provides the magnetic layer above with the essential grain size and morphology to enhance magnetic recording. The magnetic layer consists of a cobalt based alloy usually added with platinum, tantalum and chromium. The magnetic layer is then protected with an overlayer, usually carbon, to prevent any damage to the thin film or any loss of the storage information. The final layer is a very thin lubricant layer which is applied by simply dipping the disk into a solution of the lubricant.

As stated earlier, the process used to apply the intermediate coats is usually some form of sputtering technique. Figure (2.2) is a schematic diagram of a dc-sputtering system (Mee and Daniel, 1987).

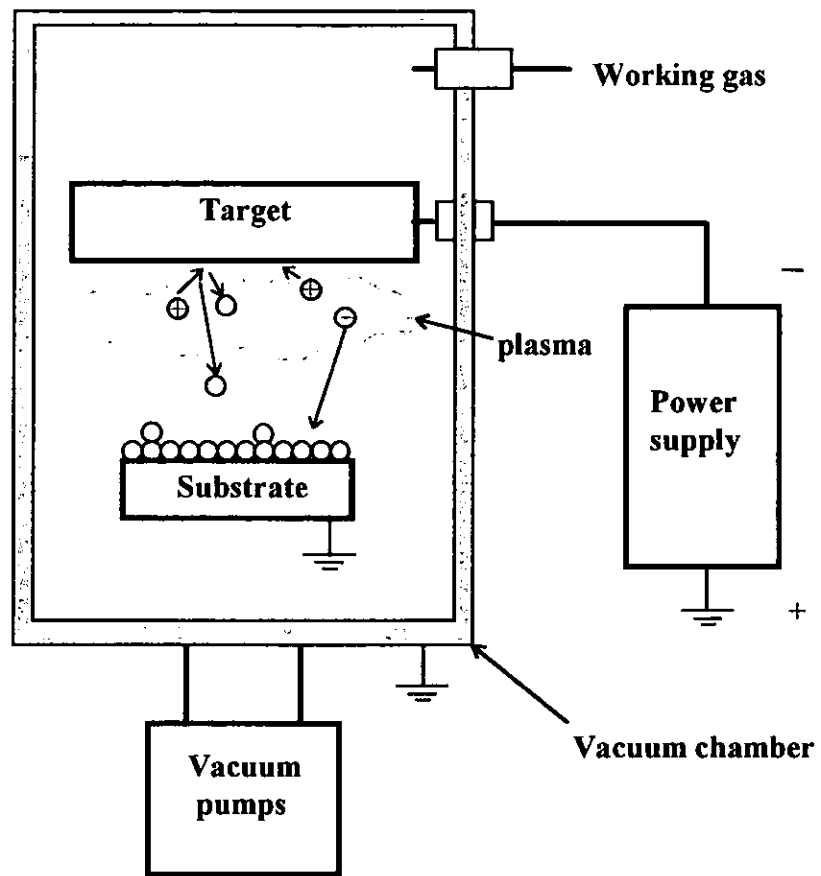


**Figure (2.2): Schematic diagram of a dc-sputtering system**

Sputtering deposition takes place in a vacuum chamber filled with a sputtering gas, usually argon. The procedure begins by applying a voltage between the target material and the substrate to be sputtered. The target is biased negatively with respect to the substrate. When the voltage has been applied, a plasma of electrons and gas ions is generated. These positively charged ions accelerate towards the biased target and knock off atoms of target material. The sputtered atoms then head towards the substrate where they are deposited.

There have been some recent improvements to the sputtering technique. An Ultra-Clean sputtering process (UC-process) has been developed (Takahashi and Shoji, 1999; Imakawa *et al.*, 1998) where the microstructures of the thin film can be controlled by the process conditions. These conditions include the substrate temperature, sputtering gas pressure and the bias voltage.

## 2.3 Microstructure of Thin Film Media

It is well known that the microstructure of the thin film material is closely related to its magnetic recording properties (Kojima *et al.*, 1995). Experimental results have shown that the thin film layer has a microstructure comprising irregularly shaped grains, due to the microstructure of the chromium underlayer (Arnoldussen and Nunnelley, 1992). This microstructure can be seen using techniques such as transmission electron microscopy (TEM), electron and x-ray diffraction, scanning probe microscopy (SPM) and atomic force microscopy (AFM). Figure (2.3) shows the microstructure of CoCrTa film observed using TEM (Imakawa *et al.*, 1998). The grain sizes in current Co-alloy based thin film are around 10-50 nm (Grundy, 1998).

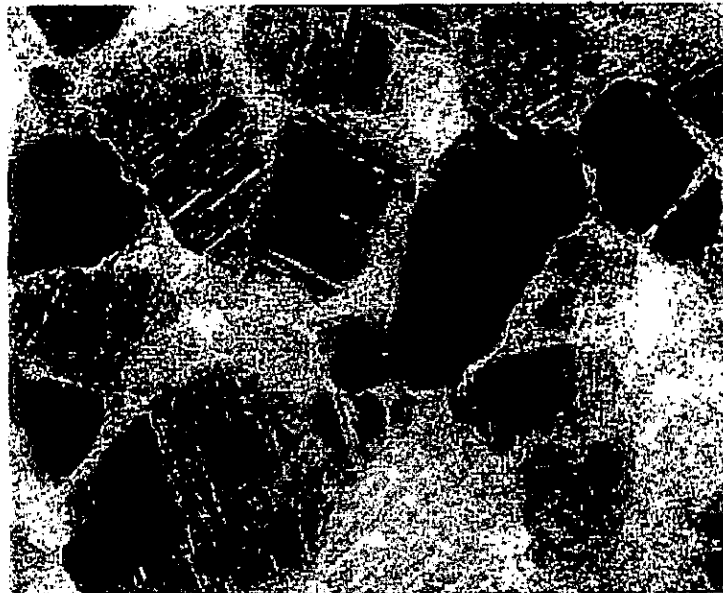


**Figure (2.3): TEM image of UC-processed CoCrTa thin film media**

For optimum recording the thin magnetic layer is required to have optimised magnetic properties such as high values of coercivity ( $H_c$ ), remanence ( $M_r$ ) and saturation magnetisation ( $M_s$ ). Coercivity is the field required to demagnetise the material and a high value protects the recorded information from any stray magnetic fields. The saturation magnetisation occurs when all the moments are parallel with the applied field and an increase in the applied field does not affect the magnetisation. A high saturation

provides a large enough signal for reading process. Remanence is the magnetisation remaining in a sample when the applied field is removed. High values ensure no recorded information is lost after the writing process.

Current compositions of the magnetic film are typically  $\text{Co}_{75}\text{Cr}_{13}\text{Pt}_{12}$  and  $\text{Co}_{85}\text{Cr}_{13}\text{Ta}_2$  (Grundy,1998). The chromium was originally added to improve the corrosion properties of the thin film, however, it is now found to increase coercivity and reduce replay noise (Kojima *et al.*,1995). This can be explained by looking at Figure (2.3) again which shows not only the grains in the film but also the grain boundaries which separate the individual grains. When chromium is added to the cobalt it has limited solubility which causes a tendency to migrate towards the grain boundaries. This non-magnetic chromium boundary decreases the intergranular exchange coupling and thus increases the coercivity and reduces noise. Tantalum and platinum when added are situated in the cobalt-rich grain. These are said to increase magnetocrystalline anisotropy and coercivity. The addition of tantalum has recently been found to promote the movement of the chromium to the grain boundaries (Kim *et al.*,1999).

## 2.4 Characteristics of Thin Film Media

Magnetic materials can be classified into categories according to their magnetic susceptibility ( $\chi$ ). This property is an indication of how responsive a material is to the field applied to it (Cullity, 1972) and is expressed mathematically as:

$$\chi = \frac{M}{H}$$

where  $M$  is the magnetic moment per unit volume of material and  $H$  the applied field. When the  $\chi$  of a material is small and negative ( $\approx -10^{-5}$ ) it is classed as diamagnetic. In this case the magnetisation opposes the field applied to it. The material is classed as paramagnetic if its  $\chi$  is small and positive ( $\approx 10^{-3} - 10^{-5}$ ). Here the magnetisation is aligned with the applied field but it is relatively weak. The class of interest is the

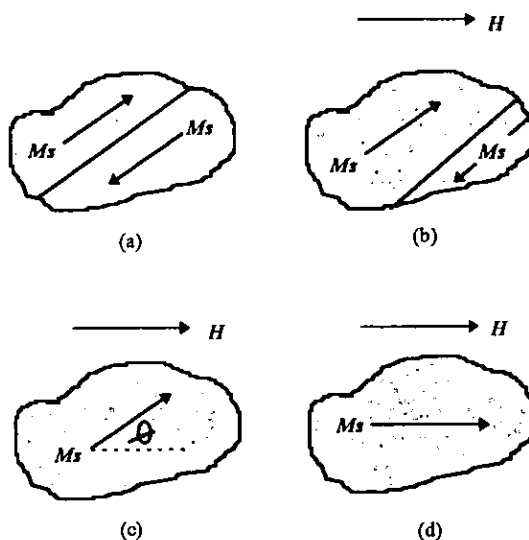
ferromagnetic materials. The  $\chi$  of these materials is positive and much greater than 1 ( $\approx 50-10,000$ ) (Jiles, 1991).

The cobalt-based material used in thin film recording media comes under the category of a ferromagnetic material. Other examples include materials composed of iron or nickel. One of the most important properties of ferromagnetic materials is their ability to acquire a large magnetisation under the influence of relatively weak fields. This characteristic makes ferromagnetic materials ideal for recording. They are also known for their spontaneous magnetisation in the absence of any externally applied field.

### 2.4.1 Weiss's Theory

The initial suggestion for this behaviour was proposed by Weiss in 1906. He introduced the concept of the molecular (or mean) field. This field was regarded as the effective field that aligned neighbouring moments parallel to each other causing the spontaneous magnetisation. The question then arose regarding material in an unmagnetised state. Weiss put forward another proposal introducing the concept of domains. He suggested that ferromagnetic materials are made up of regions called domains, where each domain is of saturated magnetisation and each domain being magnetised in a different direction. The occurrence of such a material in an unmagnetised state was said to be due to the directions of these saturated domains cancelling each other out. The effects of applying a field to this material using Weiss's theory are illustrated in Figure (2.4) (Cullity, 1972). A small portion of a magnetic material is represented and in (a) is divided into two domains. The line in between the two domains is termed the domain wall. In case (a), where no field is applied, the overall magnetisation is zero as the domains are spontaneously magnetised in opposite directions. When a field is applied, (b), the upper domain grows causing the movement of the domain wall and thus shrinking the lower domain and (c) occurs. The magnetisation at this point is equal to  $M = M_s \cos\vartheta$  where  $\vartheta$  is the angle between the direction of the magnetisation and the applied field.

Eventually, when the applied field is strong enough, the magnetisation is saturated and is aligned with the direction of the field (d).



**Figure(2.4): The magnetisation process**

The domain structures within ferromagnetic materials can be observed nowadays using equipment such as the Lorentz electron microscope and techniques using x-ray topography (Chikazumi, 1997).

The existence of domains has been proven experimentally, so the question now arises asking why and when does the material divide into domains. The answer basically is that the material always tends to a state where its energy is at a minimum (Tebble, 1969). A material will therefore create more than one domain if it proves to be energetically more favourable. The energy of the material is made up of many factors and of interest for this study are exchange, anisotropy and magnetostatic energies, see Chapter 3. Each of these energies is competing with each other to find its own minimum at the expense of the domain structures.

Briefly, the effect of exchange within a material tends to align the moments parallel to each other. Anisotropy effects cause the moments to lie in their own preferred direction. These two effects determine the thickness of the domain walls. As the domain wall is a transition region between two domains of different magnetisations, the magnetisation

within the wall is constantly changing. If the wall is infinitely thin, adjacent moments within the wall would lie antiparallel to each other which gives rise to a maximum exchange energy. If there was a spread of rotation and thus leading to a thicker wall the exchange energy would be less. However the moments in this case are not oriented in their preferred direction which causes an increase in the anisotropy energy. The domain wall width is therefore a compromise between exchange and anisotropy. Another factor characterising the domain structures is the demagnetising field effect which arise from the magnetostatic interactions between the elements within the material.

## 2.4.2 The Demagnetising Field

The energy associated with this effect is often regarded as the self energy of a particle as it describes the energy of a particle in its own field. An illustration of how this type of energy arises can be seen in Figure (2.5). A magnetised sample is shown here together with its field lines. A field is generated inside the sample which opposes the direction of the applied field.

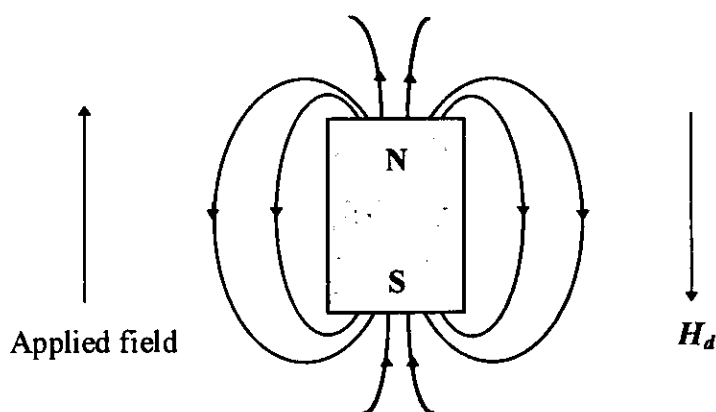


**Figure (2.5): A magnetised sample illustrating the demagnetising field ( $H_d$ )**

This is regarded as the demagnetising field ( $H_d$ ) and its strength depends on the magnetisation of the material together with the shape of the sample. The demagnetising effects are due to the free poles which are created at the top and bottom of the sample as

shown in Figure (2.6). Here the shape effects on the demagnetising field are illustrated. The demagnetising field is stronger in the shorter sample as the poles are closer together and weaker in the sample where the poles are further apart. The demagnetising field is not uniform throughout the sample but is concentrated in the region near the two ends (Jakubovics, 1994).

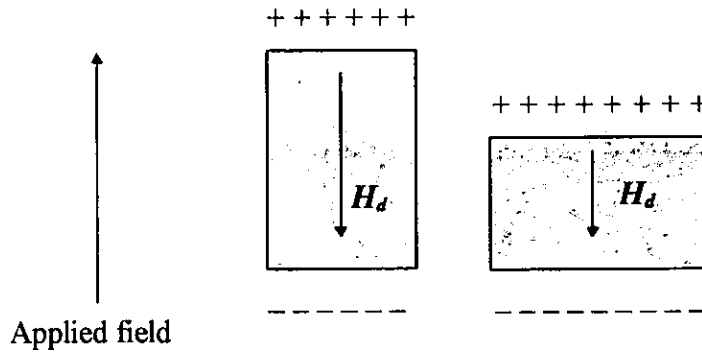


**Figure (2.6): Illustrating the shape effects of the demagnetising field**

As stated earlier in the chapter, the system wants to be in a state of minimum energy. The existence of domains is as a result of such energy minimisation. A single domain sample acquires a large demagnetising energy and through the formation of domains this energy is reduced as illustrated in Figure (2.7). In (a) the sample has divided into two domains decreasing the demagnetising field, in (b) the sample has divided into four domains decreasing the demagnetising field even further. The optimum domain structure for a minimum demagnetising field is (c), this is often called a domain of flux closure. Here the magnetisation is perpendicular at the top and bottom of the sample and no free poles are present. Although the demagnetising energy is being reduced by the formation of domains, there is energy being used to form these domains. The only time a domain will form will be when the decrease in demagnetising energy is greater than the energy required to form a domain wall.

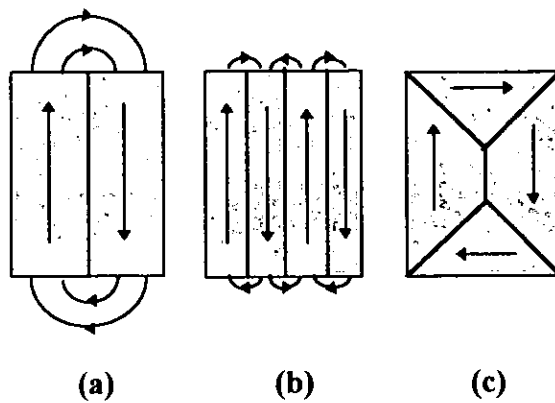


Figure (2.7): Possible domain structures for a magnetised sample

## 2.5 Previous Work on Thin Film Media

Experimental research indicates that thin films are composed of a layer of closely packed magnetic grains separated by non-magnetic boundaries. Micromagnetic models have been developed to simulate such grain structures and to gain understanding of their magnetisation states.

A model developed by Zhu and Bertram (1988, 1991) proposed that the thin film could be represented by an array of hexagonally shaped grains with intergranular boundary separation. It was assumed that each grain was uniformly magnetised and if isolated would follow Stoner-Wohlfarth coherent rotation during reversal, see Chapter 3. The computation utilises a dynamic approach based on the Landau-Lifshitz equation of motion and includes effects due to anisotropy, magnetostatic and intergranular exchange coupling. For the effect due to anisotropy, both well oriented and random easy axes were considered. The intergranular exchange coupling was the summation of the exchange due to the nearest neighbour grains and is governed by an exchange constant ( $C^*$ ). The weaker the exchange coupling across the non-magnetic grain boundary, the closer to zero the exchange constant will be and vice-versa. The magnetostatic calculation was the summation of an integration on grain surfaces, taking into account all the grains in the model.

Lu *et al.* (1992) studied a model similar to Zhu and Bertram with the difference being that the grains were assigned randomly distributed easy axes which could be either confined to the grain or in 3-D.

Dean (thesis) proposed a model, similar to that of Zhu and Bertram, comprising a regular hexagonal structure. The grains for his model were represented by spheres of equal radius. Here, instead of using the Landau-Lifshitz equation to model the motion of the moments, he employs a method based on energy minimisation. The total energy was the sum of the anisotropy, using random easy axes, exchange and magnetostatic energy. The magnetostatic energy was calculated using a dipole-dipole approximation as opposed to the surface charge integration suggested by Zhu and Bertram. Due to the fact that the magnetostatic interaction is long range it should comprise all the grains in the structure. However, Dean suggested that the magnetostatic energy term decreases as the radius from a particular grain passes a certain point. He therefore, only included grains within a certain radius of a particular grain for the magnetostatic energy calculation.

These models, however, seem unrealistic due to their regular structure. Walmsley (thesis) worked on a model which initially began as a regular structure of spaced spheres. These spheres were moved and grown until they formed a compact irregular structure. This work was continued by Hannay *et al.* (1999) and extended by introducing the Langevin equation to study the motion of the particles. The difference between this and the Landau-Lifshitz equation was that it introduced random thermal perturbations into the total effective field acting on each grain.

The micromagnetic model used for the work in this thesis is based on a model proposed by Tako (thesis). A more realistic representation of thin magnetic films is considered. Instead of having an array of regular hexagonal grains, an array of irregularly shaped grains was used. These were generated by the Voronoi construction, described later. Porter *et al.* (1996) also employed this method of construction when comparing the effects of microstructure on extrinsic magnetic properties. Two patches were generated, one made up of regular hexagonal grains and the other of irregularly shaped Voronoi grains. Significant differences in coercivity values were found from the two patches. A similar method of generating irregularly shaped grains, used by Otani *et al.* (1990), is the Wigner Seitz method.

Earlier models, described above, also assumed uniform magnetisation within each grain. This proves to be very unrealistic. Tako discretised each of the grains into a set of interacting triangles, each triangle having its own magnetisation component. This technique is commonly known as The Finite Element Method and has been described in detail by Vecchio *et al.* (1989). An exact magnetostatic calculation is used comprised of contributions from triangles within a certain radius of a particular particle. The approximate dipole calculation, as used by Dean (thesis), was used for triangles more than twice the average grain size away. The exchange field is made up of contributions from within the grain and also across the grain boundary. The grains are assigned random easy axes for the calculation of anisotropy. The Landau-Lifschitz equation was used to model the motion of the moments and solved using the Adams 4<sup>th</sup> order predictor-corrector method.

For this work, boundary conditions were incorporated, as described by Schrefl and Fidler (1992). Tako's model only considered the basic cell and the effects due to grains within it and hence is only applicable to platelets instead of longitudinal thin films. However, a grain on the edge of the cell, realistically, should interact with the other grains in the basic cell and also nearest grains outside of the cell. Schrefl and Fidler employed the minimum image convention (Heerman, 1990) and suggested that if the basic cell was of length  $L$ , then the cell image only needs to be periodically enlarged by  $L/2$ .

The following chapters discuss the micromagnetic model in detail starting with the Voronoi construction. Tako generated 100 grains for his study. Initially, this model studied only 15 grains in the basic cell but the system was increased to 40 grains once the model was set up. The micromagnetic calculations are then discussed followed by the results and conclusions from this study.

# 3. Micromagnetic Modelling of the Thin Film

## 3.1 Introduction

Micromagnetic modelling is the study of the magnetisation processes within a system of magnetic particles using theoretical concepts. These theoretical concepts, referred to as micromagnetics, mostly originated from the early works of Brown (1962, 1963) and will be discussed in this chapter. Stoner and Wohlfarth (1991) also significantly contributed towards the understanding of the magnetisation processes but they dealt with the behaviour of an isolated single particle and ignored any effects from other particles within a system. This theory will also be discussed as it is an important building block towards the understanding of how these magnetic particles behave.

Micromagnetic modelling provides theoretical insights to stimulate experimental work and together with the development of instruments such as the magnetic force microscope, experimental results on a suitable scale can now verify theoretical results.

The first step towards modelling the thin film was to generate a model of its physical structure. Experimental results have provided the information that thin films consist of irregularly shaped grains (Arnoldussen and Nunnelley, 1992). As discussed in the previous chapter, a simple approach would be to generate a system of regularly shaped polygons (Zhu and Bertram, 1988, 1991). This would however prove to be unrealistic and comparisons to experimental work would not be valid. The structure used in this study was a system of irregularly shaped polygons generated using the Voronoi construction technique (Okabe *et al.*, 1992), discussed later.

Once the structure has been modelled, the magnetic behaviour of the film needs to be simulated. The generated structure represents an array of magnetic particles or moments

which are allowed to rest in any random direction in the plane of the film. It is the behaviour of these moments under an applied external field that needs to be studied. Each moment has not only the effect of the applied field acting on it but also the effects of all the other moments in the system. One approach used by many models was to describe the interaction effects as energy terms and to seek minimisation of the system's energy (Dean, thesis). In this model the effects were described as field terms and a total effective field acting on each moment was calculated. The total effective field consisted of an applied external field, an anisotropy field, a short-range exchange field and a long-range magnetostatic field. These will all be discussed in detail later. It is the motion of each moment that is under observation and the equation used to describe it was the Landau-Lifshitz equation (1935). This equation of motion was solved numerically using the Runge-Kutta method (Atkinson, 1993).

The results obtained are in the form of hysteresis loops, which show the average magnetisation of the system when a high positive external field is applied and reduced monotonically to one applied in the opposite direction, together with pictures of moments captured at different field steps. Only when all the moments have reached equilibrium is average magnetisation taken and plotted at the corresponding field point.

This chapter discusses in detail the theory behind the behaviour of the magnetic particles and the theory behind the hysteresis loop. It also provides the background to the Landau-Lifshitz equation and to the numerical method used to solve it.

## **3.2 Generating The Physical Structure Of Thin Film Media**

Thin film media can be represented as a system of closely packed irregular polygons. The method used to generate such a system was the Voronoi Construction and has been successfully used in previous models (Tako, thesis; Porter *et al.*, 1996; Schrefl and Fidler, 1992). This technique has been used to model a wide range of scenarios, from an astronomer looking at the structure of the Universe to a physiologist examining

capillary supply to muscle tissue. These have been discussed by Okabe *et al.* (1992) where they define a Voronoi diagram as the following.

### 3.2.1 Definition of a Voronoi Diagram

*Given a set of two or more but a finite number of distinct points in the Euclidean plane, we associate all locations in that space with the closest member(s) of the point set with respect to the Euclidean distance. The result is a tessellation of the plane into a set of the regions associated with members of the point set. We call this tessellation the planar ordinary Voronoi diagram generated by the point set, and the regions constituting the Voronoi diagram ordinary Voronoi polygons.*

### 3.2.2 The Voronoi Construction

The construction began by considering a finite number,  $n$ , of distinct points,  $p_1, \dots, p_n$ , randomly placed in the Euclidean plane, where  $2 \leq n < \infty$ . This set of points has Cartesian co-ordinates, i. e.  $(x_1, y_1), \dots, (x_n, y_n)$ . Each point, e. g.  $p_1$ , was taken in turn and the process of finding the region closest to it than to any other point began, i.e. the construction of a Voronoi polygon around it. The initial step was to find all the nearest neighbours of  $p_1$  within a cut-off radius,  $r$ . This was achieved by calculating the Euclidean distance between  $p_1$  and say  $p_i$ , i.e.  $d(p_1, p_i) = \sqrt{(x_1 - x_i)^2 + (y_1 - y_i)^2}$ . If  $p_i$  was one of the closest points to  $p_1$ , i. e.  $d(p_1, p_i) \leq r$  it was termed a neighbour of  $p_1$ . A line was then drawn from  $p_1$  to each neighbour in turn and the perpendicular bisector of this line was constructed. The point at which two neighbouring bisecting lines intersected became a vertex of the Voronoi polygon. Figure (3.1) illustrates the above Voronoi polygon construction around  $p_1$ .

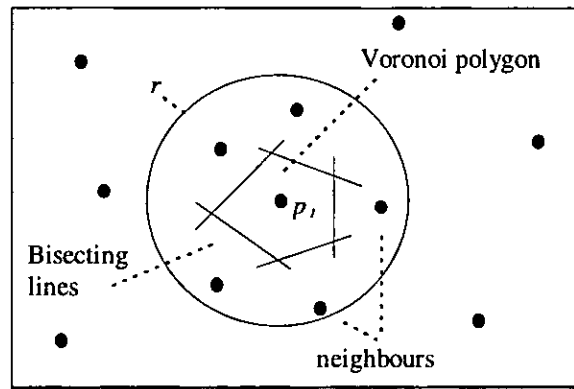
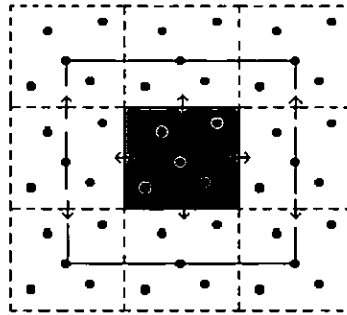


Figure (3.1): Construction of the Voronoi polygon around  $p_i$ .

Initial studies were on a system of 15 grains and the construction began by randomly generating 15 points within a 2-D,  $L \times L$  cell, where  $L$  was set to 1. A minimum distance criteria of 0.003 was set up to ensure generated points were not too close to each other. Without this restriction, the size of the polygons may have been vastly different from each other.

The points generated were regarded as the real seed points and the cell that contained them termed the real cell. This real cell was then translated as shown in Figure (3.2) to give a cell of  $3L \times 3L$  dimensions. The final cell consisted of the real cell surrounded by eight identical virtual cells. The minimum image convention was employed in this model (Heerman, 1990) which states that the particle in the basic cell only interacts with each of the other particles within that cell or their closest images. The outside half of the virtual cells is therefore not required for the calculation.



**Figure (3.2) : Initial real cell together with virtual cells**

A Voronoi polygon was then constructed around each of these real seed points, as described earlier. In this case, the neighbours of a particular real seed point could be real or virtual. If the real seed point was close to the border of the real cell, there was a possibility that some neighbours were in the adjacent virtual cell. The information used in constructing the Voronoi polygons in the real cell was then used in the virtual cells without any further calculation.

The above process generated a system of irregular grains from seed points to fill a 2-D space. The initial Voronoi configuration used is shown in Figure (3.3). Later studies were carried out on a system of 40 grains, generated using the same technique, and is shown in Figure (3.4). This new system of grains together with the model of the exchange field used caused problems when calculating the exchange field. This was due to the fact that some of the Voronoi vertices were too close to each other. This caused problems in the exchange field calculation as it required the division of this distance squared. The problem was solved by merging points which were too close to each other. The merged configuration looked the same as Figure (3.4) because by eye the two very close points looked like one. The slight difference could only be seen by comparing the actual co-ordinate points.

The exchange model had to be slightly modified when it was applied to the new merged system of 40 grains and will be discussed later on in Chapter 3.4.3.

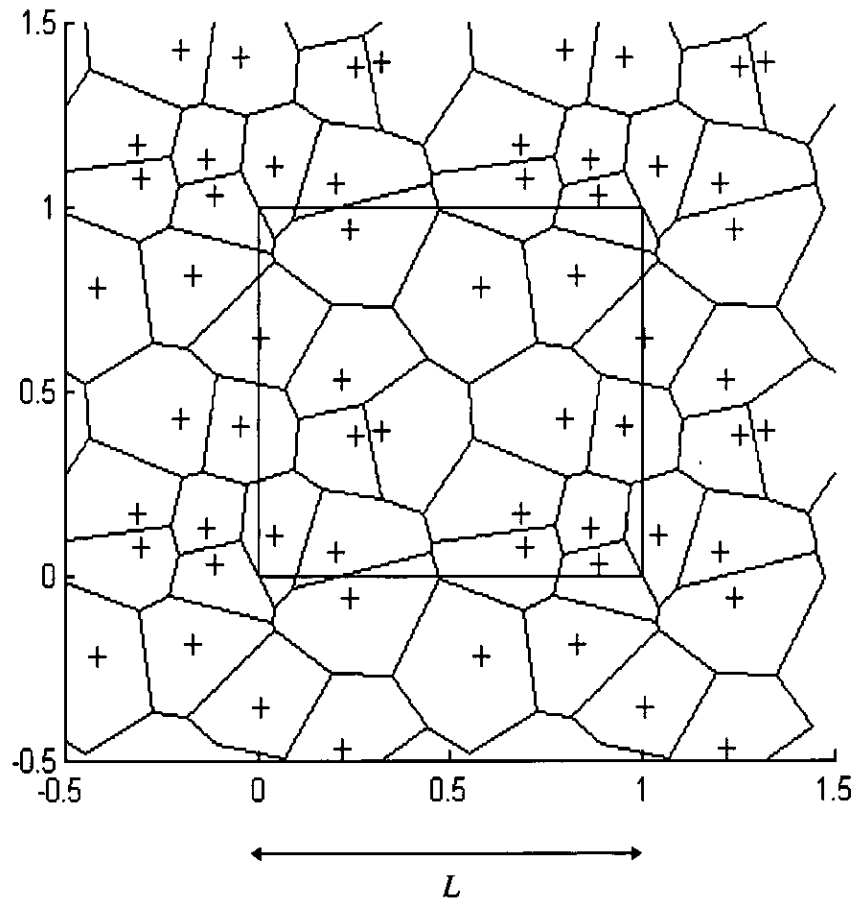


**Figure (3.3) : Initial Voronoi configuration used to represent the model**

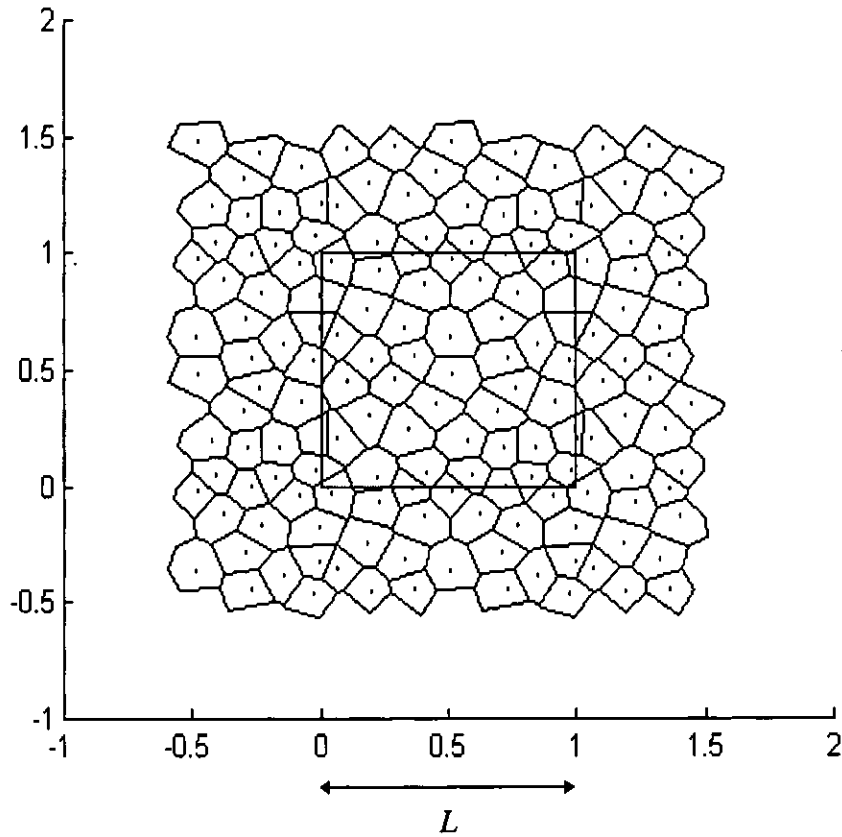


**Figure (3.4): Voronoi construction of 40 grains**

### 3.3 The Hysteresis Loop

A hysteresis loop illustrates how the magnetisation of a sample varies under an applied external field. The sample is initially placed under a large external positive field. This causes all the moments in the sample to align along the same positive direction as the applied field. The sample is then considered to be positively saturated in the field direction. This is due to the fact that any further increase in the field would not increase the magnetisation. The field is reduced gradually causing the moments to relax away from the external field direction into new equilibrium positions. The moments are said to undergo reversible changes for a period when the field is being reduced. In other words, if the field were to be increased back in the positive direction, the same magnetisation states would be achieved as before. At a certain value of the applied field

the moments experience irreversible changes. Here the moments would not retrace their states if the field was to go back. The field is reduced further until no field is being applied to the sample. The magnetisation at this point is known as the remanence ( $M_r$ ). The moments, during this period and some time after still undergo irreversible changes. The external field is now applied in the negative direction, causing the magnetisation to be reduced further. The field required to reduce the magnetisation to zero is known as the coercivity ( $H_c$ ). After the irreversible changes the moments undergo further reversible changes as they did at the start of the process. The field is increased even further in the negative direction until all the moments are negatively saturated. This process of taking the moments from a state of positive saturation to one of negative saturation provides only half of a hysteresis loop. To complete the loop the field is taken from being applied in the negative direction back to zero and then to being applied in the positive one. The moments in the sample are once again saturated in the positive direction. An illustration of a typical hysteresis loop can be seen in Figure (3.5).

The two important features of the hysteresis loop are the remanence and the coercivity. For an ideal recording medium the remanence should be high so that the material retains its magnetisation. The coercivity should be high enough to be unaffected by stray magnetic fields but at the same time low enough to be overwritten.

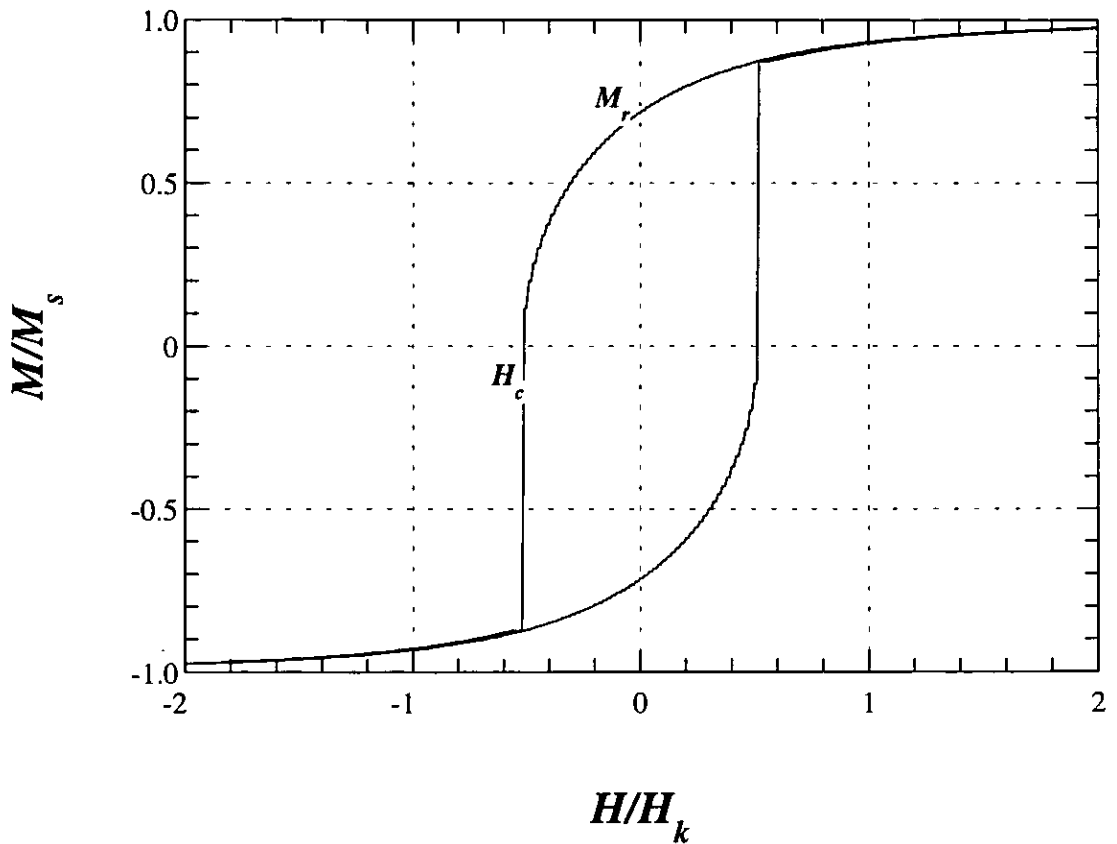
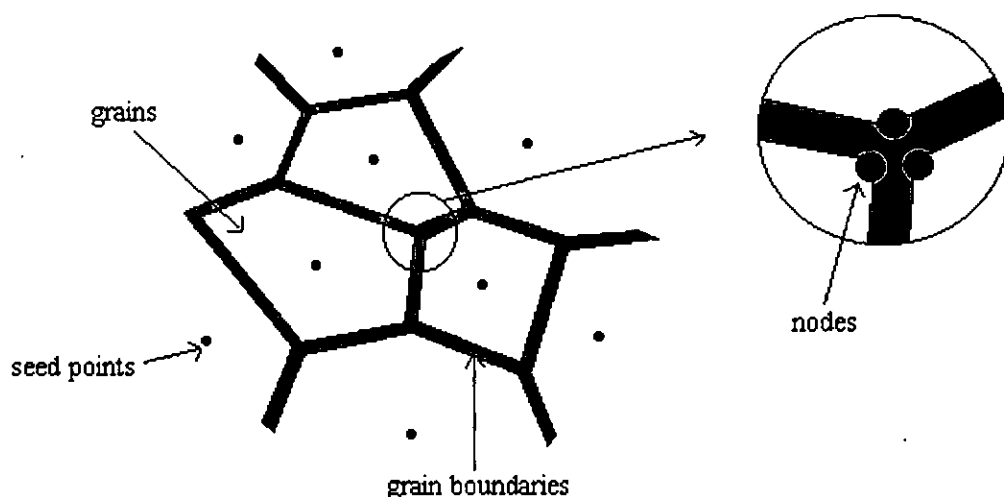


Figure (3.5): A typical hysteresis loop showing both the remanence ( $M_r$ ) and the coercivity ( $H_c$ )

### 3.4 Calculating the Total Effective Field

Once the structure of the thin film had been generated the magnetisation processes needed to be simulated. Figure (3.4) shows the grain construction used and the region of observation was the centre  $L \times L$  cell. As discussed earlier, experimental results have shown that thin films are composed of a layer of closely packed grains separated by non-magnetic boundaries. It was therefore assumed in this model that the grains generated were separated by a region of non-magnetic material, even though it is not shown on the Voronoi construction. Figure (3.6) shows a typical enlargement of a section of the structure and takes an even closer look at a vertex of one of the grains. Each vertex was assumed to be made up of three or four nodes separated by a boundary

but geometrically they shared the same co-ordinates in the cell. The cases where a vertex was made up of four nodes arose when some of the vertices had to be merged to overcome problems in the exchange field calculation.



**Figure(3.6): A typical enlargement of a section of the generated structure.**

A magnetic moment was associated with each seed point within a grain and with each of the nodes at the vertex of a grain. In many earlier models the magnetisation within each grain was assumed to be constant (Zhu and Bertram, 1988, 1991), however this proves to be unrealistic when comparing against experimental results (Schabes, 1991). A more realistic approach was to assume that the magnetisation varies throughout each grain. To simulate the non-uniform magnetisation within each grain, the grains were divided into their natural triangles. A simple illustration of this can be seen in Figure (3.7). The magnetisation within each triangle was assumed to vary linearly.

The contributions towards the total effective field acting on a moment will be discussed in detail starting with the anisotropy field.

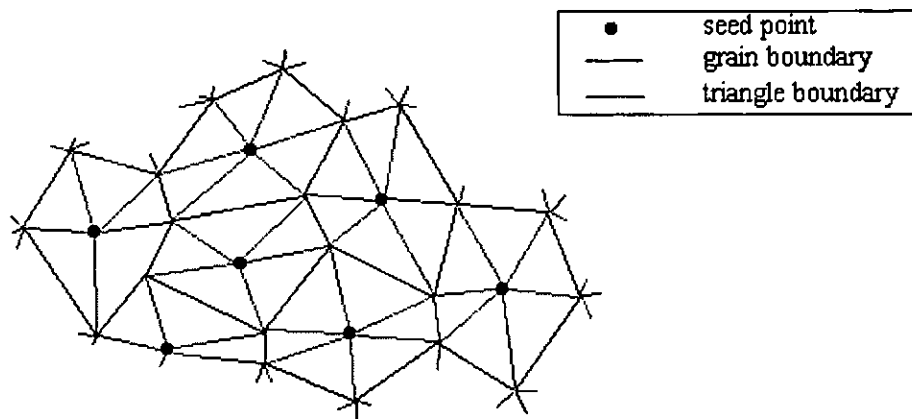


**Figure (3.7) :The grain structure showing the natural division into triangles.**

### **3.4.1 The Anisotropy Field**

The anisotropy field of a grain can be due to either its crystalline structure, its shape or due to stress. Shape anisotropy was incorporated into the model as the magnetostatic field of a grain due to its shape. This was calculated either by a dipole approximation or exactly. In this model stress anisotropy was ignored.

In the absence of an external applied field there is a direction along which the moments of a grain would prefer to lie. This is known as the 'easy axis' and when the moment is in this direction its anisotropy energy is at a minimum. When a sufficiently large external field is applied, the moment will move away from its easy axis and tend to rotate towards the direction of the applied field. The field required to rotate the moment from an easy to a 'hard' direction is known as the anisotropy field. The grains in this model were assumed to have a single easy axis and the term used to describe this characteristic is uniaxial. The anisotropy field was therefore assumed to be uniaxial.

The anisotropy field concept is best illustrated by describing the early works of Stoner and Wohlfarth (1991). They describe the magnetisation reversal processes of single domain particles when an external field was applied, ignoring any magnetic interactions between the particles. The only contributions to the total effective field were the applied external field and the anisotropy field. The particles were assumed to be ellipsoidal and have uniaxial anisotropy. The rotation of the moments was assumed to be coherent, i. e. the moments remained parallel with each other during the reversal process. Stoner and Wohlfarth employed a energy minimisation technique to study the behaviour of these particles. Figure (3.8) is an example of a single domain particle which they studied, where  $\theta$  is the angle between the magnetisation and the easy axis of the particle and  $\phi$  the angle between the applied field and the easy axis.

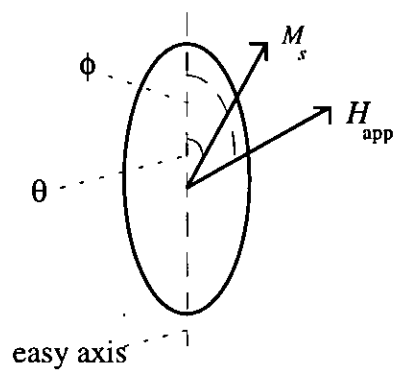


**Figure (3.8): A single domain particle.**

The anisotropy energy of the particle was assumed to be

$$E_{anis} = K \sin^2 \theta \quad (3.1)$$

where  $K$  is the anisotropy constant. Since the moment does not lie in its preferred direction, a torque due to the anisotropy will be produced equal to

$$\begin{aligned}\tau_{anis} &= -\frac{dE_{anis}}{d\theta} \\ &= -2K \sin\theta \cos\theta\end{aligned}\quad (3.2)$$

As well as a torque pulling the moment towards the easy axis there will be another torque pulling the moment towards the direction of the applied field represented by

$$\begin{aligned}\tau_H &= |H \times M_s| \\ &= HM_s \sin(\phi - \theta)\end{aligned}\quad (3.3)$$

where  $(\phi - \theta)$  is the angle between the direction of the magnetisation and the applied field. There will be equilibrium when the torque produced from the applied field equals the torque due to the anisotropy, i. e.

$$HM_s \sin(\phi - \theta) - 2K \sin\theta \cos\theta = 0 \quad (3.4)$$

This can also be regarded as the minimisation of the total energy of the particle with respect to  $\theta$ , where the energy contributions in this case consisted of the applied field and the anisotropy energy.

Consider the case where the external field is applied perpendicular to the easy axis, i.e. when  $\phi = 90^\circ$ . In order to saturate the magnetisation of the particle in the direction of the applied field the anisotropy needs to be overpowered. The field strength required to do so is as follows

$$H = \frac{2K \sin\theta \cos\theta}{M_s \sin(90^\circ - \theta)} \quad (3.5)$$

using trigonometry identity

$$H = \frac{2K \sin\theta \cos\theta}{M_s \cos\theta} \quad (3.6)$$

therefore

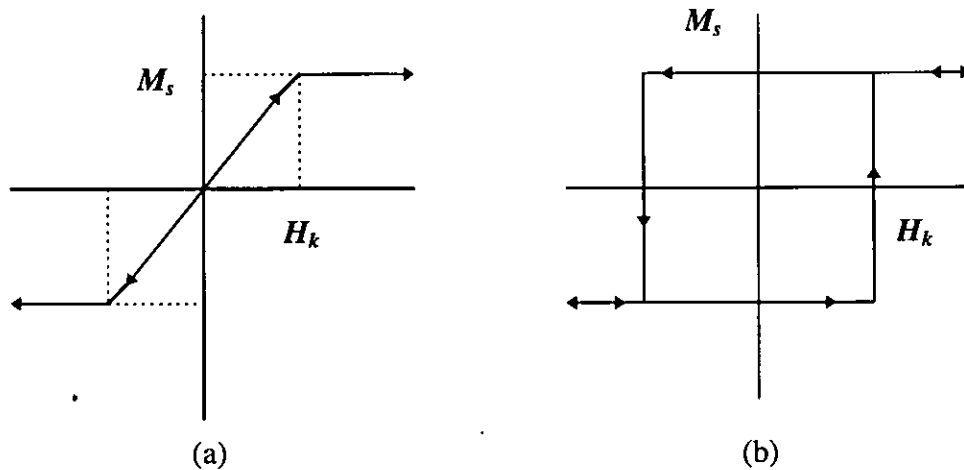
$$H = \frac{2K \sin \theta}{M_s} \quad (3.7)$$

Since the magnetisation in this case now lies in the direction of the applied field,  $\theta = 90^\circ$  and therefore

$$H = \frac{2K}{M_s} \quad (3.8)$$

This field is the anisotropy field strength and is usually represented as  $H_k$ . It is the minimum strength required to pull the magnetisation of the moment away from its easy axis through  $90^\circ$  into the direction of the applied field.

Stoner and Wohlfarth (1991) found that the moments in this case undergo reversible changes throughout as shown in the hysteresis loop (see Figure (3.9a)). The remanence and the coercivity are both equal to zero.



Figure(3.9)

- (a): Hysteresis loop obtained when the external field is perpendicular to the easy axis
- (b): Hysteresis loop obtained when the external field is applied parallel to the easy axis

Another case studied was allowing the easy axis to lie parallel with the direction of the applied field, i. e. when  $\phi$  was equal to zero. From positive saturation the magnetisation of a particle remains along its easy axis. It continues to do so until the applied field

reaches a critical value at which the magnetisation switches irreversibly to the opposite direction. This results in a square hysteresis loop as shown in Figure (3.9b). The coercivity value in this case was predicted by Stoner and Wohlfarth to be the anisotropy field strength.

For cases where  $0^\circ < \phi < 90^\circ$  the moments undergo both reversible and irreversible changes. The hysteresis loops obtained from the cases in between the two extremes are a combination of both. Different values of  $\phi$  were investigated by Stoner and Wohlfarth and the investigations were repeated in this study for comparison. The hysteresis loops are shown in Figure (3.10) and are in good agreement with those obtained by Stoner and Wohlfarth (1991).

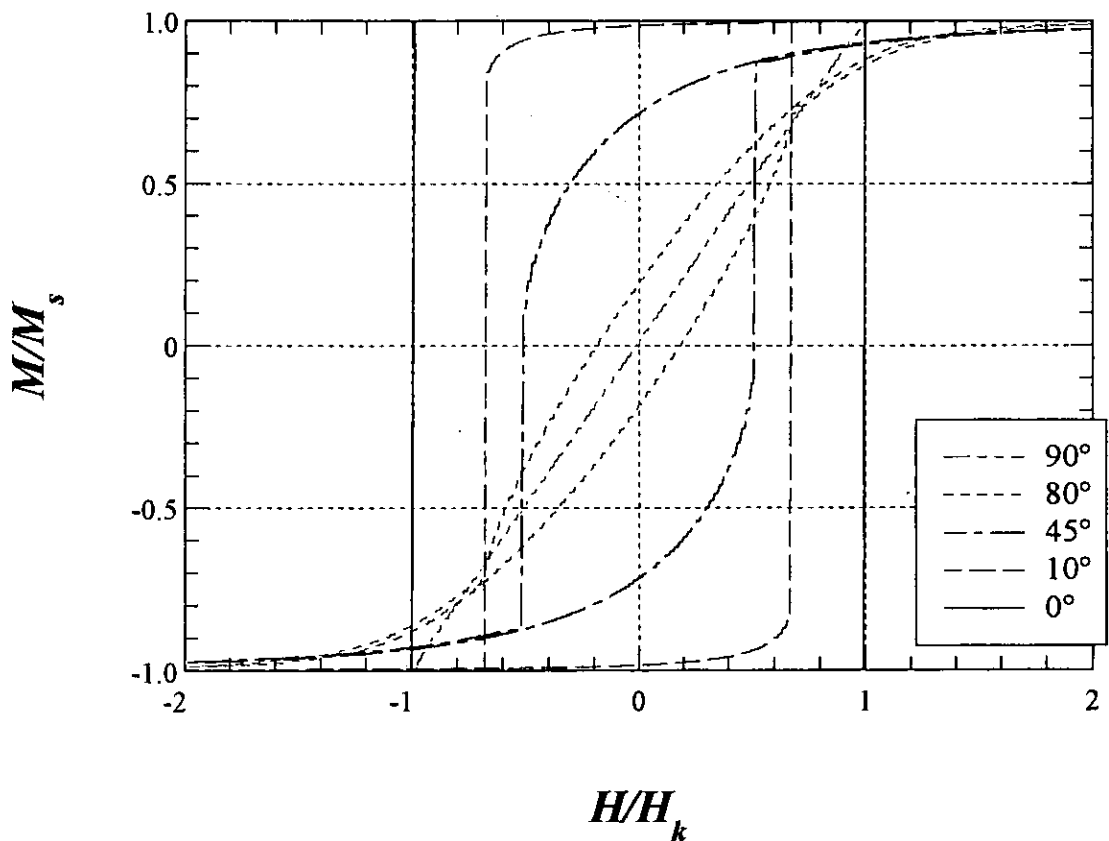


**Figure (3.10):Hysteresis loops illustrating the Stoner and Wohlfarth theory**

The anisotropy field,  $H_{anis}$ , can be determined from the energy equation (Equation(3.1)) using the following relationship between a field term,  $H$ , and an energy term,  $E$ , [Zhu]

$$H = -\frac{\partial E}{\partial M} \quad (3.9)$$

where  $M$  is the magnetisation represented by

$$M = M_s m \quad (3.10)$$

where  $m$  is the unit vector representing the reduced magnetisation.  $H$  can now be written as

$$H = -\frac{1}{M_s} \frac{\partial E}{\partial m} \quad (3.11)$$

substituting in the anisotropy energy equation (Equation (3.1)) gives

$$\begin{aligned} H_{anis} &= -\frac{1}{M_s} \frac{\partial (K \sin^2 \theta)}{\partial m} \\ &= -\frac{1}{M_s} \frac{\partial (K(1 - \cos^2 \theta))}{\partial m} \\ &= -\frac{1}{M_s} \frac{\partial (K(1 - (m \cdot k)^2))}{\partial m} \end{aligned} \quad (3.12)$$

where  $k$  was the unit vector representing the easy axis direction corresponding to the moment under observation, denoted here as the unit vector  $m$ . Differentiating gives

$$= \frac{2K (m \cdot k) k}{M_s} \quad (3.13)$$

therefore

$$\mathbf{H}_{anis} = H_k (\mathbf{m} \cdot \mathbf{k}) \mathbf{k} \quad (3.14)$$

It is usual practice in micromagnetic modelling to state the field terms in reduced units (Zhu and Bertram, 1988). This was done by dividing both sides of Equation (3.14) by the anisotropy field strength,  $H_k$ , to give a reduced anisotropy field,  $\mathbf{h}_{anis}$ . The reduced anisotropy field for each moment  $i$  was

$$\mathbf{h}_{anis}^i = (\mathbf{k}_i \cdot \mathbf{m}_i) \mathbf{k}_i \quad (3.15)$$

The anisotropy needed to be incorporated into the model by considering each of the grains represented by Voronoi polygons. These typically have a random distribution of easy axes in the thin film plane (Richter, 1999). To represent the easy axis, a random direction was associated with each of the grains in the model. This was achieved by randomly generating numbers in the range  $[0, 2\pi]$  to represent  $\phi$ , the angle measured from the field direction (the  $x$ -axis) to the easy axis.

The reduced anisotropy field was calculated for all the real seed and corresponding nodal points and then contributed to the total field calculation.

### 3.4.2 The External Field

If an external field is applied to a moment, the moment will rotate in order to align itself in the same direction as the applied field. In this model the external field was applied in the longitudinal direction ( $x$ ). It was initially set at a large positive value and reduced in small steps to a final large negative value. The energy term due to an externally applied field,  $\mathbf{H}_{ext}$ , is given by

$$E_{ext} = -\mathbf{M} \cdot \mathbf{H}_{ext} \quad (3.16)$$

As in the case for the anisotropy field, the external field is expressed in reduced units, i.e.

$$h_{ext} = \frac{H_{ext}}{H_k} \quad (3.17)$$

### 3.4.3 The Exchange Field

As well as the anisotropy effect there are other forces acting on the system of particles, one of them being exchange forces which will now be described. As discussed in the previous chapter, an important characteristic of ferromagnetic materials is their spontaneous magnetisation in the absence of an applied field. In 1928 Hiesenberg discovered that this magnetisation was due to the alignment of the moments which he said to be a result of the exchange forces present. This is a quantum-mechanical effect which is basically due to the interaction between the spin of electrons from neighbouring atoms. It is therefore a short-range effect. Cullity (1972) discusses the theory in more detail and provides the following equation for the exchange energy generated between two atoms

$$E_{ex} = -2J^* S_i \cdot S_j = -2J^* S_i S_j \cos\phi \quad (3.18)$$

where  $J^*$  is the exchange integral and  $\phi$  is the angle between the spins  $S_i$  and  $S_j$ . It can be seen that in order for there to be minimum exchange energy the two spins must be parallel to each other and  $J^*$  to be a positive value. A maximum value is obtained when the spins are anti-parallel. The exchange energy of the system is a summation of the exchange between all the pairs of nearest atoms i.e.

$$E_{ex} = -2J^* \sum_i \sum_j S_i \cdot S_j \quad (3.19)$$

To incorporate exchange into the model, the above equation can be written in terms of magnetic moments instead of spins.

Consider the exchange field of a particular moment. There is an exchange coupling generated between moments within the same grain and also one between moments,

across grain boundaries, that share the same geometric point. The exchange field calculation is represented as (Tako, thesis):

$$H_{exch}^i = \frac{2A}{M_s} \sum_{j \neq i}^n \frac{m_j \eta_{ij}}{r_{ij}^2} + 2J^* M_s \sum_{l \neq i}^k m_l (1 - \eta_{il}) \quad (3.20)$$

where  $A$  is the exchange constant. The first summation is the total exchange generated from the  $n$  moments within the same grain as moment  $i$ . The distance between moment  $i$  and moment  $j$  is represented as  $r_{ij}$ . The second summation is the exchange generated across the grain boundaries by the  $k$  moments sharing the same geometric point as moment  $i$ , where  $k$  takes the value of either two or three. The function  $\eta_{ij}$  is defined as the following :

$$\eta_{ij} = \begin{cases} 1 & \text{for all } i, j \text{ in the same grain} \\ 0 & \text{otherwise} \end{cases}$$

This function, therefore, only includes the second part of the equation when the  $i$ th moment shares the same co-ordinates as two or three other moments. The cases when it is not included is when moment  $i$  is one of the original seed points.

Equation (3.20) was divided by  $H_k$  to give a calculation for the exchange field in reduced units,

$$h_{exch}^i = C_1^* \sum_{j \neq i}^n \frac{m_j \eta_{ij}}{r_{ij}^2} + C_2^* \sum_{l \neq i}^k m_l (1 - \eta_{il}) \quad (3.21)$$

where

$$C_1^* = \frac{2A}{H_k M_s L^2} \quad \text{and} \quad C_2^* = \frac{2J^* M_s}{H_k} \quad (3.22)$$

$C_1^*$  describes the strength of the exchange coupling between the grains. The second constant,  $C_2^*$ , is a measure of the strength of the exchange coupling across the grains.

The reduced exchange field acting on moment  $i$  contributes to the total field acting on that particular moment.

### 3.4.4 The Magnetostatic Field

The final effect incorporated into this model was the magnetostatic effect. This effect will be discussed in detail in the next chapter as it was the main topic of research. The magnetostatic calculation proves to be the most time consuming calculation in micromagnetic modelling since it is long range and should incorporate all the particles in the system. There are two methods used in this model in the hope of improving the computational efficiency. An accurate magnetostatic calculation based on surface and volume integrals was used on near neighbours. This was termed ‘The Exact Magnetostatic Calculation’ in the thesis. An ‘Approximate Dipole Calculation’ was used for long range interactions where the triangles were treated as interacting dipoles.

## 3.5. Modelling the Motion of the Magnetic Moment

The reduced total field,  $\mathbf{h}_{tot}^i$ , acting on a particular moment  $i$  has now been calculated and can be expressed as the following :

$$\mathbf{h}_{tot}^i = \mathbf{h}_{ext} + \mathbf{h}_{anis}^i + \mathbf{h}_{exch}^i + \mathbf{h}_{mag}^i \quad (3.23)$$

The motion of a magnetic moment under this field can be described by the Landau-Lifshitz equation (1935) shown below,

$$\frac{d\mathbf{M}}{dt} = \gamma(\mathbf{M} \times \mathbf{H}) - \frac{\lambda}{M_s}(\mathbf{M} \times (\mathbf{M} \times \mathbf{H})) \quad (3.24)$$

where  $\frac{d\mathbf{M}}{dt}$  is the rate of change of the magnetisation,  $\mathbf{M}$ , with time,  $t$ , and

$$M = M_s m \quad \text{and} \quad H = H_k h \quad (3.25)$$

Substituting Equation (3.25) into Equation (3.24),

$$M_s \frac{dm}{dt} = \gamma M_s H_k (m \times h) - \lambda M_s H_k (m \times (m \times h)) \quad (3.26)$$

which leads to

$$\frac{dm}{dt} = H_k [\gamma (m \times h) - \lambda (m \times (m \times h))] \quad (3.27)$$

Let

$$\tau = \gamma H_k t \quad \text{and} \quad \frac{d}{dt} = \gamma H_k \frac{d}{d\tau} \quad (3.28)$$

therefore

$$\gamma H_k \frac{dm}{d\tau} = H_k [\gamma (m \times h) - \lambda (m \times (m \times h))] \quad (3.29)$$

finally

$$\frac{dm}{d\tau} = m \times h - \alpha m \times (m \times h) \quad (3.30)$$

where

$$\alpha = \frac{\lambda}{\gamma}, \quad m = m_x i + m_y j, \quad h = h_x i + h_y j \quad (3.31)$$

This final equation (Equation (3.30)) is expressed in reduced units. The first part of the equation describes the precession of the moment around the field direction. The second term in the equation describes the motion of the moment being pulled in, or damped, towards the equilibrium position,  $\alpha$  is the damping constant. This equation of motion

has been used successfully in previous models (Zhu and Bertram, 1988; Tako, thesis; Schabes, 1991). These models, as well as this one, adopted the infinite damping case where the precession term was set to equal 0 and the damping constant to 1. The reason for this is usually to aid computer efficiency. Shabes (1991) justifies the use of infinite damping by stating that if the system is strongly exchanged coupled, the angle between the magnetisation and the applied field is small. The dynamical evolution towards equilibrium is therefore governed by the damping term. Victora (1987) found the calculations to be insensitive to the value of the damping constant used. However, Zhu and Bertram (1988) found a small decrease in the coercivity when  $\alpha$  was decreased from 1 to 0.1. They also found that values of  $\alpha$  above unity showed constant coercivity.

The reduced Landau-Lifshitz equation was then expanded as follows:

$$\frac{dm}{d\tau} = -\alpha m \times (m \times h) \quad (3.32)$$

expanding gives

$$\frac{dm_x}{d\tau} = -\alpha m_y (m_x h_y - m_y h_x) \quad \text{and} \quad \frac{dm_y}{d\tau} = \alpha m_x (m_x h_y - m_y h_x) \quad (3.33)$$

Now since

$$m = \cos\theta i + \sin\theta j \quad \text{and} \quad \frac{dm}{d\tau} = (-\sin\theta i + \cos\theta j) \frac{d\theta}{d\tau} \quad (3.34)$$

it follows that

$$\frac{d \cos\theta}{d\tau} = -\alpha \sin\theta (\cos\theta h_y - \sin\theta h_x) \quad \text{and} \quad \frac{d \sin\theta}{d\tau} = \alpha \cos\theta (\cos\theta h_y - \sin\theta h_x) \quad (3.35)$$

therefore

$$-\sin\theta \frac{d\theta}{d\tau} = -\alpha \sin\theta (\cos\theta h_y - \sin\theta h_x) \quad (3.36)$$

and

$$\cos\theta \frac{d\theta}{d\tau} = \alpha \cos\theta(\cos\theta h_y - \sin\theta h_x) \quad \text{via substitution.} \quad (3.37)$$

Equation (3.36) and Equation (3.37) are mathematically identical and can be written as

$$\frac{d\theta}{d\tau} = \alpha(\cos\theta h_y - \sin\theta h_x) \quad (3.38)$$

This resulting equation, Equation (3.38), was solved numerically using the Runge Kutta Method as described in the next section.

### 3.5.1 Solving The Landau-Lifshitz Equation

There are several methods of solving the Landau-Lifshitz equation. Zhu and Bertram (1988) used the Adams Predictor-Corrector method and Shabes (1991) used the Adams-Bashforth method to solve the dynamic equation. The method used to solve the Landau-Lifshitz equation in this study was the 4th order Runge-Kutta method as used successfully by Kay (thesis) and Victora (1987). Tako (thesis) compared both the Runge-Kutta and the Adams Predictor-Corrector. He suggested that for small systems, as used in this study, the Runge-Kutta method was adequate but for large complicated systems the Adams method proved to be more efficient. The Runge-Kutta method (Atkinson, 1993) is described below.

Equation (3.38) for simplicity represented the motion of one moment within the system. What needs to be solved is a system of differential equations incorporating all the moments within the system.

Given the system of differential equations,  $\frac{d\theta}{d\tau} = f(\theta, h)$  where

$$\theta = (\theta_1, \theta_2, \dots, \theta_n) \quad \text{where } n = \text{the number of moments in the system}$$

and

$$h = h_x i + h_y j$$

where

$$h_x = f_{hx}(\theta_1, \theta_2, \dots, \theta_n)$$

$$h_y = f_{hy}(\theta_1, \theta_2, \dots, \theta_n)$$

the first step of the Runge Kutta Method of solution is as follows:

*Let*  $\theta^0 = \text{initial value of } \theta$

*and*

$$k_1 = f(\theta^0)$$

$$k_2 = f\left(\theta^0 + \frac{h}{2}k_1\right)$$

$$k_3 = f\left(\theta^0 + \frac{h}{2}k_2\right)$$

$$k_4 = f(\theta^0 + hk_3)$$

$$\theta^1 = \theta^0 + \frac{h}{6}(k_1 + 2k_2 + 2k_3 + k_4)$$

*where*

$$f(\theta) = \cos\theta h_y - \sin\theta h_x$$

$h$  is regarded as the step length, set to 0.01, and  $\theta$  the angle associated with each moment such that,  $m = \cos\theta i + \sin\theta j$ .  $h_x$  is the reduced total field acting on that moment in the  $x$  direction and  $h_y$  the total field in the  $y$  direction.

The procedure of evaluating equilibrium points for the hysteresis loop was as follows:

1. Initially set

$$\theta = 0$$

$$h_{ext}^x = 2$$

2. Calculate

$$h = h_{ext} + h_{anis} + h_{exch} + h_{mag}$$

Determine new  $\theta^i$  using the Runge Kutta Method

3. Convergence check to see if equilibrium has been reached

$$| \text{old } \theta^i - \text{new } \theta^i | < \text{tol} \quad \text{tol} = 0.001 \text{ radians}$$

Replace old  $\theta$  with new  $\theta$

If the condition is satisfied for all variables:

Calculate and store the average magnetisation,

reduce  $h_{ext}^x$  by 0.01 and return to step 2.

If condition fails:

return to step 2

4. If  $h_{ext}^x = -2$ , then stop (end of loop)

New angles for all the moments were calculated via the Runge Kutta algorithm. A convergence check was carried out on all the new angles against the old ones with the tolerance set to 0.001 radians. Only when all the moments had reached a state of equilibrium, i.e. when there was no difference between the old  $\theta$  and the new one for all the moments, would the average magnetisation be plotted and the external field be

reduced. If this was not the case and all the moments had not reached equilibrium, the total field acting on each moment was calculated again using the updated  $\theta$ 's and put through the algorithm again. This procedure was repeated until all the moments had reached equilibrium for each particular field step.

The average magnetisation at each field step was expressed as the following:

$$\bar{M}_x = \frac{\sum M_x A}{\sum A} \quad (3.39)$$

where  $M_x$  is the average magnetisation, measured in the  $x$  direction, associated with each triangle and  $A$  the area of that particular triangle.

### 3.6 Summary

The theory behind the micromagnetic modelling process has been introduced. The generation of the model of the physical structure was described first. Most of the results obtained from the study were in the form of hysteresis loops. The theory behind hysteresis was described next. The contributions towards the total effective field acting on a moment in the system was then described which introduced the theoretical concepts behind the anisotropy, external and exchange fields. The chapter concluded by discussing the equation to model the motion of the moment together with the numerical method used to solve it. The magnetostatic field calculation was only briefly introduced but will be discussed in detail in the next chapter.

## 4. Calculating the Magnetostatic Field

### 4.1 Introduction

The most time consuming calculation in micromagnetic modelling is the magnetostatic field calculation. It is because of this a lot of research has been devoted to finding approximate solutions to this particular field calculation and improving the computation time.

In a model presented by Zhu and Bertram (1988), where the grains were represented by closely packed hexagons, the magnetostatic field calculation was based on a summation of the integration on grain surfaces. It was calculated exactly for the hexagon sides but the top and bottom surfaces were approximated by square surfaces. The calculation range was truncated to 7 grains in radius or 198 nearest neighbours.

In Lu *et al.*'s model (1992), one similar to Zhu and Bertram's, the magnetostatic interactions between near neighbours were calculated by dividing the grains into small elements and summing the dipole interaction fields between these elements. A mean field approximation was used to consider the effects from grains beyond the 5th neighbour. The self demagnetising field of each grain was also included in the calculation.

In Vecchio's model on 2D thin film using the finite element method (1989), the magnetostatic interaction was expressed as volume and surface charge densities. The surface charges in his model were ignored since they were not present on the top and bottom as a 2D magnetisation distribution was assumed. He also suggested that the surface charge density at the edge of the film could be approximated by a volume charge density which drops to zero as it approaches the edge.

The magnetostatic model used in this study has been previously used by Tako (thesis). It uses a combination of an exact calculation, based on surface and volume integrals,

together with an approximate solution based on dipoles. The first part of this chapter describes the approximate calculation. The exact magnetostatic calculation is then discussed together with the problems occurring from using this method. The final part of this chapter introduces the concept used to overcome the problems encountered when using the exact method.

## 4.2 Dipole Approximation

The system being studied comprises a set of irregularly shaped grains each of which has been divided into triangles, see Figure (3.7). In order to calculate the magnetostatic field at any point in the material, assume that each triangle,  $Q$ , acts as a dipole of moment  $\mu_j$  located at the centroid,  $j$ , of the triangle. Its magnitude is the volume of the triangular element and its direction is the average direction of the three moment directions at each vertex of the triangle, see Figure (4.1),

$$\text{i. e.} \quad \mu_j = M_s A_Q T m_j \quad (4.1)$$

where  $A_Q$  is the area of the triangle,  $T$  is the thickness of the material. Here the unit vector  $m_j$  is such that

$$m_j = \frac{(m_Q^{(1)} + m_Q^{(2)} + m_Q^{(3)})}{|m_Q^{(1)} + m_Q^{(2)} + m_Q^{(3)}|} \quad (4.2)$$

where  $m_Q^{(1)}$ ,  $m_Q^{(2)}$ ,  $m_Q^{(3)}$  are the magnetisation directions at each vertex of the triangle  $Q$ .

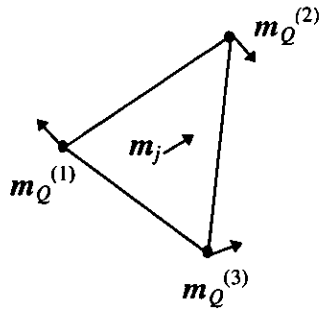


**Figure (4.1) : Illustrating the average magnetisation for each triangle**

The magnetostatic field at a particular point should consider contributions from all of the moments in the film. The calculation, therefore, proves to be very complex and time consuming. To overcome this, earlier models, as those described in Chapter 2.4., only worked out the exact magnetostatic field at a particular point due to moments within a prescribed radius of it. An approximate calculation, based on dipoles, was used on moments a further distance away and those even further away were ignored. Initial studies on the model omitted the exact calculation and the dipole approximation was used for all moments within a certain radius.

The triangles required in the calculation of the magnetostatic field at a point  $P$  were found by checking whether their centroids lay within a given radius,  $r_2$ , from  $P$ , see Figure (4.2).

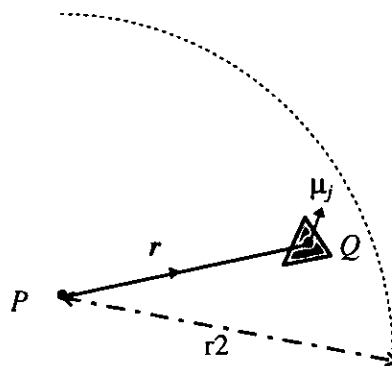


**Figure (4.2) : Illustrating field at  $P$  due to dipole at  $Q$**

The magnetostatic field at  $P$  due to the dipole at  $j$  is given by

$$\mathbf{H}_{mag} = -\frac{\boldsymbol{\mu}}{|\mathbf{r}|^3} + \frac{3(\boldsymbol{\mu} \cdot \mathbf{r})\mathbf{r}}{|\mathbf{r}|^5} \quad (4.3)$$

where  $|\mathbf{r}|$  is the distance between  $P$  and  $j$ , and  $\boldsymbol{\mu}$  is the dipole moment at  $Q$ .

This equation only accounts for one of the dipoles. To include all the dipoles within a given radius of  $P$ , Equation (4.3) was summed:

$$\mathbf{H}_{mag}^P = \sum_{j \neq P}^n \left( -\frac{\boldsymbol{\mu}_j}{|\mathbf{r}_{Pj}|^3} + \frac{3(\boldsymbol{\mu}_j \cdot \mathbf{r}_{Pj})\mathbf{r}_{Pj}}{|\mathbf{r}_{Pj}|^5} \right) \quad (4.4)$$

where  $|\mathbf{r}_{Pj}|$  is the distance between node  $P$  and the centroid,  $j$  of triangle  $Q$ . Substituting Equation (4.1),

$$\mathbf{H}_{mag}^P = TM_s \sum_{j \neq P}^n A_Q \left( -\frac{\mathbf{m}_j}{|\mathbf{r}_{Pj}|^3} + \frac{3(\mathbf{m}_j \cdot \mathbf{r}_{Pj})\mathbf{r}_{Pj}}{|\mathbf{r}_{Pj}|^5} \right) \quad (4.5)$$

Now

$$A_Q = L^2 a_Q \quad \text{and} \quad |\mathbf{r}_{Pj}| = L |\mathbf{r}'_{Pj}| \quad (4.6)$$

where  $a_Q$  is the relative area of triangle  $Q$ .  $L$  is the length scale, i. e. the length of the cell, and  $|\mathbf{r}'_{Pj}|$  is the scaled distance between node  $P$  and the centroid  $j$ .

Substituting Equation (4.6) into Equation (4.5),

$$\mathbf{H}_{mag}^P = H_{int} \sum_{j \neq P}^n a_Q \left( -\frac{\mathbf{m}_j}{|\mathbf{r}'_{Pj}|^3} + \frac{3(\mathbf{m}_j \cdot \mathbf{r}'_{Pj})\mathbf{r}'_{Pj}}{|\mathbf{r}'_{Pj}|^5} \right)$$

where (4.7)

$$H_{int} = \frac{TM_s}{L}$$

Both sides of Equation (4.7) were divided by  $H_k$  to give the reduced magnetostatic field,

$$\mathbf{h}_{mag}^P = h_{int} \sum_{j \neq P}^n a_Q \left( -\frac{\mathbf{m}_j}{|\mathbf{r}'_{Pj}|^3} + \frac{3(\mathbf{m}_j \cdot \mathbf{r}'_{Pj})\mathbf{r}'_{Pj}}{|\mathbf{r}'_{Pj}|^5} \right)$$

where

$$\mathbf{h}_{mag}^P = \frac{\mathbf{H}_{mag}^P}{H_k} \quad \text{and} \quad h_{int} = \frac{H_{int}}{H_k}$$

(4.8)

$\mathbf{h}_{mag}^P$  is the reduced magnetostatic field at moment  $P$  due to a summation of the dipole fields from  $n$  triangles. The magnetostatic field is calculated at all nodes and contributes to the total field. Since the magnetostatic field is only dependent on the geometric position of the moments, the field at the moments that share the same vertex is the same irrespective of which grain they belong to. Therefore to improve computational efficiency, the magnetostatic field is only calculated at distinct points and then transferred to the moments with matching co-ordinates.

### 4.3 Exact Calculation

This calculation is based on the assumption that volume and surface charges are present within the system and was used in a previous model by Tako (thesis). Surface charges arise due to a discontinuity in the magnetisation across a boundary between two particles, as each is assumed to have different magnetisations. The surface charge ( $\sigma$ ) can be represented as

$$\sigma = \mathbf{M} \cdot \mathbf{n} = M \cos \vartheta \quad (4.9)$$

where  $\vartheta$  is the angle between the magnetisation ( $\mathbf{M}$ ) and the normal to the surface at the point at which  $\sigma$  is to be calculated, represented by the unit vector  $\mathbf{n}$ . It is the free poles at the surface that cause the charges and these free poles may also exist within the volume of the particle. Here the free poles are due to spatial variation of the magnetisation within the particle. The volume charge ( $\rho$ ) can be represented as

$$\rho = -\nabla \cdot \mathbf{M} \quad (4.10)$$

These two charges are incorporated into a more accurate magnetostatic calculation represented as the following (Tako, thesis).

$$\mathbf{H}_d = \int_{v'} \frac{-\nabla' \cdot \mathbf{M}'(\mathbf{r}')(\mathbf{r} - \mathbf{r}') dv'}{|\mathbf{r} - \mathbf{r}'|^3} + \int_{s'} \frac{\mathbf{M}'(\mathbf{r}') \cdot \mathbf{n}(\mathbf{r} - \mathbf{r}') ds'}{|\mathbf{r} - \mathbf{r}'|^3} \quad (4.11)$$

The first part of the Equation (4.11) is a three fold integration over the volume and the second part represents a two fold integration over the surface. The region over which the integrations take place can be seen in Figure (4.3).

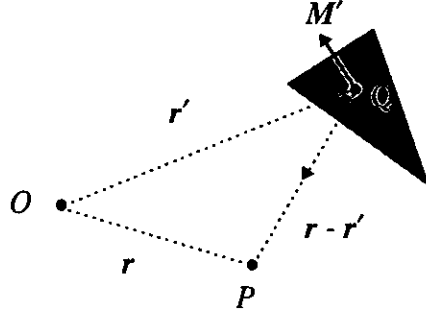


**Figure (4.3): Illustration showing the region to be integrated**

$P$  is the point where the magnetostatic field is to be evaluated.  $Q$  is one of the triangles which contribute towards this field and has a linearly varying magnetisation  $\mathbf{M}'$ . The surface and volume integrals need to be calculated over a number of such triangles.

Since the study is on thin films, it is assumed that the magnetisation along the  $z$ -direction is zero and does not contribute to the integration leaving a surface and line integral. The constant taken out represents the thickness of the film,  $T$  (see Equation (4.12)). The magnetisation within each triangle is assumed to vary linearly and therefore  $\text{div } \mathbf{M}'$  is also constant and can be taken out as follows

$$\mathbf{H}_d = T \left[ -\nabla' \cdot \mathbf{M}'(\mathbf{r}') \int_{s'} \frac{(\mathbf{r} - \mathbf{r}') ds'}{|\mathbf{r} - \mathbf{r}'|^3} + \int_{l'} \frac{\mathbf{M}'(\mathbf{r}') \cdot \mathbf{n}(\mathbf{r} - \mathbf{r}') dl'}{|\mathbf{r} - \mathbf{r}'|^3} \right] \quad (4.12)$$

The integrals are now evaluated over the surface area of a triangle and the perimeter around it.

An approach taken by Tako (thesis) was used to simplify this integral. He suggested rotating the axes by an angle of  $\theta$  so that one side of the triangle lies parallel to the  $x$ -axis, see Figure (4.4).

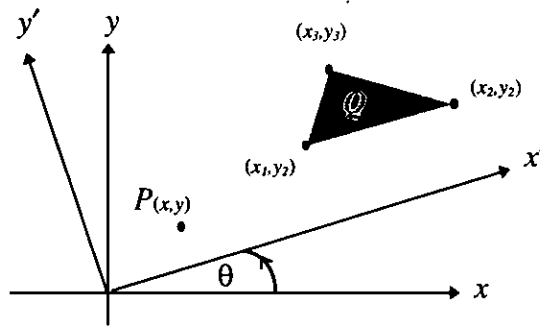


Figure (4.4): Rotating the axes to simplify the integrals

### 4.3.1 Evaluating The Surface Integral

The evaluation of the surface integral,  $h_{surf}$ , is considered first where

$$h_{surf} = \int_{s'} \frac{(\mathbf{r} - \mathbf{r}') dx' dy'}{|\mathbf{r} - \mathbf{r}'|^3} \quad (4.13)$$

The integral can be expressed as an  $x$  and  $y$  component, i.e.

$$\mathbf{h}_{surf} = h_{surf}^x \mathbf{i} + h_{surf}^y \mathbf{j} \quad (4.14)$$

and the  $x$  component, illustrated in Figure (4.5), is considered first.

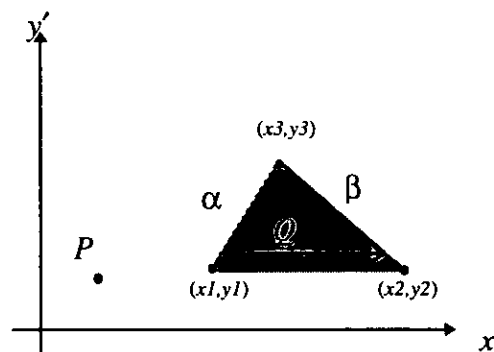


Figure (4.5): Illustrating the  $x$  component of the surface integral

The limits for the  $x'$  integration to cover region  $Q$  are  $x'=\alpha$  to  $x'=\beta$  where

$$\alpha = x1 + s_1^*(y' - y1)$$

$$\beta = x2 + s_2^*(y' - y1)$$

$$s_1^* = \frac{(x3 - x1)}{(y3 - y1)} \quad \text{and} \quad s_2^* = \frac{(x3 - x2)}{(y3 - y1)} \quad (4.15)$$

The  $x$  component can be written as

$$\begin{aligned} h_{surf}^x &= \int_{y'=y1}^{y'=y3} dy' \int_{x'=\alpha}^{x'=\beta} \frac{(x - x') dx'}{[(x - x')^2 + (y - y')^2]^{\frac{3}{2}}} \\ &= \int_{y'=y1}^{y'=y3} \frac{dy'}{\sqrt{(x - \beta)^2 + (y - y')^2}} - \int_{y'=y1}^{y'=y3} \frac{dy'}{\sqrt{(x - \alpha)^2 + (y - y')^2}} \\ &= h_{surf}^{x1} - h_{surf}^{x2} \end{aligned} \quad (4.16)$$

Evaluating  $h_{surf}^{x1}$  first

$$h_{surf}^{x1} = \int_{y'=y1}^{y'=y3} \frac{dy'}{\sqrt{(x - x2 - s_2^*(y' - y1))^2 + (y - y')^2}} \quad (4.17)$$

By completing the square within the square root of Equation (4.17) gives

$$h_{surf}^{x1} = \frac{1}{\sqrt{1 + s_2^{*2}}} \int_{y'=y1}^{y'=y3} \frac{dy'}{\sqrt{(y' - d)^2 + f^2}} \quad (4.18)$$

where

$$d = \frac{y + s_2^*((x - x2) + y1s_2^*)}{1 + s_2^{*2}} \quad (4.19)$$

$$f = \frac{ys_2^* - ((x - x2) + y1s_2^*)}{1 + s_2^{*2}} \quad (4.20)$$

This standard integral, Equation (4.18), is evaluated to give

$$h_{surf}^{x1} = \frac{1}{\sqrt{1+s_2^2}} \ln \left[ \frac{(y3-d) + \sqrt{(y3-d)^2 + f^2}}{(y1-d) + \sqrt{(y1-d)^2 + f^2}} \right] \quad (4.21)$$

$h_{surf}^{x2}$  can be evaluated in the same way to give

$$h_{surf}^{x2} = \frac{1}{\sqrt{1+s_1^2}} \ln \left[ \frac{(y3-d^*) + \sqrt{(y3-d^*)^2 + f^{*2}}}{(y1-d^*) + \sqrt{(y1-d^*)^2 + f^{*2}}} \right] \quad (4.22)$$

where

$$d^* = \frac{y + s_1^* ((x - x1) + y1s_1^*)}{1 + s_1^{*2}} \quad (4.23)$$

$$f^* = \frac{ys_1^* - ((x - x1) + y1s_1^*)}{1 + s_1^{*2}} \quad (4.24)$$

Now consider the y component. The triangle was divided into two sub-regions A and B, see Figure (4.6), as suggested by Tako (thesis) and the surface integral in terms of the y component becomes

$$h_{surf}^y = h_A^y + h_B^y \quad (4.25)$$

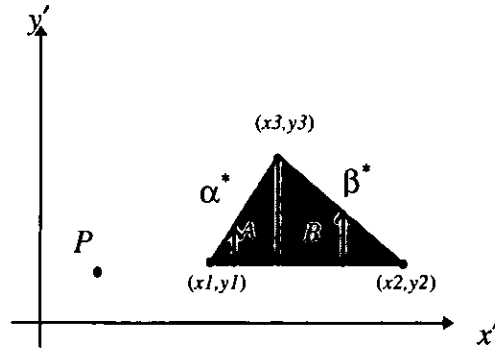


**Figure (4.6): Dividing triangle into regions A and B in order to calculate the y component**

The y component in region A is calculated from  $y = 1$  to  $\alpha^*$  and in region B it is calculated from  $y = 1$  to  $\beta^*$ , where

$$\alpha^* = y1 + s_1(x' - x1)$$

$$\beta^* = y1 + s_2(x' - x2)$$

$$s_1 = \frac{1}{s_1^*} = \frac{(y3 - y1)}{(x3 - x1)} \quad \text{and} \quad s_2 = \frac{1}{s_2^*} = \frac{(y3 - y1)}{(x3 - x2)} \quad (4.26)$$

Consider the y component in region A first. This can be expressed as

$$\begin{aligned} h_A^y &= \int_{x'=x1}^{x'=x3} dx' \int_{y'=y1}^{y'=\alpha^*} \frac{(y - y') dy'}{[(x - x')^2 + (y - y')^2]^{\frac{1}{2}}} \\ &= \int_{x'=x1}^{x'=x3} \frac{dx'}{\sqrt{(x - x')^2 + (y - \alpha^*)^2}} - \int_{x'=x1}^{x'=x3} \frac{dx'}{\sqrt{(x - x')^2 + (y - y1)^2}} \\ &= h_A^{y1} - h_A^{y2} \end{aligned} \quad (4.27)$$

Evaluating  $h_A^{y1}$  first

$$h_A^{y1} = \int_{x'=x1}^{x'=x3} \frac{dx'}{\sqrt{(x-x')^2 + (y-y1 - s_1(x'-x1))^2}} \quad (4.28)$$

By completing the square within the square root of Equation (4.28) as previously, gives

$$h_A^{y1} = \frac{1}{\sqrt{1+s_1^2}} \int_{x'=x1}^{x'=x3} \frac{dx'}{\sqrt{(x'-u)^2 + v^2}} \quad (4.29)$$

where

$$u = \frac{x + s_1((y-y1) + x1s_1)}{1+s_1^2} \quad (4.30)$$

$$v = \frac{xs_1 - ((y-y1) + x1s_1)}{1+s_1^2} \quad (4.31)$$

The solution to this standard integral, Equation (4.29), can be shown to equal

$$h_A^{y1} = \frac{1}{\sqrt{1+s_1^2}} \ln \left[ \frac{(x3-u) + \sqrt{(x3-u)^2 + v^2}}{(x1-u) + \sqrt{(x1-u)^2 + v^2}} \right] \quad (4.32)$$

Using the same methods, the solution to the standard integral  $h_A^{y2}$  can be shown to equal

$$h_A^{y2} = \ln \left[ \frac{(x-x3) + \sqrt{(x-x3)^2 + (y-y1)^2}}{(x-x1) + \sqrt{(x-x1)^2 + (y-y1)^2}} \right] \quad (4.33)$$

Next, consider the y component in region B which can be expressed as

$$h_B^y = \int_{x'=x3}^{x'=x2} \int_{y'=y1}^{y'=\beta^*} \frac{(y-y')dy'}{[(x-x')^2 + (y-y')^2]^{\frac{1}{2}}} \quad (4.34)$$

By using the same methods as before, this integral, Equation (4.34), can be expressed as

$$\begin{aligned} h_B^y &= \int_{x'=x3}^{x'=x2} \frac{dx'}{\sqrt{(x-x')^2 + (y-\beta^*)^2}} - \int_{x'=x3}^{x'=x2} \frac{dx'}{\sqrt{(x-x')^2 + (y-y1)^2}} \\ &= h_B^{y1} - h_B^{y2} \end{aligned} \quad (4.35)$$

By completing the square and evaluating the resulting standard integral

$$h_B^{y1} = \frac{1}{\sqrt{1+s_2^2}} \ln \left[ \frac{(x2-u^*) + \sqrt{(x2-u^*)^2 + v^{*2}}}{(x3-u^*) + \sqrt{(x3-u^*)^2 + v^{*2}}} \right] \quad (4.36)$$

where

$$u^* = \frac{x + s_2((y-y1) + x2s_2)}{1 + s_2^2} \quad (4.37)$$

$$v^* = \frac{xs_2 - ((y-y1) + x2s_2)}{1 + s_2^2} \quad (4.38)$$

The evaluation of the second integral in Equation (4.35) by similar methods equals

$$h_B^{y2} = \ln \left[ \frac{(x-x2) + \sqrt{(x-x2)^2 + (y-y1)^2}}{(x-x3) + \sqrt{(x-x3)^2 + (y-y1)^2}} \right] \quad (4.39)$$

### 4.3.2 Evaluating The Line Integral

As a reminder, the line integral is expressed as

$$\mathbf{h}_{line} = \int_{r'} \frac{\mathbf{M}'(\mathbf{r}') \cdot \mathbf{n}(\mathbf{r} - \mathbf{r}') dl'}{|\mathbf{r} - \mathbf{r}'|^3} \quad (4.40)$$

The magnetisation is normalised to give

$$\mathbf{h}_{line} = \int \frac{\mathbf{m}'(\mathbf{r}) \cdot \mathbf{n}(\mathbf{r} - \mathbf{r}') dl'}{|\mathbf{r} - \mathbf{r}'|^3} \quad (4.41)$$

where

$$\mathbf{m}' = \frac{\mathbf{M}'}{M_s} \quad (4.42)$$

The integral is carried out along the perimeter of the triangle such that

$$\begin{aligned} dl' &= \sqrt{dx'^2 + dy'^2} \\ &= dx' \sqrt{1 + \left(\frac{dy'}{dx'}\right)^2} \end{aligned} \quad (4.43)$$

Substituting Equation (4.43) into the integral Equation (4.41) gives

$$\mathbf{h}_{line} = \int \frac{\mathbf{m}'(\mathbf{r}) \cdot \mathbf{n}(\mathbf{r} - \mathbf{r}') dx'}{|\mathbf{r} - \mathbf{r}'|^3} \sqrt{1 + \left(\frac{dy'}{dx'}\right)^2} \quad (4.44)$$

This integral has to be evaluated three times representing each side of the triangle. The side to be evaluated is rotated so that it lies parallel to the x axis. The gradient of the line in this case is zero, thus reducing the integral, Equation (4.44), to

$$\mathbf{h}_{line} = \int \frac{\mathbf{m}'(\mathbf{r}) \cdot \mathbf{n}(\mathbf{r} - \mathbf{r}') dx'}{|\mathbf{r} - \mathbf{r}'|^3} \quad (4.45)$$

The magnetisation within the triangle is assumed to vary linearly, i.e.

$$\begin{aligned} m'_x &= a_1 + b_1x' + c_1y' \\ m'_y &= a_2 + b_2x' + c_2y' \end{aligned} \quad (4.46)$$

The constants in the equations can be calculated since  $m_x$  and  $m_y$  are known at the vertices of each triangle. For example, consider the triangle in Figure (4.7).

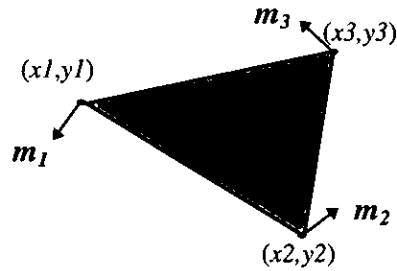


**Figure (4.7): A typical triangle illustrating magnetisation at the vertices**

The magnetisation at the vertices should equal

$$\begin{aligned} \left. \begin{aligned} m_{1x} &= a_1 + b_1x_1 + c_1y_1 \\ m_{1y} &= a_2 + b_2x_1 + c_2y_1 \end{aligned} \right\} m_1 \\ \\ \left. \begin{aligned} m_{2x} &= a_1 + b_1x_2 + c_1y_2 \\ m_{2y} &= a_2 + b_2x_2 + c_2y_2 \end{aligned} \right\} m_2 \\ \\ \left. \begin{aligned} m_{3x} &= a_1 + b_1x_3 + c_1y_3 \\ m_{3y} &= a_2 + b_2x_3 + c_2y_3 \end{aligned} \right\} m_3 \end{aligned} \quad (4.47)$$

Given the values of the magnetisations at the vertices, the constants in the linear equations for the magnetisation within the triangle can be calculated by methods of elimination.

The line integral contains the dot product between the magnetisation and the normal to the surface. This can be represented as the following

$$\begin{aligned}
\mathbf{m}' \cdot \mathbf{n} &= (a_1 + b_1x' + c_1y')n_x + (a_2 + b_2x' + c_2y')n_y \\
&= (a_1n_x + a_2n_y) + (b_1n_x + b_2n_y)x' + (c_1n_x + c_2n_y)y' \\
&= d_1 + d_2x' + d_3y'
\end{aligned} \tag{4.48}$$

where

$$\begin{aligned}
d_1 &= a_1n_x + a_2n_y \\
d_2 &= b_1n_x + b_2n_y \\
d_3 &= c_1n_x + c_2n_y
\end{aligned} \tag{4.49}$$

The line integral can now be written as

$$h_{line} = \int \frac{(d_1 + d_2x' + d_3y')(r - r')dx'}{|r - r'|^3} \tag{4.50}$$

Now since the line lies parallel along the  $x$  axis, it has a constant  $y$  value, say  $y'=c$ . The line integral can be simplified further by making this substitution to give

$$h_{line} = \int \frac{(d_4 + d_2x')(r - r')dx'}{|r - r'|^3} \tag{4.51}$$

where

$$d_4 = d_1 + d_3c \tag{4.52}$$

Equation (4.51) can now be divided into its  $x$  and  $y$  components, i.e.,

$$h_{line}^x = \int \frac{(d_4 + d_2x')(x - x')dx'}{[(x - x')^2 + (y - c)^2]^{\frac{3}{2}}} \tag{4.53}$$

$$h_{line}^y = \int \frac{(d_4 + d_2x')(y - c)dx'}{[(x - x')^2 + (y - c)^2]^{\frac{3}{2}}} \tag{4.54}$$

The limits on the integrals will be from  $x_1$  to  $x_2$ ,  $x_2$  to  $x_3$  and  $x_3$  to  $x_1$ . The triangle is rotated between each integration ensuring that the line to be evaluated lies parallel to the  $x$  axis.

The  $x$  component, Equation (4.53), is considered first and can be written as

$$\begin{aligned} h_{line}^x &= \int \frac{d_4 x - d_4 x' + d_2 x' x - d_2 x'^2 dx'}{[(x - x')^2 - (y - c)^2]^{\frac{1}{2}}} \\ &= \int \frac{-d_2 x'^2 + (d_2 x - d_4)x' + d_4 x}{[(x - x')^2 - (y - c)^2]^{\frac{1}{2}}} dx' \end{aligned} \quad (4.55)$$

This can be evaluated by first letting  $X=(x-x')$  and  $Y=(y-c)$

$$h_{line}^x = \int \frac{d_2 X^2 - (d_2 x + d_4)X}{[X^2 + Y^2]^{\frac{1}{2}}} dX \quad (4.56)$$

Now let

$$I = d_2 \int \frac{X^2}{[X^2 + Y^2]^{\frac{1}{2}}} dX \quad (4.57)$$

and

$$J = \int \frac{(d_2 x + d_4)X}{[X^2 + Y^2]^{\frac{1}{2}}} dX \quad (4.58)$$

$I$  can be written as

$$I = d_2 \int \frac{X^2 + Y^2}{[X^2 + Y^2]^{\frac{1}{2}}} dX - d_2 \int \frac{Y^2}{[X^2 + Y^2]^{\frac{1}{2}}} dX \quad (4.59)$$

The first integral in Equation (4.59) can be evaluated easily and the second by letting  $X=Y\tan U$  which gives

$$I = d_2 \ln(X + \sqrt{X^2 + Y^2}) - \frac{d_2 X}{\sqrt{X^2 + Y^2}} \quad (4.60)$$

$J$  can be evaluated by letting  $U = X^2 + Y^2$  giving

$$J = -\frac{(d_2x + d_4)}{\sqrt{X^2 + Y^2}} \quad (4.61)$$

Therefore, the solution to the  $x$  component of the line integral is

$$h_2^x = \left[ d_2 \ln[(x - x') + \sqrt{(x - x')^2 + (y - c)^2}] + \frac{(d_4 + d_2x')}{\sqrt{(x - x')^2 + (y - c)^2}} \right]_{x'=x}^{x'=x''} \quad (4.62)$$

where the limits  $x^*$  and  $x^{**}$  represent either  $x1$  and  $x2$ ,  $x2$  and  $x3$ , or  $x3$  and  $x1$  respectively.

Incorporating the limits gives

$$h_{line}^x = d_2 \ln \left[ \frac{(x - x^{**}) + \sqrt{(x - x^{**})^2 + (y - c)^2}}{(x - x^*) + \sqrt{(x - x^*)^2 + (y - c)^2}} \right] + \frac{(d_2 + d_4x^{**})}{\sqrt{(x - x^{**})^2 + (y - c)^2}} - \frac{(d_2 + d_4x^*)}{\sqrt{(x - x^*)^2 + (y - c)^2}} \quad (4.63)$$

The  $y$  component of the line integral, Equation (4.54) is now considered and can be written as

$$h_{line}^y = \int \frac{d_4(y - c) + d_2x'(y - c)dx'}{[(x - x')^2 + (y - c)^2]^{\frac{3}{2}}} \quad (4.64)$$

This can be solved using similar techniques as for the  $x$  component. First, let  $X=(x-x')$  and  $Y=(y-c)$  and substitute into the integral to give

$$h_{line}^y = \int \frac{d_2YX - Y(d_4 + d_2x)}{[X^2 + Y^2]^{\frac{3}{2}}} dX \quad (4.65)$$

Now let

$$I = d_2 Y \int \frac{X}{[X^2 + Y^2]^{\frac{3}{2}}} dX \quad (4.66)$$

and

$$J = -(d_4 + d_2 x) \int \frac{Y}{[X^2 + Y^2]^{\frac{3}{2}}} dX \quad (4.67)$$

By letting  $U = X^2 + Y^2$   $I$  can be solved to give

$$I = \frac{-d_2 Y}{\sqrt{X^2 + Y^2}} \quad (4.68)$$

and by letting  $X = Y \tan U$ ,  $J$  can be solved to give

$$J = -\frac{(d_4 + d_2 x) X}{Y \sqrt{X^2 + Y^2}} \quad (4.69)$$

The  $y$  component of the line integral can now be written as

$$h_{line}^y = \left[ \frac{-d_2 (y-c)^2 - (d_4 + d_2 x)(x-x')}{(y-c)\sqrt{(x-x')^2 + (y-c)^2}} \right]_{x'=x^*}^{x'=x^{**}} \quad (4.70)$$

where the limits are as before. This gives

$$h_{line}^y = \left[ \frac{d_2 (y-c)^2 + (d_4 + d_2 x)(x-x^*)}{(y-c)\sqrt{(x-x^*)^2 + (y-c)^2}} \right] - \left[ \frac{d_2 (y-c)^2 + (d_4 + d_2 x)(x-x^{**})}{(y-c)\sqrt{(x-x^{**})^2 + (y-c)^2}} \right] \quad (4.71)$$

The exact magnetostatic field can now be written as

$$\mathbf{H}_d = TM_s [-\nabla' \cdot \mathbf{m}'(\mathbf{r}') \mathbf{h}_{surf} + \mathbf{h}_{line}] \quad (4.72)$$

From Equation (4.46)

$$\nabla' \cdot \mathbf{m}' = b_1 + c_2 \quad (4.73)$$

where  $b_1$  and  $c_2$  can be obtained using methods of elimination.

Equation (4.72) is then reduced by dividing by  $H_k$  and normalised to the length of the cell as in the dipole approximation. This gives

$$\mathbf{h}_d = h^* \left[ -(b_1 + c_2) \mathbf{h}_{surf} + \mathbf{h}_{line} \right] \quad (4.74)$$

where

$$h^* = \frac{TM_s}{H_k L} = \frac{TM_s^2}{2KL} \quad (4.75)$$

### 4.3.3 Incorporating the magnetostatic calculation into the model

Figure (4.8) illustrates the regions in which each calculation was performed. Here  $P$  is the point at which the magnetostatic field is calculated.  $r1$  is the radius of the region closest to  $P$  and  $r2$  is the radius of the region of triangles to be included in the magnetostatic calculation.

The dipole approximation was first introduced into the model and included all the triangles within the outer radius  $r2$ , even the ones nearest to  $P$ . Hysteresis plots were drawn and can be seen in the results chapter (Chapter 5).

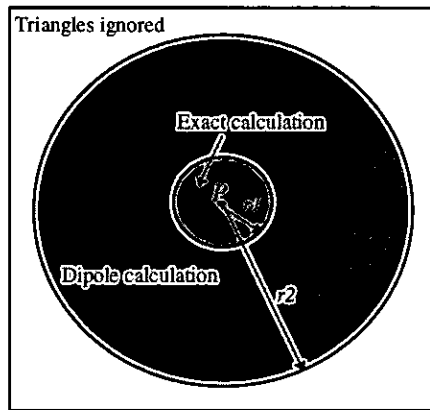


**Figure (4.8): The cell represents the system of triangles and highlights the regions where the exact and dipole calculations are carried out on a given point  $P$**

The exact calculation was next introduced into the model which calculated the magnetostatic field due to the triangles within the radius  $r_1$  from  $P$ . The dipole calculation was now used only on the triangles within the region  $(r_2-r_1)$ .

It was with the introduction of the exact calculation that the model encountered problems. The exact calculation had been previously used by Tako (thesis) but it was unclear how the problems were solved. The next section highlights the problems that arose with this calculation.

#### **4.3.4 Problems with the exact calculation**

The problems arose when trying to evaluate the contribution to the field from the surface charge  $(\mathbf{m} \cdot \mathbf{n})$ , in Equation (4.40). They occurred when trying to evaluate the field at one of the vertices of a triangle around which the integral was being calculated. The integral was found to diverge. The following is an example of such a case.

Let the triangle have vertices at  $(0,0)$ ,  $(1,0)$  and  $(0,1)$  as illustrated below in Figure (4.9),

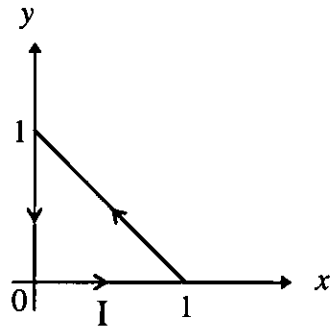


**Figure (4.9): Illustrating the triangle to be integrated**

Consider the integral along I where

$$n = -j$$

$$y' = 0$$

$$dl' = dx'$$

which gives, from Equation (4.46)

$$\begin{aligned} m'(r) \cdot n &= -(a_2 + b_2 x' + c_2 y')j \cdot j \\ &= -(a_2 + b_2 x') \end{aligned} \quad (4.76)$$

and

$$\begin{aligned} r - r' &= (x - x')i + (y - y')j \\ &= (x - x')i + yj \end{aligned} \quad (4.77)$$

The integral along I is

$$H_I = -T \int_0^1 \frac{(a_2 + b_2 x')(x - x')i + yj}{((x - x')^2 + y^2)^{3/2}} dx' \quad (4.78)$$

Rearranging into its components, the integral becomes

$$H_I(x, y) = -Ti \int_0^1 \frac{(a_2 + b_2 x')(x - x')}{((x - x')^2 + y^2)^{3/2}} dx' - Tj \int_0^1 \frac{(a_2 + b_2 x')y}{((x - x')^2 + y^2)^{3/2}} dx' \quad (4.79)$$

Now evaluating this at one of the vertices of the triangle, say (0,0), the integral becomes

$$\begin{aligned} H_I(0,0) &= -Ti \int_0^1 \frac{(a_2 + b_2 x')(-x')}{x'^3} dx' + 0j \\ &= Ti \int_0^1 \left( \frac{a_2}{x'^2} + \frac{b_2}{x'} \right) dx' \\ &= Ti \left[ \frac{-a_2}{x'} + b_2 \ln x' \right]_0^1 \\ &= Ti \left[ -a_2 + \lim_{x' \rightarrow 0} \left( \frac{-a_2}{x'} + b_2 \ln x' \right) \right] \end{aligned} \quad (4.80)$$

i.e. the integral diverges

The same problem occurs when trying to evaluate at the point (1,0)

$$\begin{aligned} H_I(1,0) &= -Ti \int_0^1 \frac{(a_2 + b_2 x')(1 - x')}{(1 - x')^3} dx' + 0j \\ &= -Ti \int_0^1 \frac{a_2 + b_2 x'}{(1 - x')^2} dx' \\ &= -Ti \left[ \frac{a_2 + b_2}{(1 - x')} + b_2 \ln(1 - x') \right]_0^1 \\ &= -Ti \left[ -(a_2 + b_2) + \lim_{x' \rightarrow 1} \left( \frac{a_2 + b_2}{(1 - x')} + b_2 \ln(1 - x') \right) \right] \end{aligned} \quad (4.81)$$

Divergence occurs as  $x$  tends to 1.

### 4.3.5 The Shift Method

The method developed to overcome this problem was termed the shift method. If  $P$  was found to lie on one of the vertices of a triangle  $Q$  to be included in the magnetostatic calculation the vertex of  $Q$  was shifted a fraction so that it no longer lay on  $P$ .

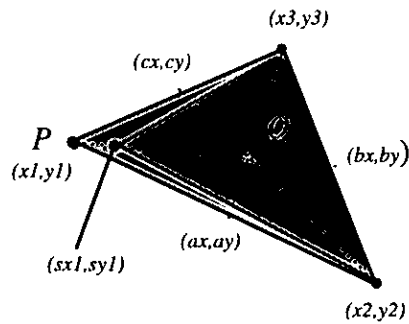


Figure (4.10): Illustrating the shift method

Figure (4.10) illustrates the case when  $P$  coincides with  $Q(x_1, y_1)$ . In order to find the co-ordinates of the position of the new vertex,  $Q(sx_1, sy_1)$ , a line was taken from the old vertex to the midpoint of the opposite side,  $(bx, by)$ . The vertex was then shifted along this line by a fraction, regarded as the shift fraction, leaving  $P$  to lie by itself. The integrals may now be calculated for this shifted triangle as  $P$  does not coincide with any of the co-ordinates of  $Q$ . The same technique was used if  $P$  lay on one of the other two vertices.

The magnetostatic calculation may not be exact using the shift method but it is more accurate than leaving the problem triangles out of the calculation. The triangles that caused the problem were the ones immediately surrounding  $P$  and in most cases there were around five or six. The next decision was how far to shift the vertex along in order to make the calculation as accurate as possible. If the vertex was shifted by too small a

fraction the problems would still remain as there would be divisions by very small, almost zero values. If the vertex was shifted too much then there would be a loss in accuracy. The investigation into the shift fraction can be seen in Chapter 5.

## **4.4 Summary**

The magnetostatic field calculation has been described in detail. The approximate dipole calculation has been discussed and was initially applied to calculate the total magnetostatic field contribution. The exact magnetostatic calculation based on surface and volume integrals was described next. It was used to calculate the close range magnetostatic field effects. The integrals were however, found to have singularities. As a result, The Shift Method was introduced to overcome the problem found. The results from applying the methods of calculating the magnetostatic field can be seen in Chapter 5.

## 5. Results

### 5.1 Introduction

The aim of this project was to study the behaviour of thin magnetic media under the influence of an externally applied field. More specifically, it was to understand the micromagnetic processes within the actual grains that make up the media. In order to do this a micromagnetic model has been developed simulating such behaviour, as described in Chapter 3. The main topic of research has been the calculation of the magnetostatic field and as a result Chapter 4 has been dedicated to it.

This chapter is concerned with the results obtained to illustrate the behaviour of the simulated model in the form of hysteresis loops and 'arrow plots'. An arrow plot was the term given to a vector plot that illustrated the average magnetisation within each grain at specific points along the hysteresis loop. The hysteresis loops will illustrate the effects on the coercivity and the remanence when different parameters were introduced into the model.

Initial studies were on a system of 15 grains in order to test the model. The main study was on a larger system of 40 grains. The results from both systems can be compared in terms of grain size. The system of 15 grains had a larger grain size than the system of 40 grains. The effect of grain size on coercivity has been discussed by Kojima *et al.* (1995) and Sato *et al.* (1996) and will be compared in this chapter briefly. When discussing the system of particles, the results refer to the final system of 40 grains unless otherwise stated.

The model initially introduced the effects of uniaxial anisotropy within the system. This has been discussed in Chapter 3.4.1 where it was shown that the system did follow the Stoner-Wohlfarth theory of rotation (1991) when all the moments were aligned in specific directions. The hysteresis loop obtained from this study can be seen in Chapter

3.4.1, Figure (3.10). An easy axis was associated with each of the grains with a random distribution. The effects of different sets of random easy axes were also noted.

The next effect introduced into the model was the approximate magnetostatic interaction based on dipoles as described in Chapter 4.2. This model was described as the basic model. The effects on the coercivity and the remanence were observed when comparing different strengths of this interaction ( $h_{int}$ ). The exchange effect was then added and the effect of its strength on the coercivity and remanence was also noted.

A more accurate magnetostatic calculation was then introduced which calculated the magnetostatic effects within the closest range, leaving the approximate dipole calculation for triangles further away. This model was described as the enhanced model. Comparisons between the two different methods of calculating the magnetostatic interaction are discussed and provide the results of one of the main aims of this study.

The following sections discuss each of the above points together with the results obtained.

## 5.2 A Comparison Between The Systems Studied

Two systems of grains have been studied and their configurations can be seen in Chapter 3.2.2, Figures (3.3) and (3.4). The average diameter for each system was calculated, taking the diameter of a grain as the maximum distance within the grain. For the system of 15 grains the average diameter was 0.3760 units with a range of [0.2583, 0.4799] and the larger system of 40 grains had an average diameter of 0.2205 units with a range of [0.1828, 0.2614]. The average grain size for the smaller system was almost twice the average grain size of the larger system. The current real grain sizes have been quoted by Grundy (1998) who states that they lie in the range of 10-50 nm.

Each of the systems was tested to check if it followed the Stoner Wohlfarth method of reversal with aligned easy axes. Table (5.1) shows the remanence values obtained from each system with varying values of  $\vartheta$ , where  $\vartheta$  represents the angle between the

applied field and the easy axes. The expected value of the remanence under these conditions was  $\cos \vartheta$ . The figures obtained from both systems compare well against the expected values.

The easy axes were then assigned in random directions where  $0 \leq \vartheta \leq 2\pi$ . Figure (5.1) shows the hysteresis loops from both systems and Table (5.2) shows the respective remanence and coercivity values together with the values obtained by Stoner and Wohlfarth. The two systems again compare well against the Stoner and Wohlfarth predicted values (1991). However, the remanence value from the system of 15 grains was less accurate. This could be due to the fact that it was a particularly small, unrealistic system.

$\vartheta$	<i>15 grains</i>	<i>40 grains</i>	<i>cos</i> $\vartheta$
10°	0.9849796	0.9849790	0.9848077
45°	0.7078074	0.7078097	0.7071067
80°	0.1746161	0.1746204	0.1736481

**Table (5.1): Table of remanence values for different values of  $\vartheta$ , comparing the two systems against the expected values.**

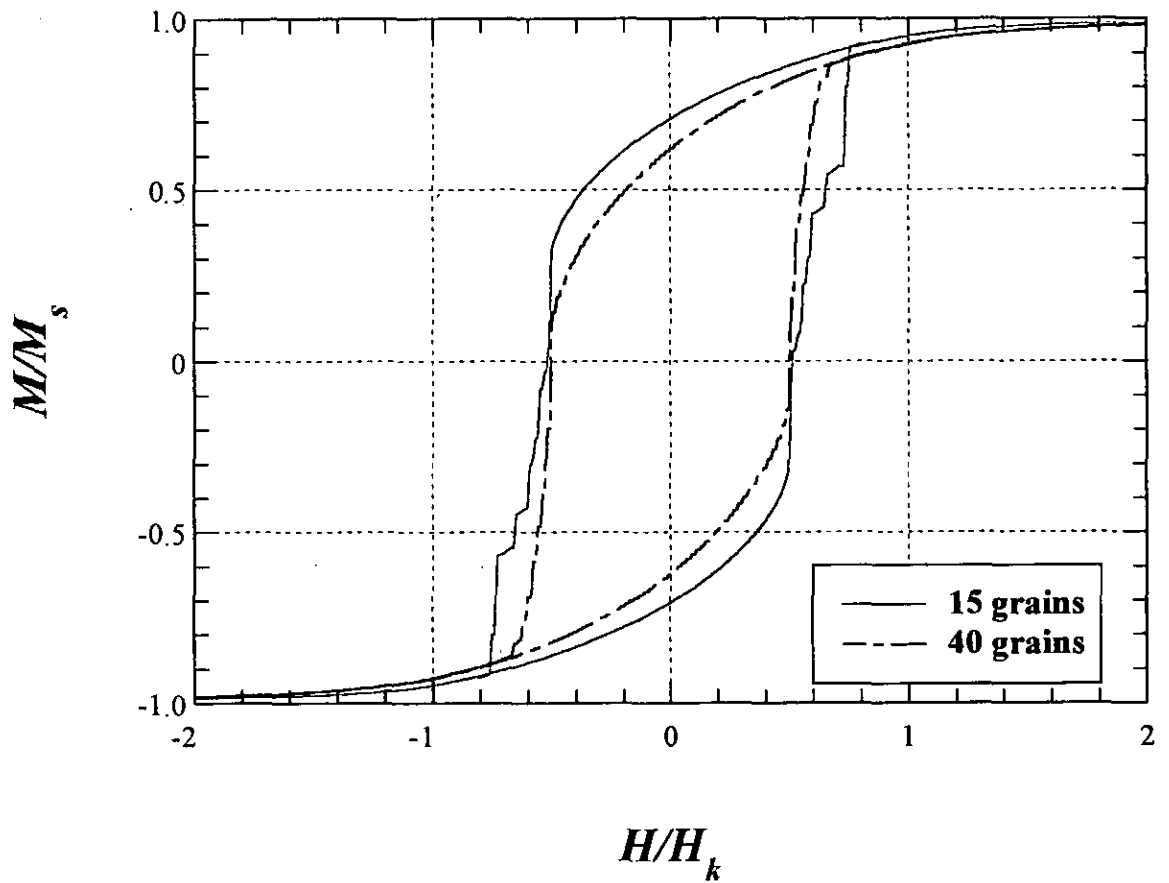


Figure (5.1): Hysteresis loops from a system of 15 and 40 grains with random easy axes

<i>System</i>	<i>Remanence</i>	<i>Coercivity</i>
15 grains	0.706401	0.5024175
40 grains	0.622709	0.504202
Stoner Wohlfarth	0.636620	0.479

Table (5.2): Table of remanence and coercivity values for two systems with random easy axes, comparing against the values obtained by Stoner and Wohlfarth

Several different sets of random easy axes were generated and applied to the model to see if there was any difference between them. The results from both systems can be seen in Figures (5.2) and (5.3). The hysteresis loops show no significant difference between the different sets of random easy axes. This is ideal as differences in remanence and coercivity values can be assumed to be dependent on the magnetostatic and exchange parameters and independent of which set of random easy axes was used.

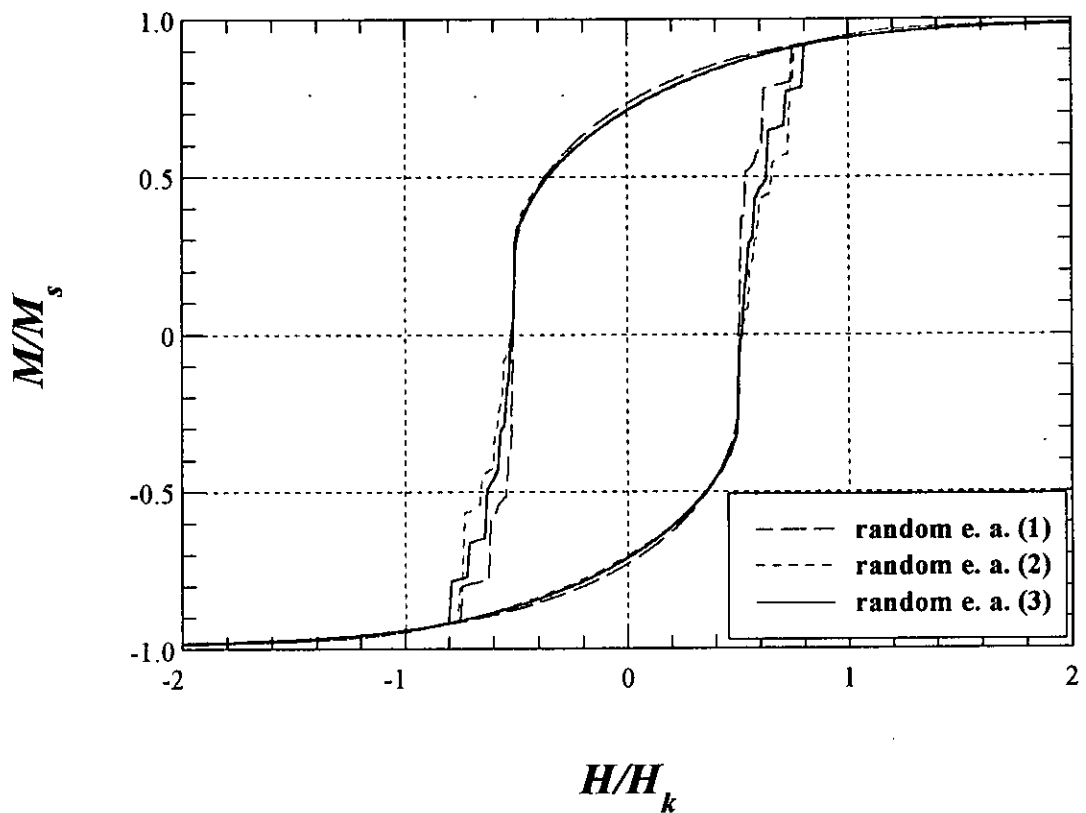
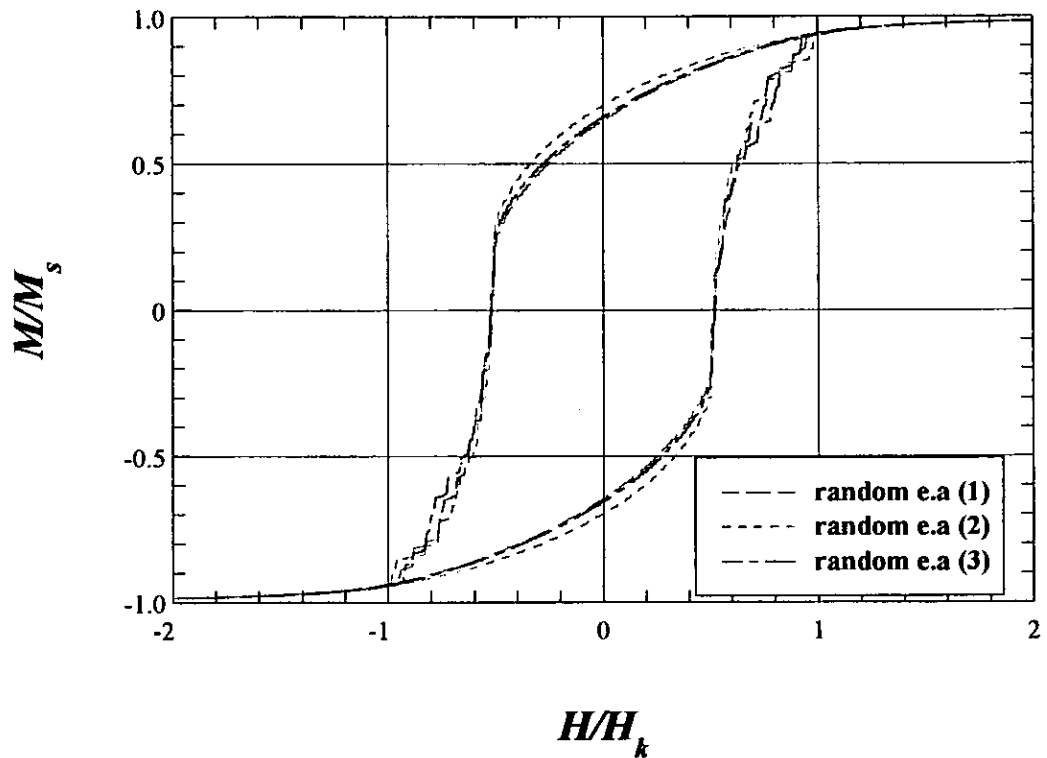


Figure (5.2): Hysteresis loops from the system of 15 grains with 3 sets of random easy axes



**Figure (5.3): Hysteresis loops from the system of 40 grains with 3 sets of random easy axes**

### **5.3 Introducing The Dipole Approximation Into The Model - The Basic Model**

The next interaction incorporated into the model was the approximate magnetostatic field interaction, discussed in Chapter 4. This approximation was based on the elementary unit of magnetism, the dipole. The magnetic medium was assumed to consist of a system of grains which were subsequently divided into triangles. A dipole moment was assigned to each vertex of the triangles and to the seed points of the original grains. The magnetostatic field calculated at each dipole should consider all the other dipoles in the system. In this approximation each triangle was assigned an average dipole moment located at its centroid, whose magnitude was its volume and its direction was the average direction of the three dipoles at its vertices. Each original moment was taken in turn and the effect of the magnetostatic field due to the triangles in the system was calculated. Not all the triangles were included, only the triangles whose centroids lay within a prescribed radius,  $r_2$ , contributed to the magnetostatic field.

The first step for this part of the study was to decide what value  $r_2$  should take. Since the model incorporated periodic boundary conditions the minimum image convention was employed (Heermann, 1990). This states that in a periodic boundary simulation, the particle should only 'see' one copy of any other particle within the system. To ensure this the cut-off point, in this case  $r_2$ , should be  $L/2$ , where  $L$  is the side of the basic cell.

The parameter associated with the dipole approximation is known as  $h_{int}$  and its possible range of values needs to be investigated. It has been defined in Chapter 4 in reduced units as

$$h_{int} = \frac{TM_s^2}{2KL}$$

Lu *et al.* (1992) assigned a parameter similar to  $h_{int}$ , the only difference being that in their model the constant  $L$  represented the length of the side of the hexagonal grain. In their model  $T$  and  $L$  were chosen to be equal. The range of  $h_{int}$  values studied in their model was [0.05,0.3]. Zhu and Bertram (1988) stated that a relative measure of the magnetostatic interaction could be represented as  $h_m = M_s/H_k$  and studied values in the range of [0.3,0.6].

The value representing the strength of the magnetostatic interaction is dependent on the microstructure being modeled (Kay, thesis) as it incorporates values such as the diameter or volumes of hexagonal grains (Dean, thesis) or spherical grains (Kay, thesis; Hannay *et al.*, 1999). The values used in previous models take average values of individual grains, however, the parameter in this model incorporates the length scale which represents the side of the basic cell. An immediate comparison cannot therefore be made. The magnetostatic interaction strength also depends on the values taken to represent  $M_s$  and  $K$ . The values used to obtain an estimate value for  $h_{int}$  are those as stated in Mee and Daniels (1987) and used by Tako (thesis) and Hannay *et al.* (1999). The value for  $M_s = 1.4 \times 10^3$  emu/cm<sup>3</sup> and  $K = 4.2 \times 10^6$  erg/cm<sup>3</sup>.

An estimate value for the thickness of the film needs to be sought. Experimental studies in 1994 by Choe *et al.* produced thin films having a thickness of 50 nm. Later work by Imakawa *et al.* in 1998 produced films, using an U-C process, with a thickness of 40

nm. Recently, work done by Futamoto *et al.* (1999) produced DC sputter deposited film with a thickness of 25 nm. An estimated value of the thickness of the thin film was taken as 30 nm ( $3 \times 10^{-6}$  cm).

Finally, a value for the length scale,  $L$ , needs to be estimated. Since this value represents the length of one side of the basic cell it can be expressed in terms of grains. The system of 40 grains is approximately a system of 6 x 6 grains and therefore  $L$  can be represented as 6 x the average grain size of the system. An estimate value for the grain size was given by Grundy (1998) who states that currently they lie in the range of 10-50 nm. Experimentally, Imakawa *et al.* (1998) and Takahashi *et al.* (1999) have recently produced films with average grain sizes of 10 nm. A value of 30 nm was taken to represent the average size of the grains.  $L$  can be estimated as  $6 \times (3 \times 10^{-6})$  cm. The estimated average grain size has the same value as the estimated thickness of film, as used by Lu *et al.* (1992).

Substituting all the estimated values into the equation for the magnetostatic interaction parameter,  $h_{int} = M_s^2 / 12K = 0.039$ . The values used in this study lay either side of the estimated value and ranged from 0.01 to 0.06. The results for increasing  $h_{int}$  can be seen in Figures (5.4), (5.5) and (5.6). The effect on the remanence value is not clear from the hysteresis loops but can be seen clearly in Figure (5.5). This shows a slight increase when a weak magnetostatic field is introduced but remains steady throughout as  $h_{int}$  is increased. This pattern has also been observed by Zhu and Bertram (1988). The effect on the coercivity can be seen in Figure (5.6) as well as from the hysteresis loops. There is an initial decrease in the coercivity as a weak magnetostatic interaction is introduced. It then increases steadily as the magnetostatic interaction strength becomes stronger. Zhu and Bertram (1988) however found that the coercivity decreases as the magnetostatic strength became greater.

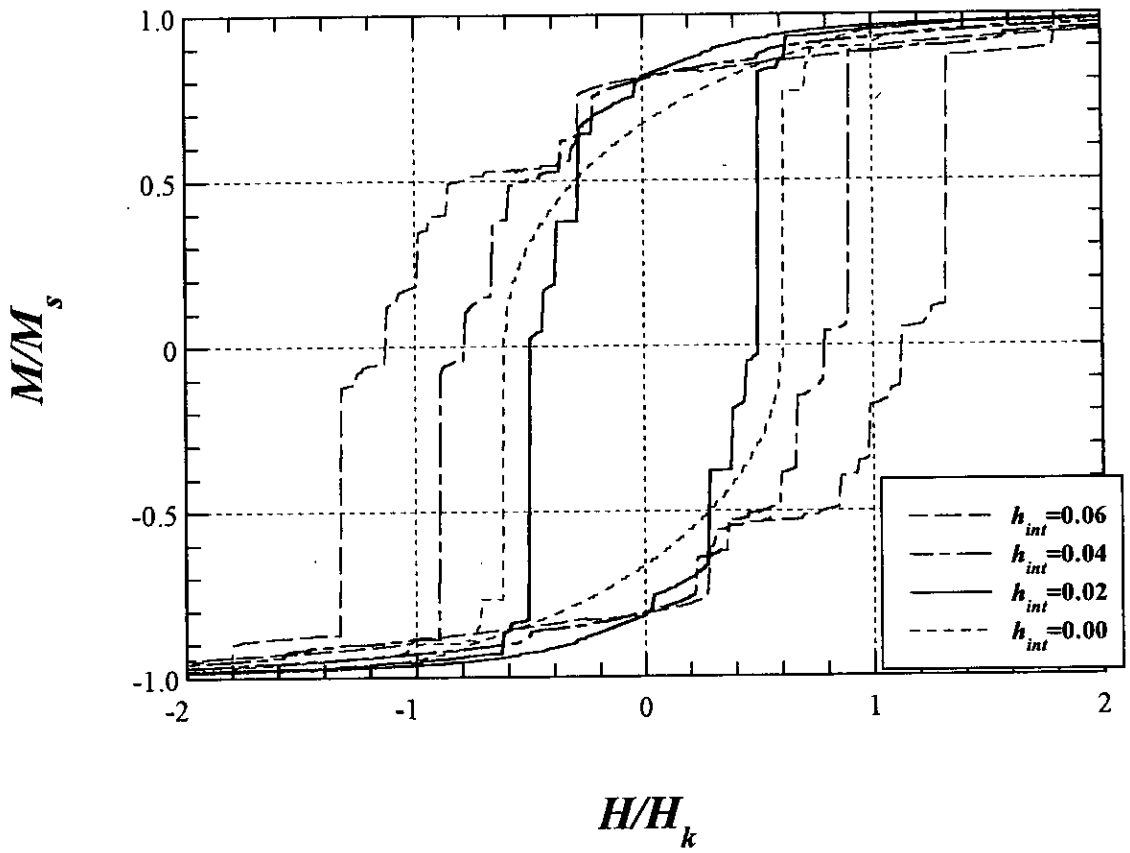


Figure (5.4): Hysteresis loops to show the effect of increasing  $h_{int}$

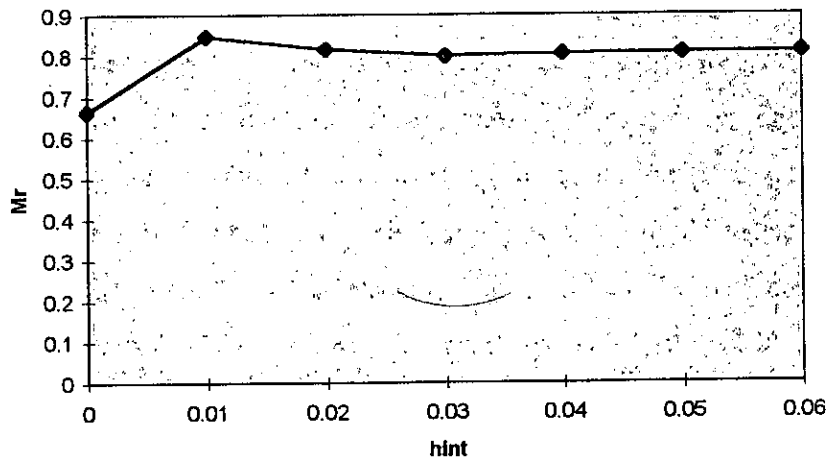
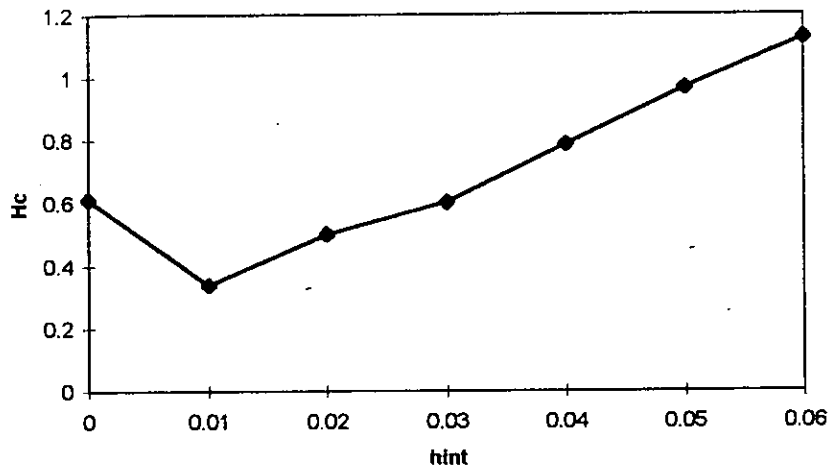
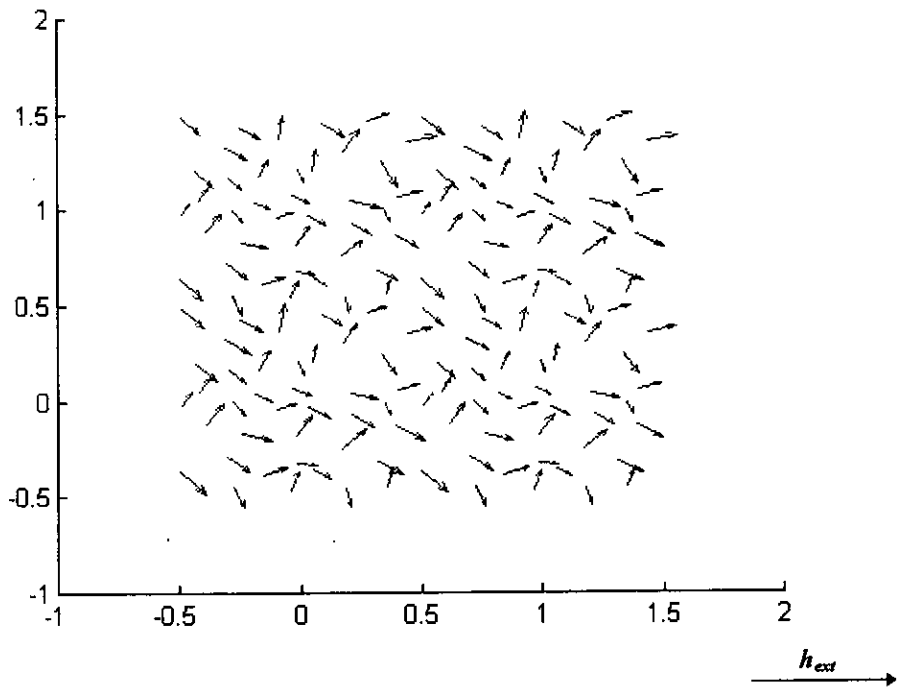


Figure (5.5): Graph to show remanence values ( $M_r$ ) against increasing values of  $h_{int}$



**Figure (5.6):** Graph to show coercivity values ( $H_c$ ) against increasing values of  $h_{int}$

The behaviour of the moments at remanence and coercivity can be seen from the arrow plots for different strengths of  $h_{int}$ . The first arrow plot, Figure (5.7), is the case where  $h_{int}$  is set to zero and shows the moments after the external field has been removed, i.e. at remanence. The moments appear to have been affected by the applied field but are also influenced by their own easy axes. The overall direction appears to be in the direction of the applied field but there is also the added random factor associated with each moment due to the random distribution of the easy axes. At coercivity, Figure (5.8), the moments appear to be in random directions giving an overall magnetisation of zero. When a weak magnetostatic field is introduced ( $h_{int}=0.01$ ) a ripple structure is formed at remanence, see Figure (5.9). At coercivity, Figure (5.10), the moments have formed 'weak' vortices. When a stronger magnetostatic field is introduced ( $h_{int}=0.03$ ) a more pronounced ripple structure can be seen at remanence, Figure (5.11), and at coercivity, Figure (5.12), the moments have formed 'stronger' vortices. These results compare well with the findings of Zhu and Bertram (1991) who stated that 'increasing the magnetostatic interaction constant results in better defined vortex structures and larger vortex sizes.'



**Figure (5.7):** Arrow plot taken at remanence when  $h_{int} = 0.0$

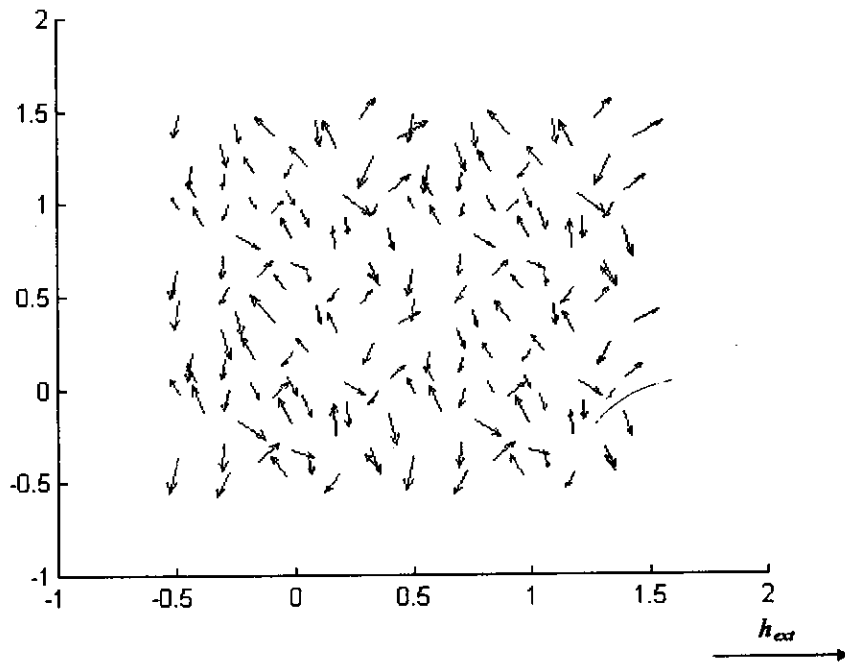


**Figure (5.8):** Arrow plot taken at coercivity when  $h_{int} = 0.0$

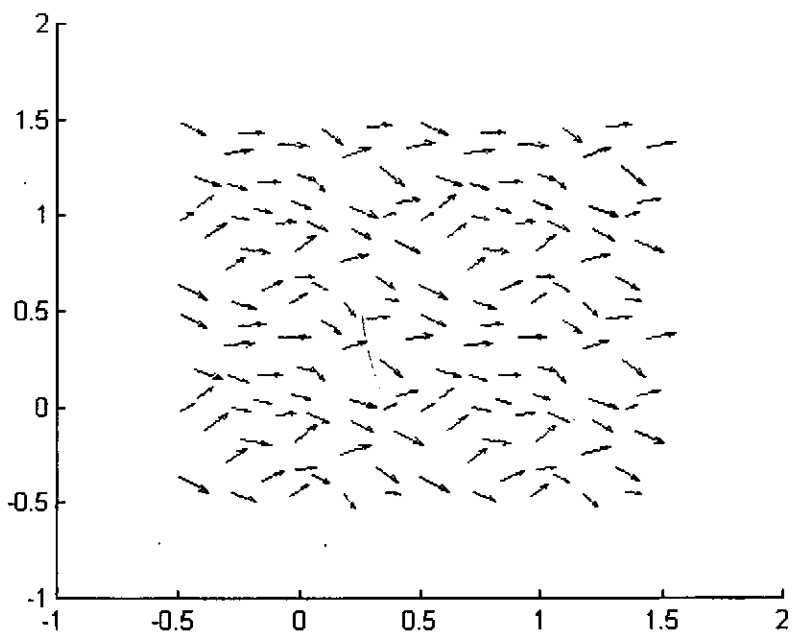


**Figure (5.9):** Arrow plot taken at remanence when  $h_{ir}=0.01$

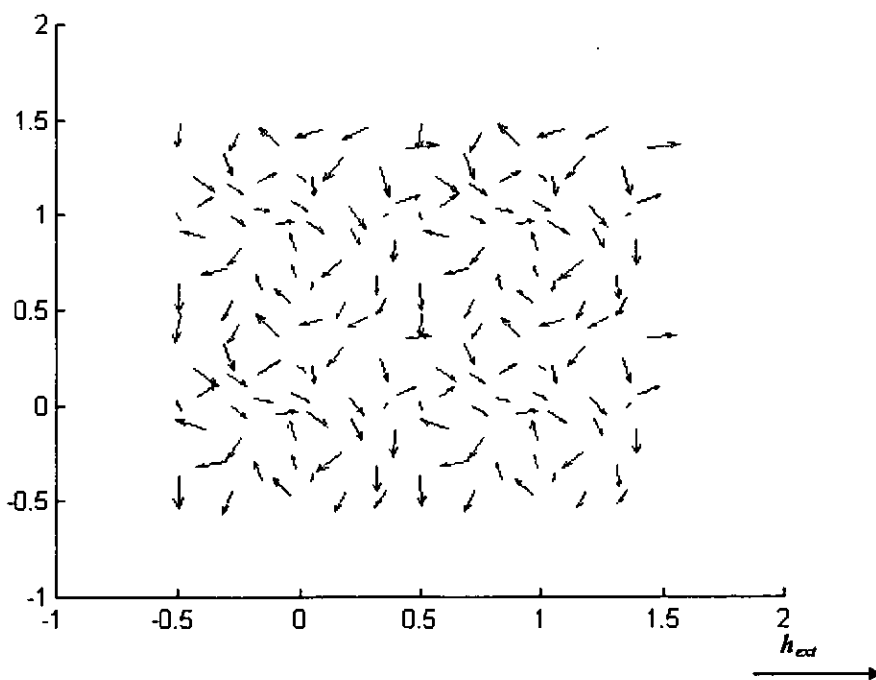


**Figure (5.10):** Arrow plot taken at coercivity when  $h_{ir}=0.01$

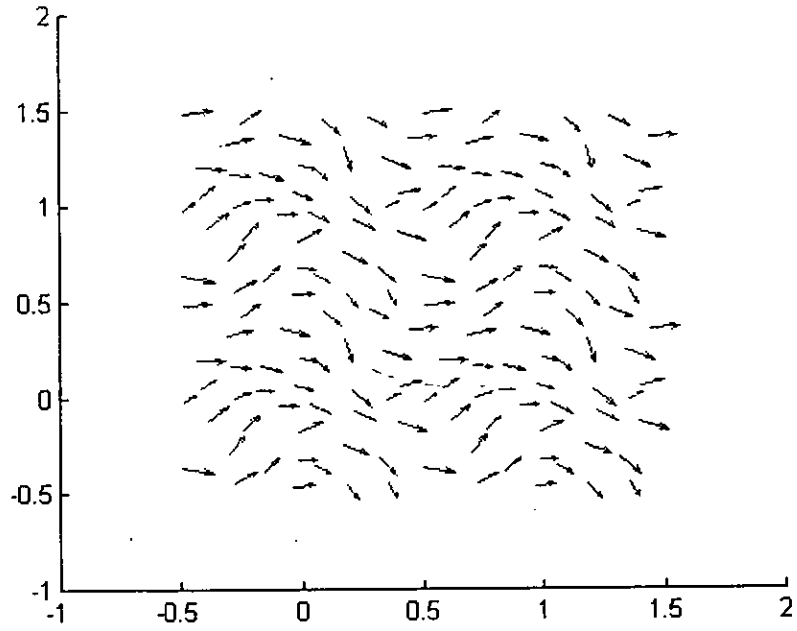


**Figure (5.11):** Arrow plot taken at remanence when  $h_{int}=0.03$

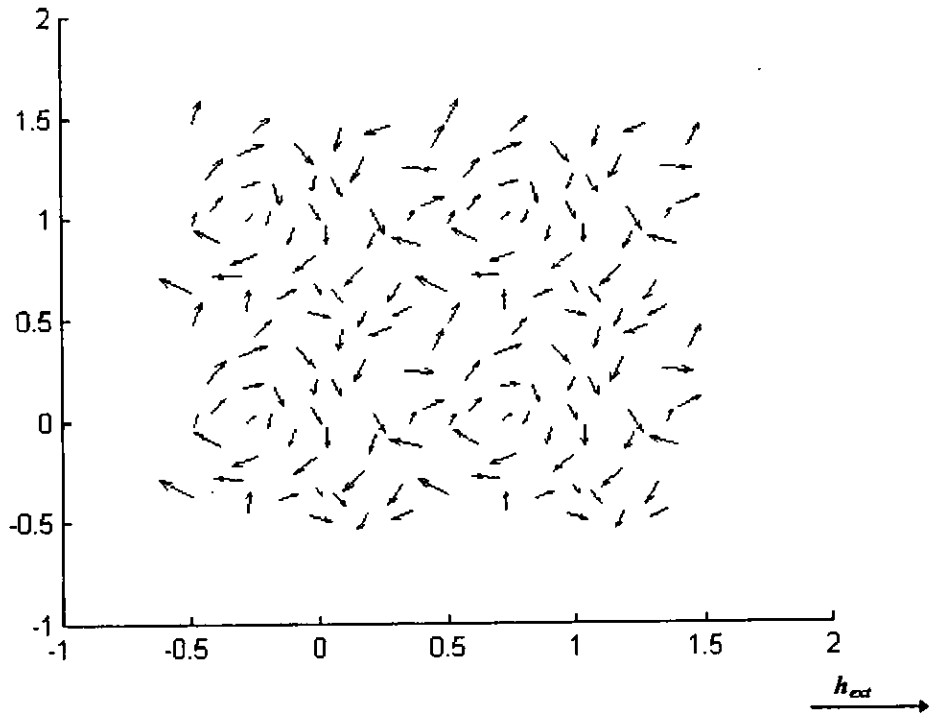


**Figure (5.12):** Arrow plot taken at coercivity when  $h_{int}=0.03$

Earlier studies on the smaller system of 15 grains showed the same overall pattern in terms of remanence and coercivity values against increasing  $h_{int}$ .

A value for  $h_{int}$  needed to be set in order to study the effects of the exchange interaction parameters. A value of 0.03 was set while the next interaction was studied.

## 5.4 Introducing The Exchange Effect Into The Model

The exchange interaction was then introduced into the basic model. This has been discussed in detail in Chapter 3. There are two parameters that need to be investigated within this calculation. The first one,  $C_1^*$ , describes the strength of the exchange coupling within the grains and the second,  $C_2^*$ , describes the strength of the exchange coupling across the grain boundaries. The second one is more commonly recognized as simply  $C^*$ . As already defined earlier in Chapter 3 they can be written as

$$C_1^* = \frac{A}{KL^2} \quad \text{and} \quad C_2^* = \frac{J^* M_s^2}{K}$$

where  $A$  is the exchange constant and  $J^*$  is the exchange integral. The second parameter is considered first, as most micromagnetic models in this field use a similar parameter. Zhu and Bertram (1991) stated that a value of 0.1 was practical for a Co-based alloy film. Hannay *et al.* (1999) studied a range between [0, 0.4] for  $C^*$  and stated that only grains within a radius of approximately 0.06 mean grain diameters was used in the calculation. Lu *et al.* (1992) studied values between [0.1,0.2] in their model of thin films. Tako (thesis), who also incorporated the same exchange calculation, studied values in the range [0,0.4].

It was difficult to obtain a value of  $J^*$  in order to substitute it into the equation of  $C_2^*$ . The values studied were therefore based on previous models and lay between [0,1].

Since  $C_2^*$  describes the strength of the exchange coupling across the grain boundaries, experimentally it can be varied by the amount of non-magnetic Cr content within the grain boundaries. The exchange coupling has been found to decrease with increasing Cr

content within the grain boundaries (Futamoto *et al.*, 1999). Noise properties and coercivity values have been associated with the exchange coupling strength. It has been found that reducing the exchange coupling between the grains reduces the noise and increases the coercivity of the material (Futamoto *et al.*, 1999; Imakawa *et al.*, 1998). Therefore, for an optimum recording material the grains should be well exchange-decoupled (Futamoto *et al.*, 1999).

The other parameter,  $C_1^*$ , is not as widely recognised and it was difficult to find other models that incorporated this parameter into the exchange calculation. Tako (thesis) used the same exchange equation in his model and chose a value of 0.2 for this parameter.

The experimental values were substituted into the equation for  $C_1^*$  as used in the equation for  $h_{int}$ . A value for the exchange constant,  $A$ , was taken as  $10^{-6}$  erg/cm (Tako, thesis; Vecchio *et al.*, 1989) and a value of 0.0007 was obtained. It clearly is dependent on the value taken to represent the size of the grains, the smaller the size of the grains the larger the parameter and vice-versa. It was for this reason that Schabes (1991) introduced a scaling relation between particle size and exchange constant into his model. A range between [0, 0.05] was studied for this parameter.

The effect of  $C_1^*$  was studied first whilst setting  $C_2^*$  to zero, i.e. the exchange within the grain was observed assuming that no exchange coupling was present across the grain boundaries. Figure (5.13) shows the effect on the remanence when increasing  $C_1^*$ . The graph suggests that there appears to be no significant differences in the remanence values as  $C_1^*$  is increased. Figure (5.14) shows the effect on the coercivity values as  $C_1^*$  is increased. There was an initial decrease in the coercivity value as  $C_1^*$  was introduced up until a value of 0.02, after this the coercivity remained steady.

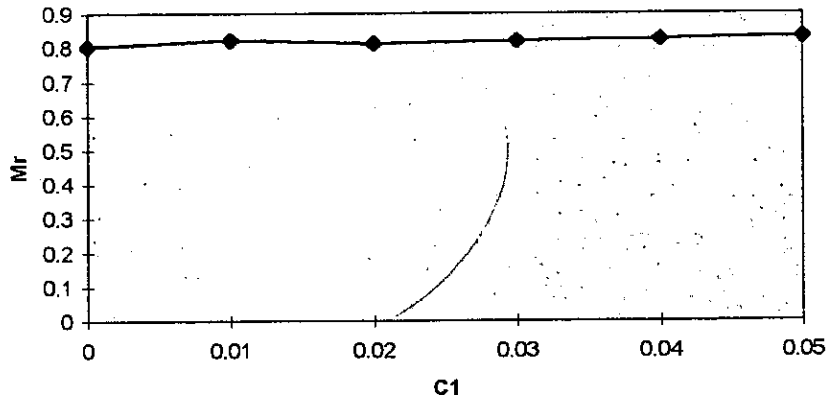


Figure (5.13): Graph to show the effects on the remanence as  $C_1^*$  is increased

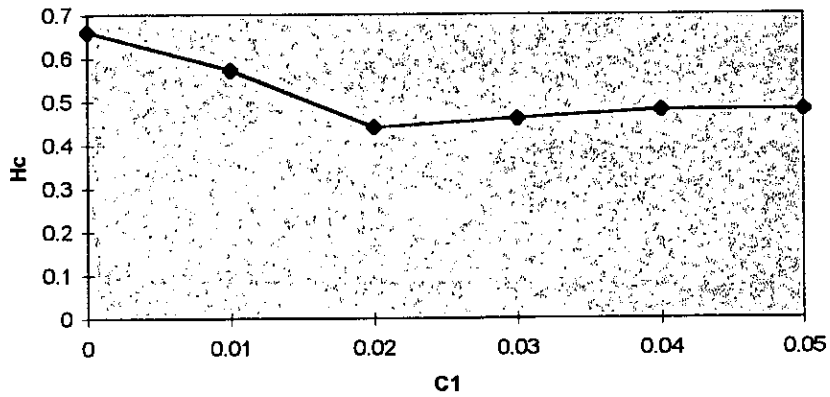


Figure (5.14): Graph to show the effects on the coercivity as  $C_1^*$  is increased

In order for the second parameter to be studied a value of 0.02 was set for  $C_1^*$ . Figure (5.15) shows the effect on the remanence as  $C_2^*$  was increased. The remanence value appears to show a slight increase with increasing  $C_2^*$ . Figure (5.16) shows the effect on the coercivity as  $C_2^*$  was increased. The graph shows an overall increase in the coercivity up to  $C_2^* = 0.5$ . The coercivity value then decreases and remains at a steady value.

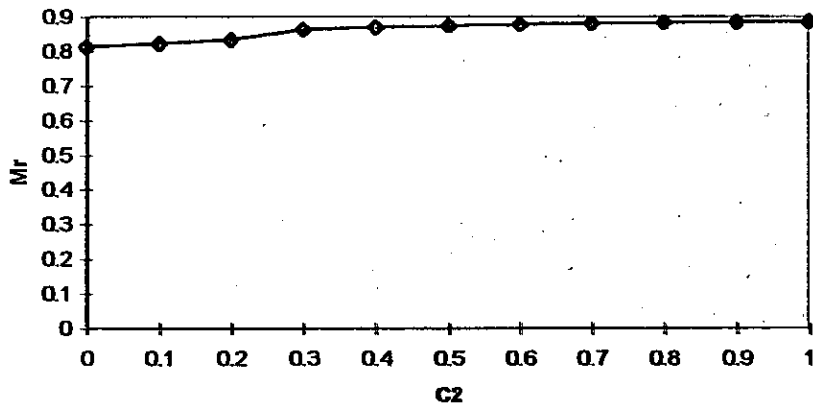


Figure (5.15): Graph to show the effect on the remanence as  $C_2^*$  is increased

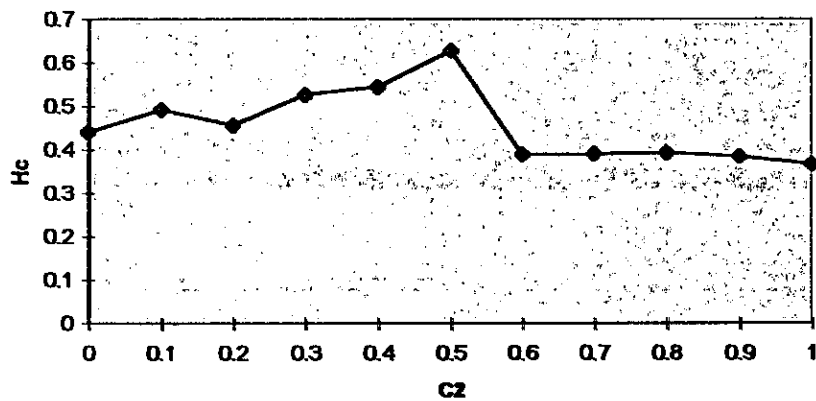


Figure (5.16): Graph to show the effect on the coercivity as  $C_2^*$  is increased

This did not agree with the results found experimentally. As discussed earlier, when the strength of the exchange coupling is increased, the coercivity was found to decrease.

Figures (5.17) and (5.18) show the arrow plots of the model, where  $C_1^* = 0.02$  and  $C_2^* = 0.4$ , taken at remanence and coercivity. The remanence shows a similar pattern seen when only the magnetostatic effect was included in the model. At coercivity, vortices can be seen illustrating the magnetostatic effect still present in the model. The vortices are not as strong as the model with only magnetostatic present. This could be due to the competing exchange effect trying to align the moments.

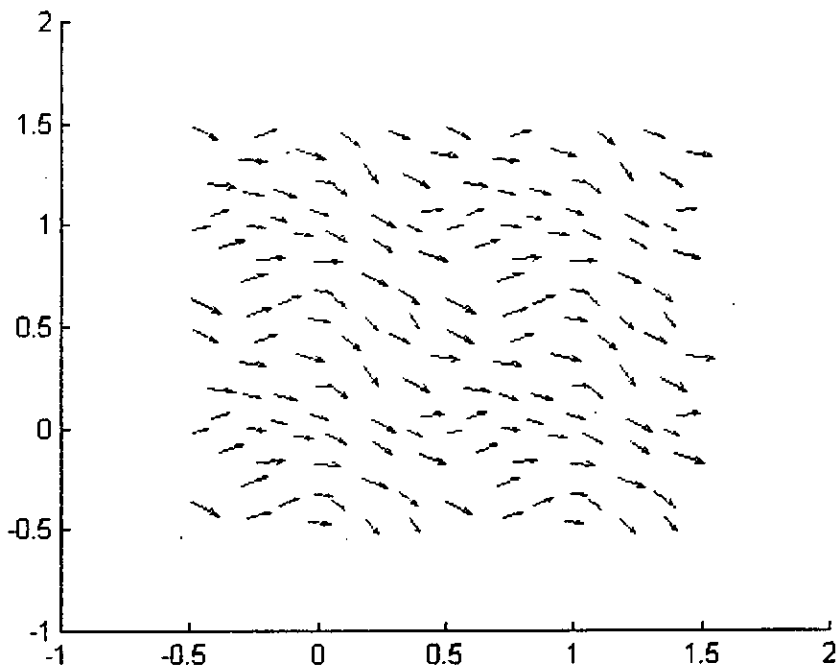


Figure (5.17): Arrow plot taken at remanence when  $h_{int}=0.03$ ,  $C_1^*=0.02$  and  $C_2^*=0.4$

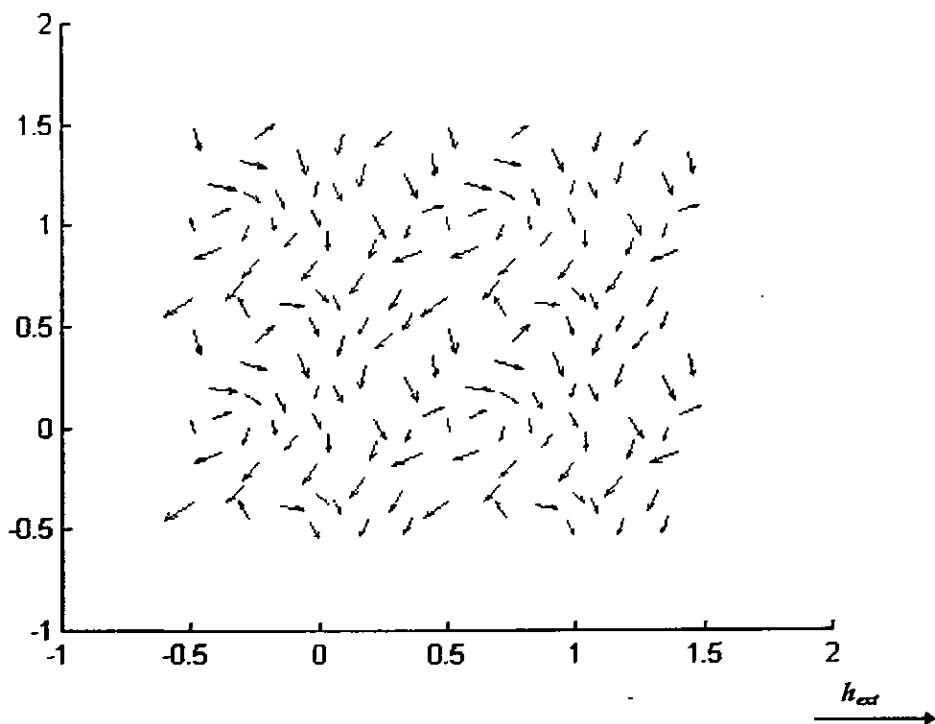
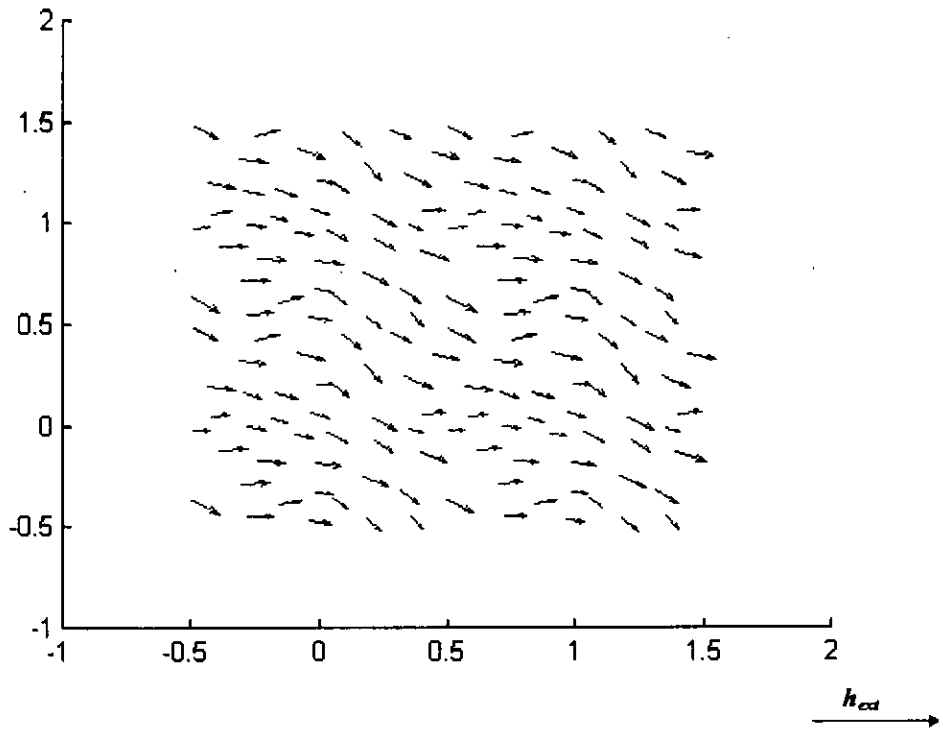


Figure (5.18): Arrow plot taken at coercivity when  $h_{int}=0.03$ ,  $C_1^*=0.02$  and  $C_2^*=0.4$

When a stronger exchange was introduced ( $C_2^* = 1.0$ ) a similar pattern was seen at remanence, see Figure (5.19). At coercivity the exchange effects can clearly be seen, Figure (5.20) and dominate over the magnetostatic effects. The strong effects of the exchange which keep the moments in line with each other can be seen.



**Figure (5.19):** Arrow plot taken at remanence when  $h_{int} = 0.03$ ,  $C_1^* = 0.02$  and  $C_2^* = 1.0$

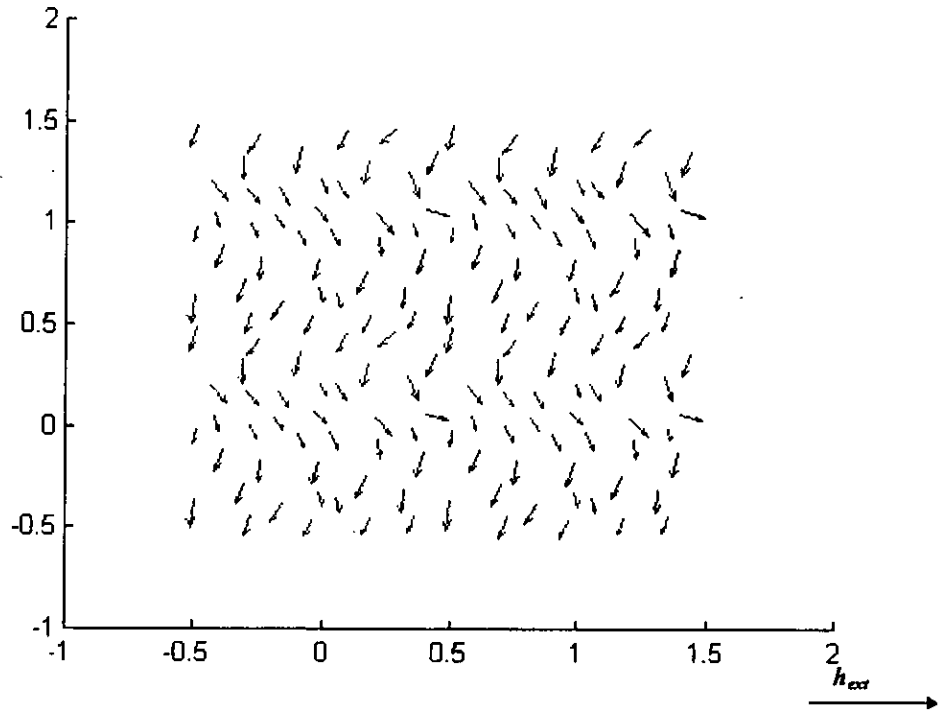
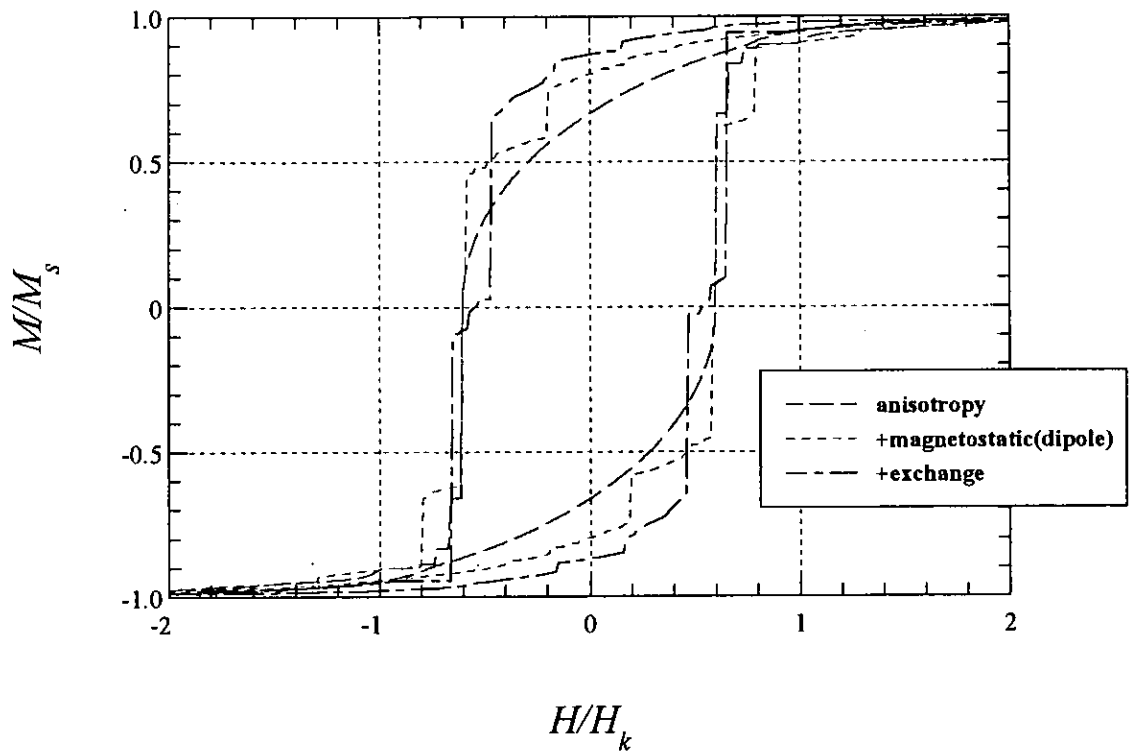


Figure (5.20): Arrow plot taken at coercivity when  $h_{int}=0.03$ ,  $C_1^*=0.02$  and  $C_2^*=1.0$

The basic dipole model has now been discussed. A comparison can be made at this stage involving the effects on the hysteresis loop in terms of the anisotropy, the approximate magnetostatic and the exchange effects. Figure (5.21) illustrates the effects on introducing each interaction into the model. The parameters set were as follows:

anisotropy:	random easy axes
dipole model:	$r_2=0.5$ and included all the triangles within this radius. $h_{int}=0.03$
exchange:	$C_1^*=0.02$ and $C_2^*=0.4$



**Figure (5.21):** Introducing each of the interactions into the basic model

As each of the interactions was introduced into the model, the remanence increased. There appeared to be no difference in the coercivity value as the magnetostatic effect was introduced, but with exchange included in the model the coercivity value decreased.

## 5.5 The Enhanced Model

### 5.5.1 Introducing The Exact Magnetostatic Calculation Into The Model

The exact magnetostatic calculation was next incorporated to enhance the basic model. This method of calculating the magnetostatic field is based on volume and surface

charges. During initial studies the exchange effect was removed from the model so that total concentration lay on the magnetostatic effects. The main aim was to compare the two techniques of calculating the magnetostatic field, the dipole approximation and the exact calculation. The two methods have been discussed in detail in Chapter 4. The two parameters for each calculation,  $h_{int}$  and  $h^*$ , were

$$h_{int} = h^* = \frac{TM_x^2}{2KL}$$

The value set for  $h^*$  needed to be equal to the value set for  $h_{int}$ . For initial studies they were both set to 0.01.

## 5.5.2 The Shift Method

The exact calculation used what was termed the Shift Method for the ‘problem triangles’. This meant that a value for the shift fraction needed to be studied. The values studied were in the range  $[1/3, 1/100]$ . The method was tested by taking a point,  $P$ , and evaluating the exact calculation due to one triangle,  $Q$ . Two studies were conducted, one with  $P$  outside  $Q$  and the other with  $P$  on one of the vertices of  $Q$ . In the first case  $P$  was given the co-ordinates (0,0) and the triangle vertices had the co-ordinates  $[(2,1), (6,3), (3,5)]$ . The surface and line integrals were calculated on the whole triangle as normal and then calculated using the shift method with different values of the shift fraction. The results for the absolute value of the  $x$  component of the surface integral can be seen in Figure (5.22). The results were as expected. As the shift fraction decreased it converged to the actual value of the surface integral.

In the second case,  $P$  was placed on a vertex of  $Q$  with the co-ordinates (2,1). The exact surface integral could not therefore be evaluated in this case. The Shift Method was used in the calculation and the results on varying the shift fraction can be seen in Figure (5.23). The results clearly showed divergence.

A value of 1/5 for the shift fraction was settled on.

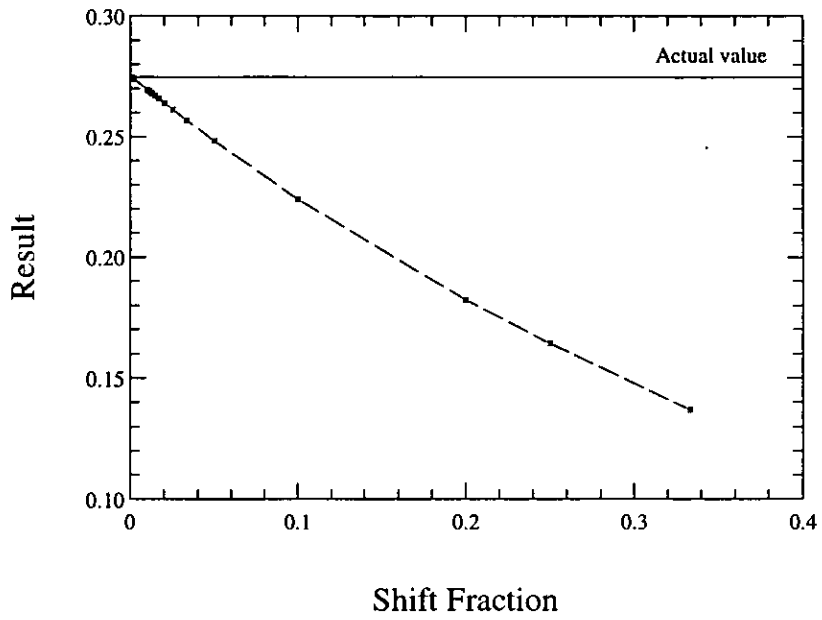


**Figure (5.22): Results from calculating the surface integral with and without the shift method, where  $P$  was placed at a distance from  $Q$ .**

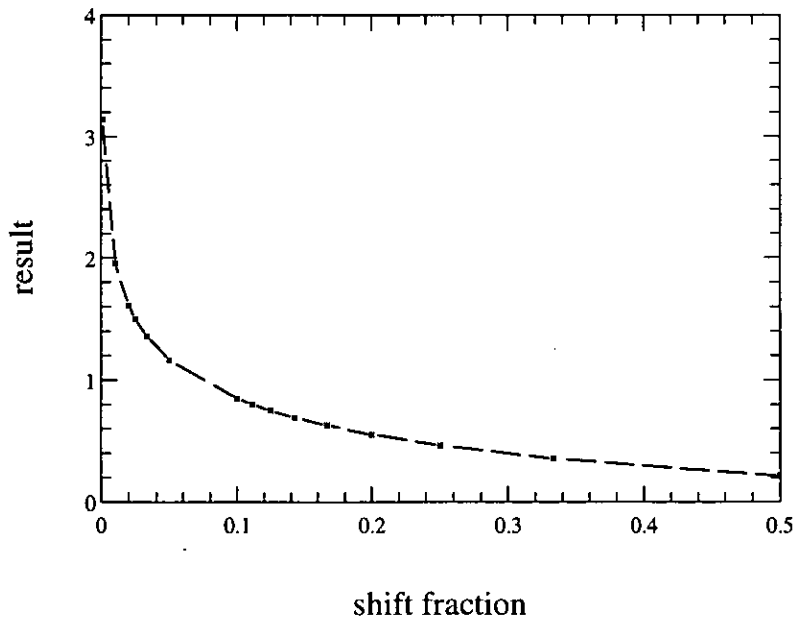


**Figure (5.23): Results from calculating the surface integral using the shift method, where  $P$  was placed on a vertex of  $Q$ .**

### 5.5.3 Investigating r1

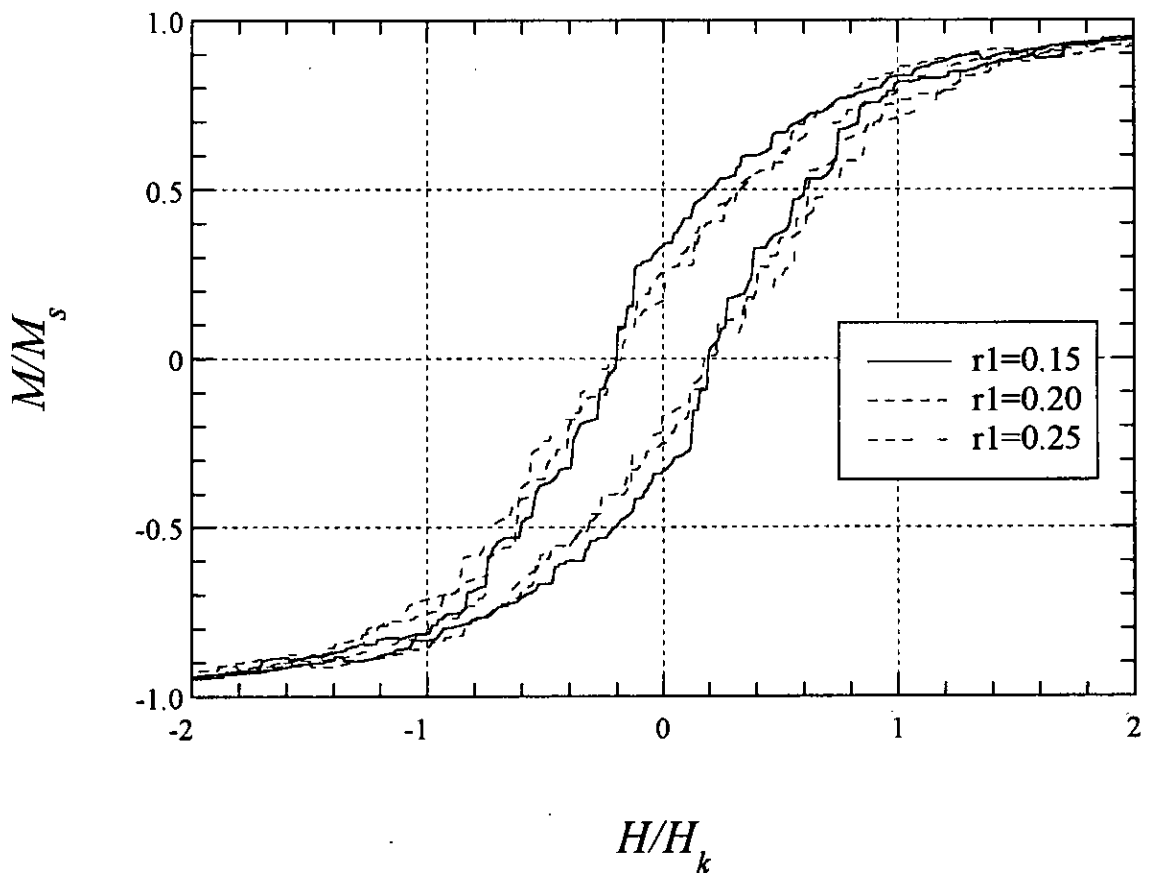
The next stage of incorporating the exact calculation into the model was to set a value for r1. This is the radius containing the triangles considered for the exact calculation. A range of radius values were considered and the average number of triangles within each radius from a point was initially obtained, see Table (5.3).

r1	number of triangles	r2	number of triangles
0.00	0	0.5	182
0.05	1	0.5	180
0.10	7	0.5	174
0.15	16	0.5	165
0.20	30	0.5	152
0.25	46	0.5	136
0.30	66	0.5	115
0.35	90	0.5	92

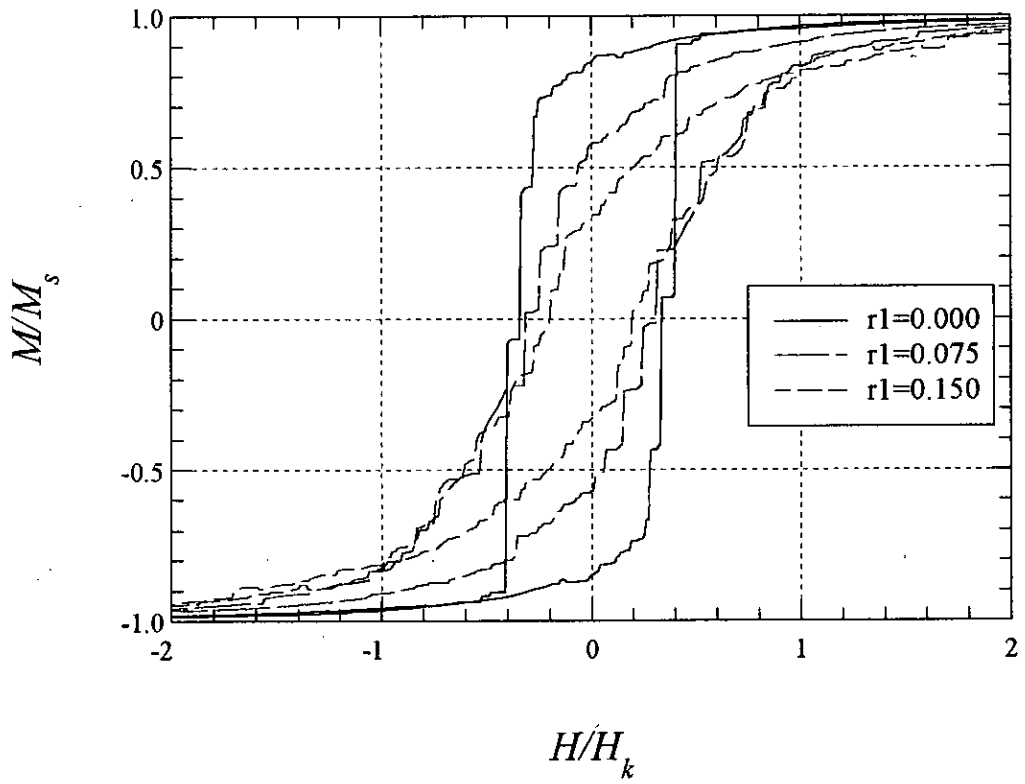
**Table (5.3): Table to show the number of triangles within r1 and r2 with different values of r1 against constant r2.**

Figure (5.24) shows the hysteresis loops obtained when using values of r1 in the range [0.15,0.25]. There clearly is a difference in the remanence values as r1 is increased. The remanence was found to decrease as r1 increased. The coercivity values, however, showed no significant differences as r1 was varied.

As  $r_1$  is decreased down to zero it means that the number of triangles within  $r_2$  increases. In other words the number of triangles included in the exact calculation is decreasing and used for the dipole calculation. Figure (5.25) continues from Figure (5.24) and illustrates the transition from when the dipole calculation was used on all the triangles to when the exact calculation was introduced slowly from  $r_1=0.0$  to  $r_1=0.15$ . The effect on the remanence and coercivity values can be seen in Figures (5.26) and (5.27). In both cases there is an overall decrease as  $r_1$  is increased. For further studies a value of 0.20 was set for  $r_1$ .



**Figure (5.24): Hysteresis loops illustrating the effect on the remanence and coercivity values as  $r_1$  is varied**



**Figure (5.25): Hysteresis loops illustrating the introduction of the exact calculation in the model**

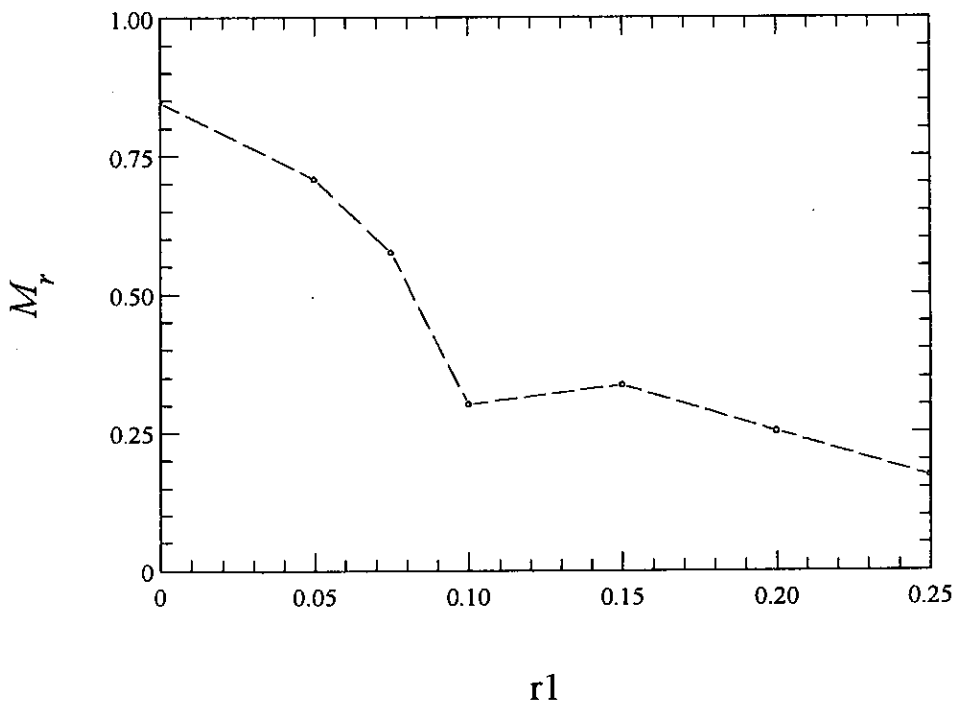


**Figure (5.26): Illustrating the effect on the remanence as  $r_1$  is increased**



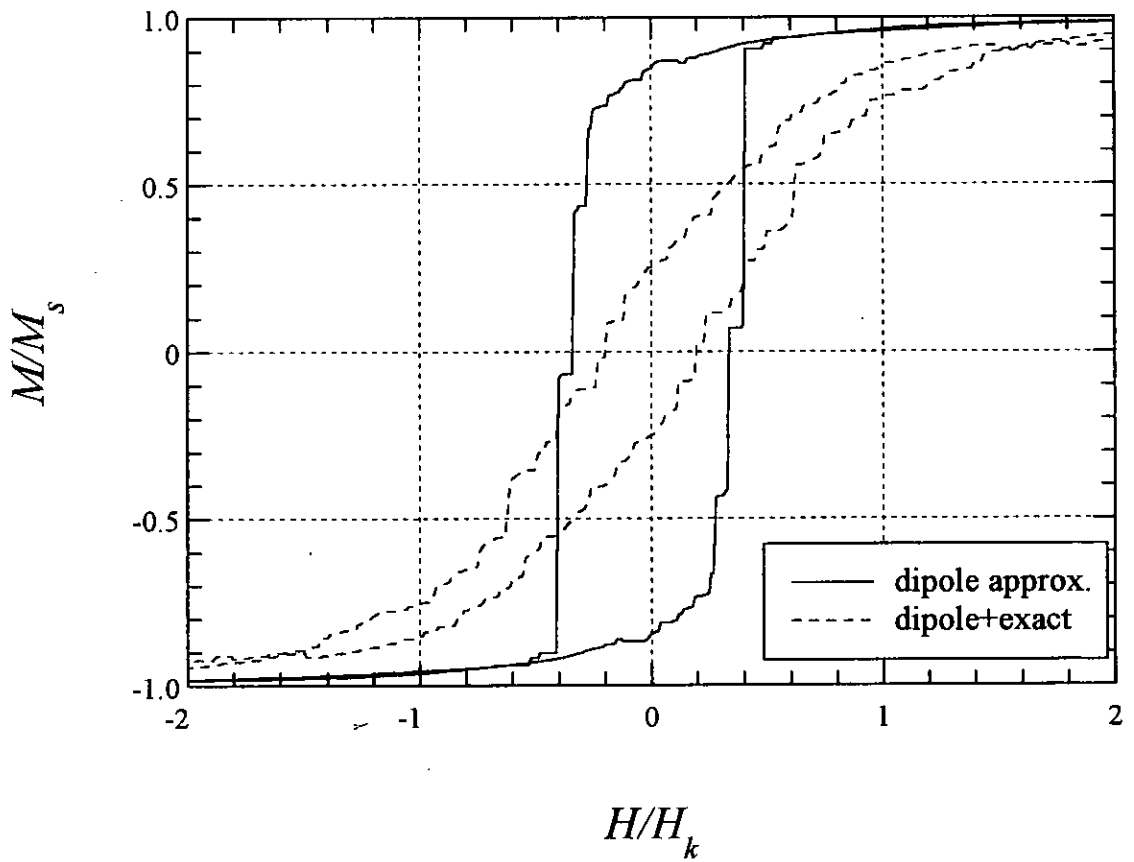


**Figure (5.28): Hysteresis loops illustrating the effects when using the two methods of calculating the magnetostatic field**

The loops show dramatic differences when using the two methods of calculation for the magnetostatic field.

A step further along this line of investigation was to see the differences in the calculation of the magnetostatic field due to the nearest neighbours. This was done by comparing the following models:

```

anisotropy+magnetostatic(dipole(r2=0.2, hint=0.01))
v
anisotropy+magnetostatic(exact(r1=0.2, h*=0.01))

```

The hysteresis loops can be seen in Figure (5.29). There is clearly a significant difference between the two methods of calculating the magnetostatic field of the nearest neighbours.

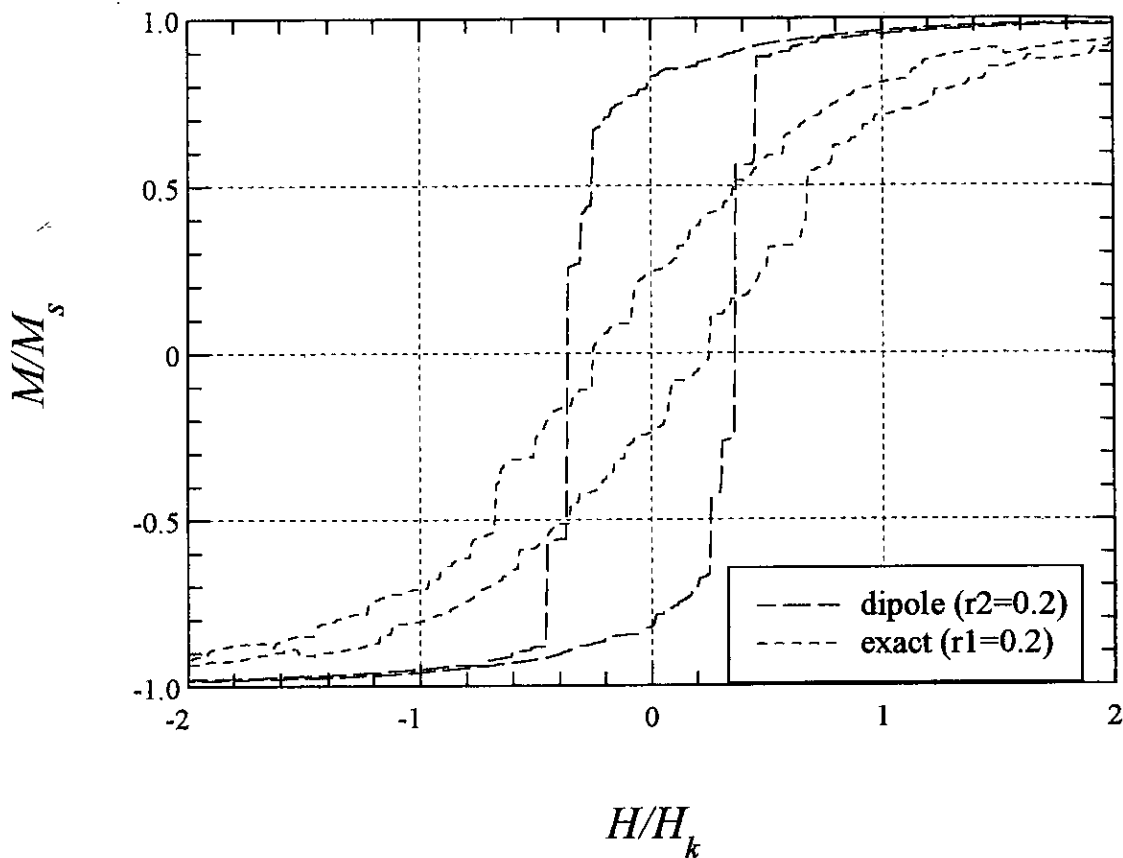


**Figure (5.29): Hysteresis loops illustrating the differences in the calculation of the near neighbours**

It has so far been shown that the inclusion of the exact calculation made a significant difference to the hysteresis properties. The next step was to see if the inclusion of the 'problem triangles' made any difference. Was it necessary to employ the shift method on these triangles or could they just be ignored? To answer this question the following models were compared:

$$\begin{aligned} & \text{anisotropy+magnetostatic}(\text{exact}(r1=0.2)+\text{dipole}(r2=0.5), h^* = h_{int}=0.01) \\ & \quad \quad \quad \vee \\ & \text{anisotropy+magnetostatic}(\text{exact}(r1=0.2-\text{problem triangles})+\text{dipole}(r2=0.5), h^* \\ & \quad \quad \quad = h_{int}=0.01) \end{aligned}$$

The hysteresis from this study can be seen in Figure(5.30).

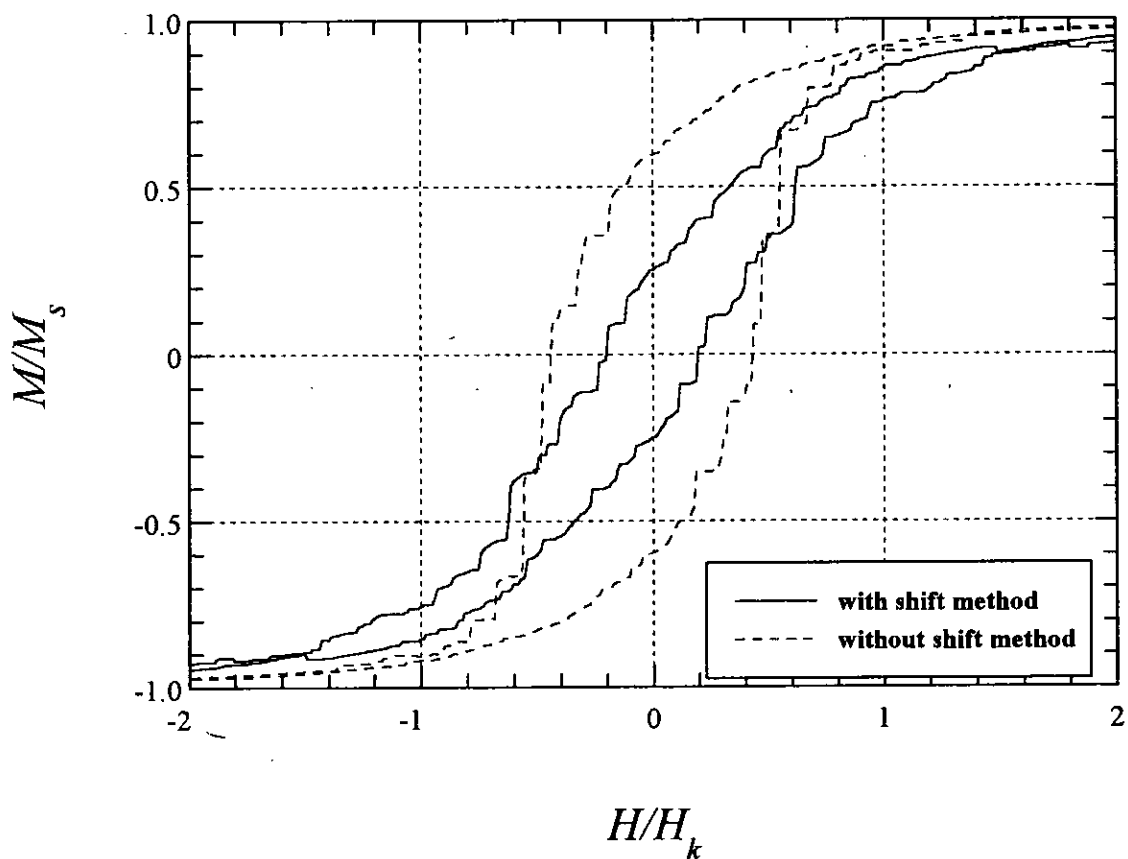


**Figure (5.30): Hysteresis loops illustrating the effects when using the shift method**

The inclusion of not only the exact calculation but also the problem triangles has been shown in this study to make a significant difference to the coercivity and remanence values. The exact calculation has turned out not to be as exact as expected and clearly future work would involve finding a more accurate way of incorporating the problem triangles.

### 5.5.5 Investigating $h^*$ and $h_{int}$

The last study in dealing with the magnetostatic calculation was to observe the effects on the hysteresis loops when both  $h^*$  and  $h_{int}$  were varied. Since the inclusion of the exact calculation, the value of 0.03 for  $h_{int}$ , and thus  $h^*$ , appeared to be too high. This could be explained by noting that the effect of exact calculation was much stronger than the dipole calculation. Therefore only a relatively small value was needed to observe its effects on the system. As already stated, a value of 0.01 was used in the previous studies. Values in the range of  $[0, 0.01]$  were studied and the hysteresis loops can be seen in Figure (5.31).

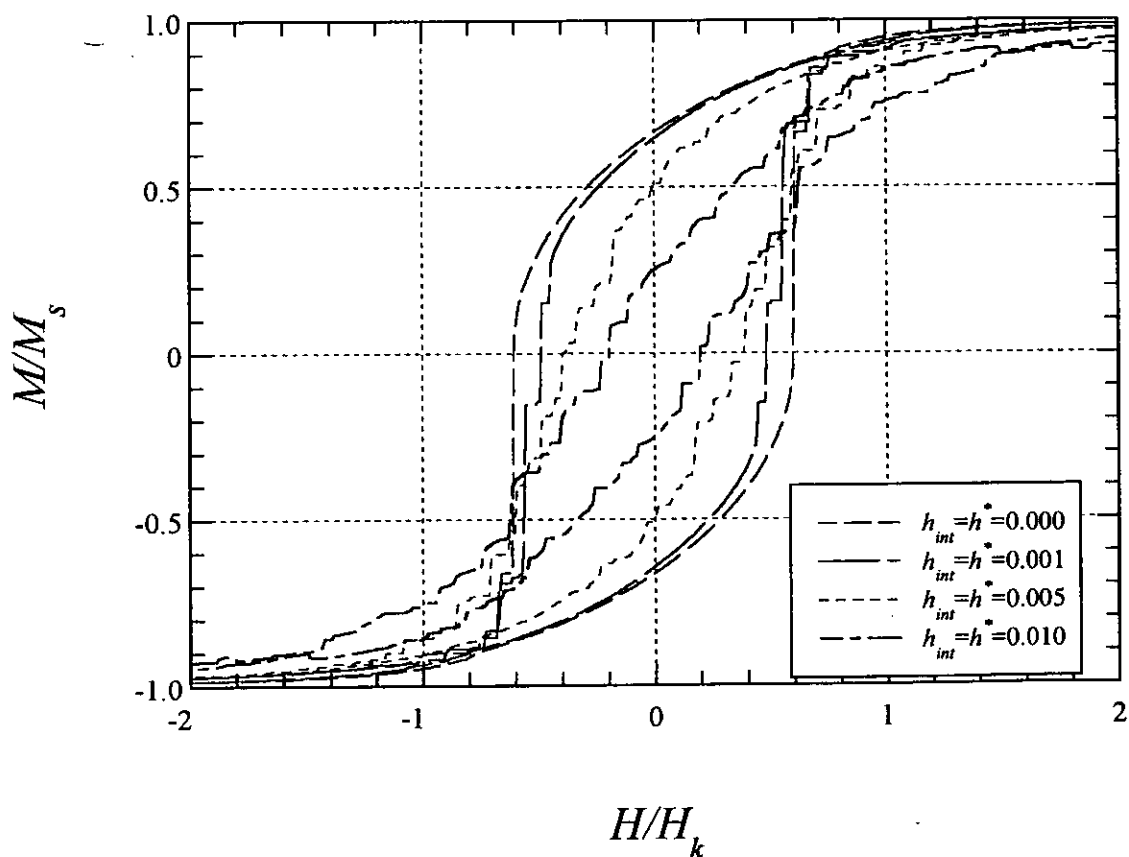


Figure (5.31): Hysteresis loops illustrating the effects on varying  $h^*$  and  $h_{int}$

There appears to be a significant reduction in both the remanence and coercivity values as the strength of the magnetostatic effects,  $h_{int}$  and  $h^*$ , was increased. This was not as

observed when using only the dipole calculation as an approximation for the magnetostatic field. The results obtained here, however, compare favourably with previous models (Tako, thesis; Zhu and Bertram, 1988).

Figures (5.32) and (5.33) show the arrow plots taken at remanence and coercivity. The first point to note in both cases is the length of the arrows. The length represents the average magnitude of the triangles within each of the grains. With the introduction of the exact calculation the overall average magnetisation within the grains appears to be smaller than previously observed with just the dipole approximation. This may be due to some cancellation of magnetisation between the triangles within the grain. Demagnetising effects may be apparent within the grains whereas previously they were seen over several grains in the form of vortices. At remanence, Figure (5.32), there appears to be no remaining evidence of the external field having been applied. In the previous plots a ripple structure was seen in the direction of the applied field. The same pattern was seen at coercivity as shown in Figure (5.33). Previously there were vast differences in the arrow plots between the two states. In this case, the remanence was low, therefore close to zero magnetisation.

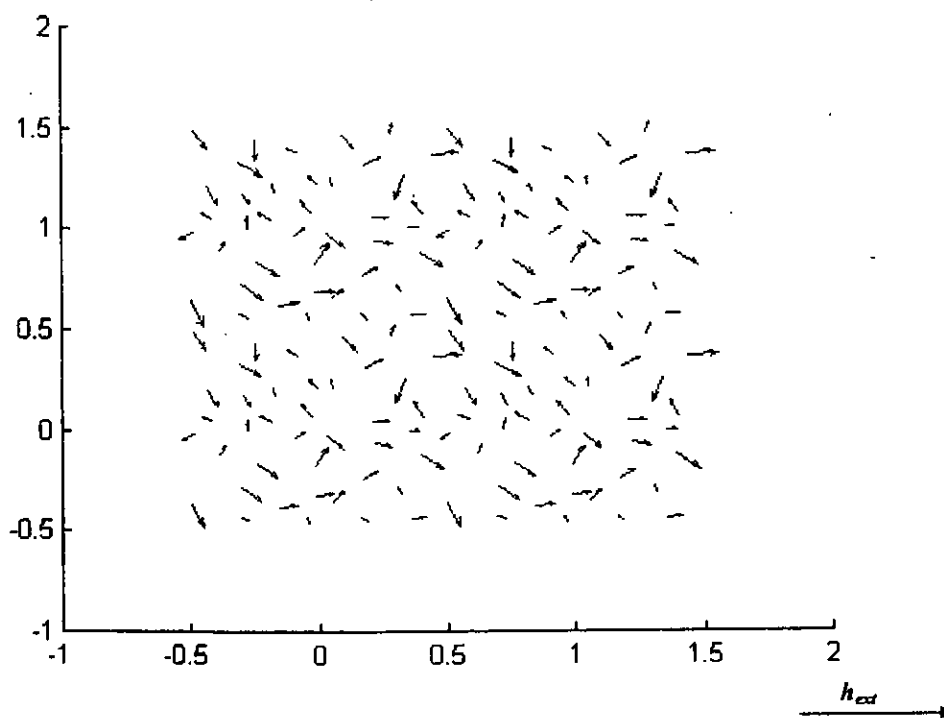
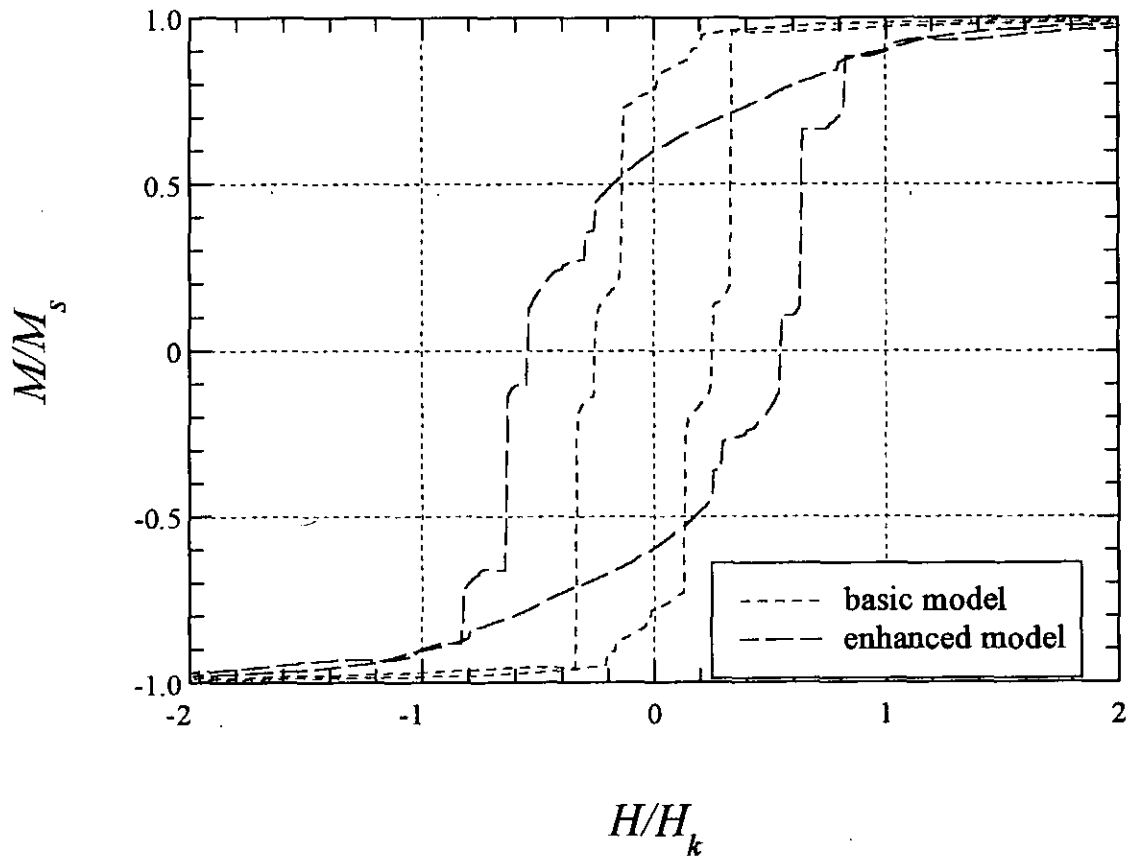


Figure (5.32): Arrow plot taken at remanence when  $h^* = h_{int} = 0.01$



exchange coupling between them. In the basic model the overall shape of the loop is more 'square'. This is very characteristic of a system dominated by exchange. The remanence is higher and close to the saturation value as the moments are kept well aligned. The coercivity is lower as more moments are switching coherently. The basic model appears to be dominated by exchange possibly as a result from the insufficient representation of the magnetostatic field by the dipole calculation.



**Figure (5.34): Hysteresis loops illustrating the differences between the basic and the enhanced model when all the interactions are included**

With the introduction of the exact calculation, the model behaviour compared well against other research findings when dealing with effect of the magnetostatic strength. When the exchange parameter,  $C_2^*$ , was investigated earlier using the basic model, the effects from increasing its value was opposite to what has been previously found. The same applied to strength of the magnetostatic effect and was amended by the introduction of the exact calculation. Therefore, the next step was to see the effects on

increasing  $C_2^*$  when using both the exact and dipole calculations to represent the magnetostatic field.

The effects on the remanence can be seen in Figure (5.35). The graph shows a significant increase in the remanence value as this parameter is introduced into the model and continues to increase steadily as  $C_2^*$  reaches a value of 0.4. The remanence value then decreases and increases as the parameter is increased further. However, the overall pattern appears to show a decrease in the remanence value for higher values of  $C_2^*$ . There were significant differences in the remanence values for increasing values of  $C_2^*$ . In the basic model, however, there appeared to be no significant differences in the remanence values with increasing  $C_2^*$ .

The effect on the coercivity as  $C_2^*$  is increased can be seen in Figure (5.36). There is an initial increase in the remanence value as  $C_2^*$  is introduced. The remanence then remains steady up to when  $C_2^* = 0.5$ . As  $C_2^*$  is increased further the remanence value decreases. These results appear to show more of a pattern than the results obtained from the basic model and favours the results found experimentally and from previous models (Nakai *et al.*, 1994; Tako, thesis; Zhu and Bertram, 1988)

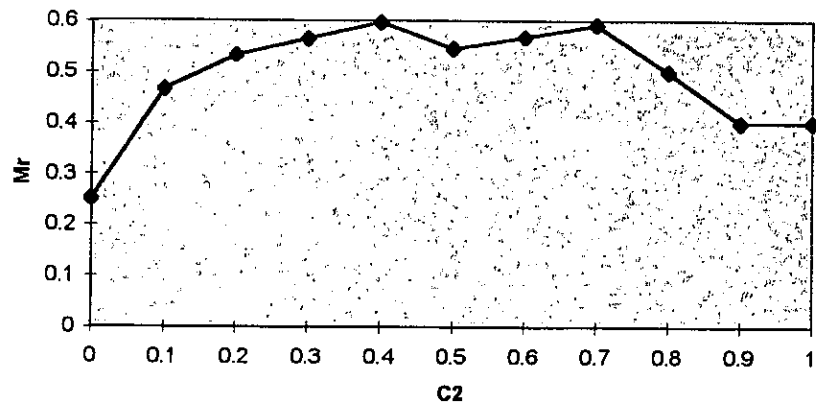
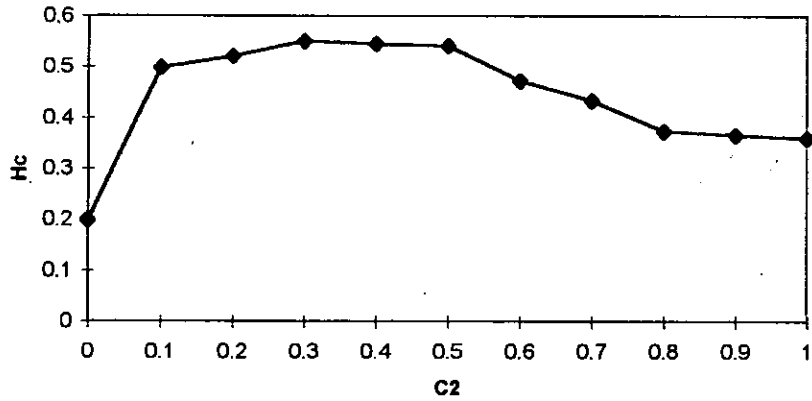
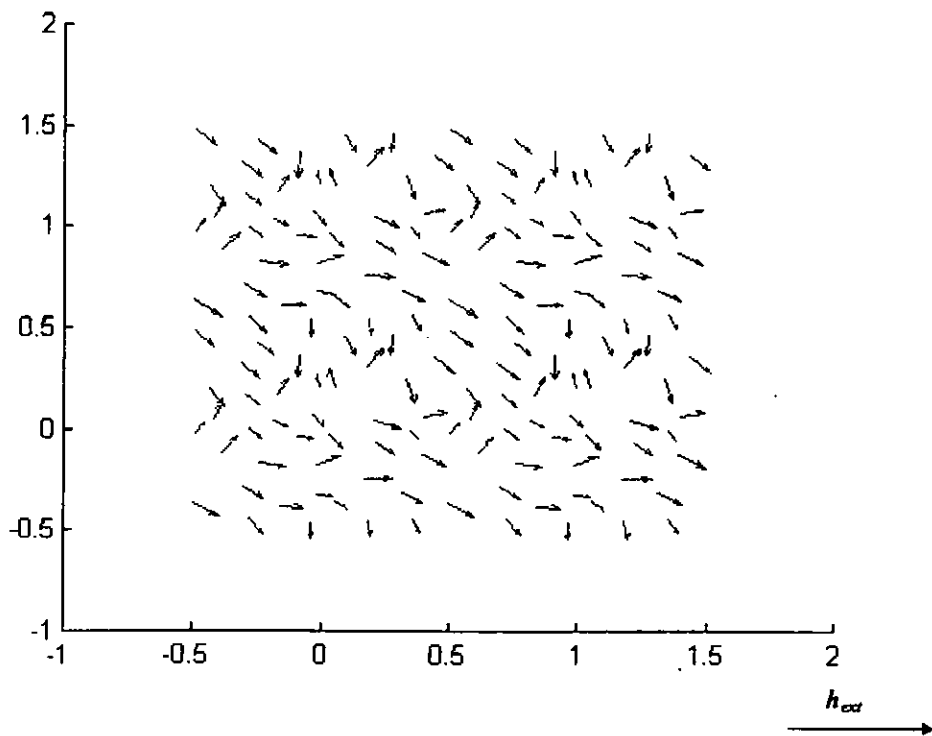


Figure (5.35): Graph to show the effect on the remanence as  $C_2^*$  is increased in the enhanced model



**Figure (5.36):** Graph to show the effect on the coercivity as  $C_2^*$  is increased in the enhanced model

Figures (5.37) and (5.38) show the arrow plots at remanence and coercivity for the enhanced model. The first point to note is the length of the arrows with respect to the previous model without exchange. The arrows are bigger and more in line with each other illustrating the exchange effects now present within the model.



**Figure (5.37):** Arrow plot taken at remanence when  $h^*=h_{int}^*=0.01$ ,  $C_1^*=0.02$  and  $C_2^*=0.4$

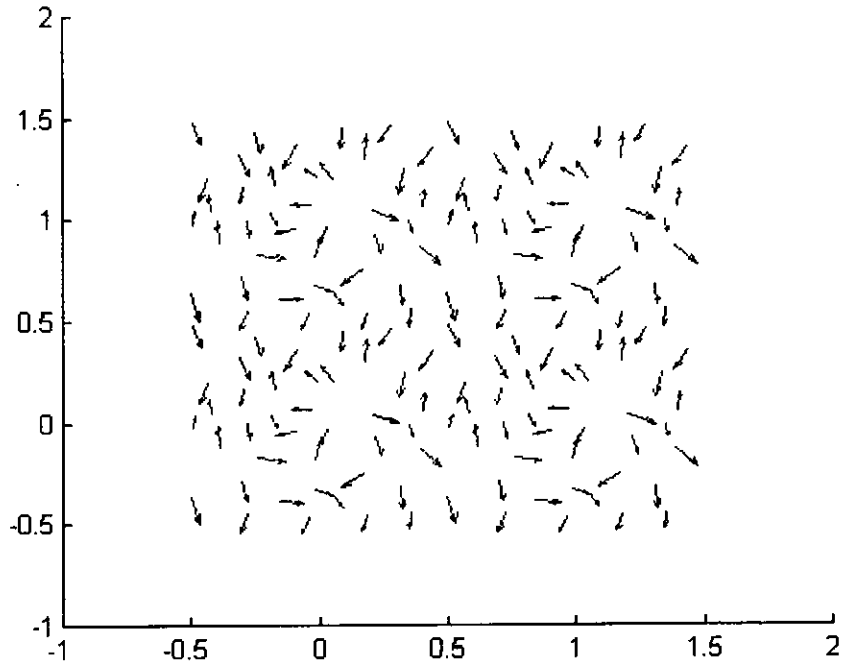


**Figure (5.38):** Arrow plot taken at coercivity when  $h^*=h_{int}=0.01$ ,  $C_1^*=0.02$  and  $C_2^*=0.4$

An enhanced model has been discussed and studied. A final comparison was made which introduced each of the interactions into the model as was observed with the basic model. The difference was the inclusion of the exact magnetostatic calculation. The hysteresis loops can be seen in Figure (5.39). The parameters for the enhanced model were set as:

anisotropy:	random easy axes
exact magnetostatic:	$r1=0.2$ and $h^*=0.01$
dipole approximation:	$r2=0.5$ and $h_{int}=0.01$
exchange:	$C_1^*=0.02$ and $C_2^*=0.4$

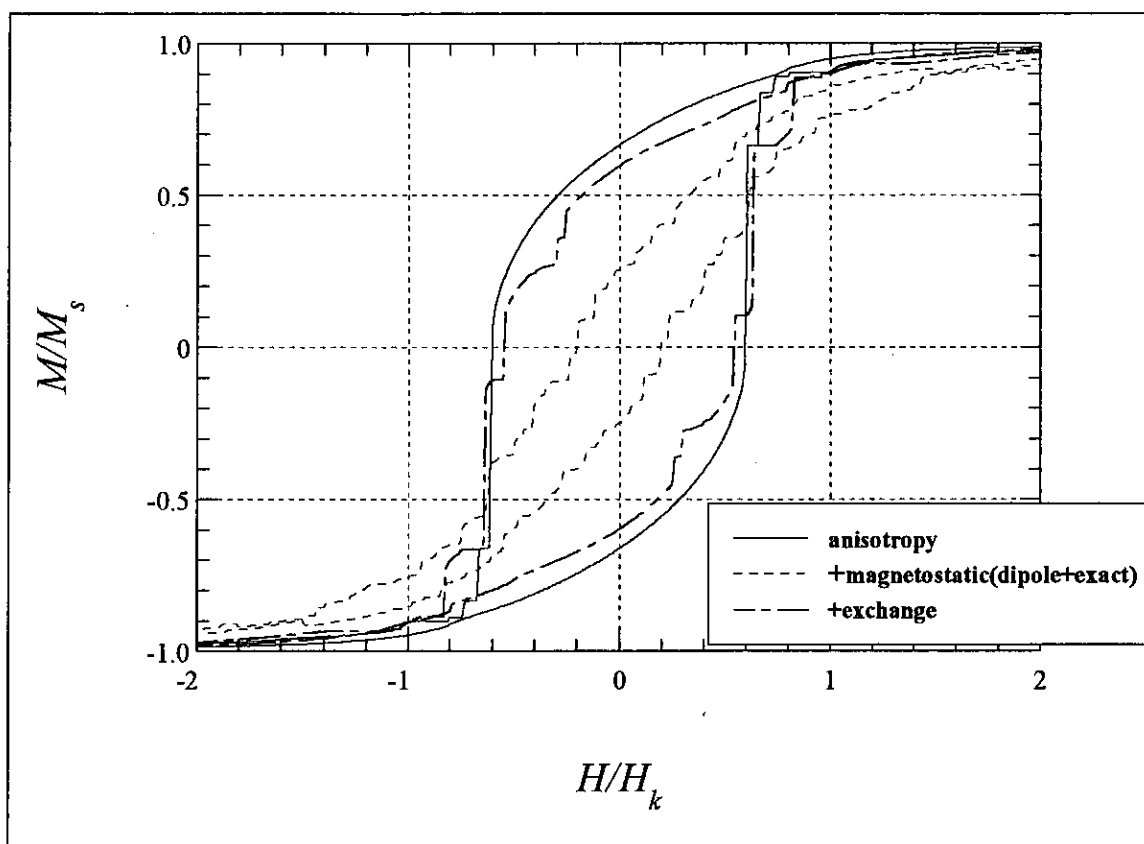


**Figure (5.39): The enhanced model**

When the magnetostatic effect was introduced both the remanence and the coercivity values decrease dramatically. This behaviour was due to the strong demagnetising effects present within the system. In this case the system wants to be in a demagnetised state at as low a field value as possible. The demagnetising effects can be seen at the start of the loop as the system was not fully saturated.

On the introduction of the exchange effects both the remanence and coercivity increase significantly. The shape of the loop illustrates the exchange effect. Large jumps can be seen representing regions of moments switching coherently. This is due to the exchange coupling present between them.

## 5.6 Summary

The results from the micromagnetic study have been presented. The main study was on the effects of the magnetostatic field calculation.

The inclusion of the exact calculation made a significant difference to the behaviour of the model. The effects of the close range magnetostatic effect was seen in the arrow plots. The magnitude of the magnetisation within the grain was small which suggested that flux closure occurred within the grain. In the basic model the magnetostatic effect was seen in the form of vortices across several grains. The results from the hysteresis loops also highlighted the differences between the models. The basic model showed more evidence of being dominated by exchange effects as remanence was higher and the shape of the loop was squarer. This could be due to insufficient representation of the magnetostatic effect. The enhanced model showed more evidence of being dominated by magnetostatic effects as the remanence was lower suggesting the need to reach a demagnetised state as early as possible.

The magnetostatic calculation is known to be the most time consuming but as the results from this study have shown, using just an approximate method can drastically effect the findings. It is therefore important to find a more accurate way of calculating the short range magnetostatic field. A relatively simple way has been presented here and no doubt its accuracy can be improved in further work.

## 6. Conclusions and Further Work

A two dimensional, micromagnetic model has been put forward to study the interaction effects on the magnetisation within the granular structure of thin films. The following is a summary of the work carried out in this thesis and possible ideas for future work.

The work in this study began by researching the material that was to be modelled, as discussed in Chapter 2. Its fundamental role in magnetic media was described together with the manufacturing process. It was also important to discuss the microstructure of thin films as a realistic model had to be simulated. Figure (2.3) showed the granular structure of a thin film observed via transmission electron microscopy (TEM). Early research into thin films modelled the structure as regularly shaped hexagons (Zhu and Bertram, 1988,1991). However, based on experimental findings as shown in Figure (2.3), recent micromagnetic models (Tako, thesis; Walmsley, thesis) have simulated irregular systems to obtain a more realistic representation of thin films. The model used in this study was based on the work by Tako who studied two dimensional thin film platelets. Chapter 2 also discussed the characteristics of thin film and introduced theories to enable the interpretation of the results obtained in Chapter 5.

The technique used to generate a model of the physical structure of the thin film was discussed in Chapter 3. The Voronoi Construction was used which generated the required irregular structure. The structure was made up of Voronoi polygons which were grown from randomly placed seed points within a 1x1 cell. Periodic boundary conditions were also applied which involved surrounding the main cell by eight replica cells. Early studies were based on a system of 15 grains, see Figure (3.3). Once the model was tested it was applied to a larger system of 40 grains, see Figure (3.4).

The magnetisation within each of the simulated grains was assumed to vary throughout. To achieve this, the polygons were divided into their natural triangles and the magnetisation within each triangle was assumed to vary linearly. A magnetic moment was associated with each seed point and vertex of the triangles. It was also assumed that

the grains were separated from each other by a boundary. This was to simulate the non-magnetic boundary found experimentally to lie between the magnetic grains.

Chapter 3 also discussed the micromagnetic concepts in order to understand the magnetic interactions which take place within a system of magnetic particles. Each magnetic moment within the system experienced effects from an externally applied field, anisotropy field, a magnetostatic and exchange field. The main work in this thesis was the interpretation of the magnetostatic field and was discussed in Chapter 4.

This field calculation is long range and therefore time consuming as it should include effects from all the moments within the system. Research into magnetostatic approximations is continuously being carried out in order to find more time and computer efficient models. Two approaches to modelling the magnetostatic field effect were put forward and were based on the model used by Tako. An approximation of the magnetostatic field calculation based on dipoles was discussed first. In order to calculate the magnetostatic field at any point in the system, an average of the moments on each vertex of the triangles was taken and located at the centroid of the corresponding triangles. The magnetostatic field at each moment due to the dipoles at the centroids of the triangles was calculated. Initially this approximation was used for triangles whose centroids lay within a given radius,  $r_2$ , from the point of evaluation.

A more accurate method of calculating the magnetostatic field based on surface and volume integrals was discussed. This was used to calculate the close range magnetostatic effects. The integrals, however, were found to have singularities when the point of evaluation lay on one of the vertices of a triangle to be integrated. The problem was overcome with the introduction of what was termed The Shift Method. It was a simple method which involved shifting the 'problem vertex' slightly away from the point of evaluation.

Chapter 4 discussed the results obtained from the study with the aid of hysteresis loops and arrow plots. The anisotropy effect was first studied and compared to the famous work carried out by Stoner and Wohlfarth (1991). The results from this model compared well to the previous findings. Different sets of random easy axes were also tested. They were found not to make any significant differences to the hysteresis loops.

The next study was on the effects from the magnetostatic field. The model which used the dipole approximation to calculate the total effect from the magnetostatic field was termed the basic model. The strength of this interaction was governed by the parameter  $h_{int}$ . The effects on the remanence and coercivity values were studied as  $h_{int}$  was increased. When a weak magnetostatic field interaction was introduced the remanence value increased and as  $h_{int}$  became stronger the remanence value remained at a constant value. The coercivity value, however, decreased on the introduction of a weak magnetostatic field interaction and then increased as  $h_{int}$  became stronger. The arrow plot taken at remanence showed a ripple structure which became more pronounced as  $h_{int}$  became stronger. At coercivity, the moments formed vortices which became stronger as  $h_{int}$  was increased. These findings compared well with the results obtained by Zhu and Bertram (1988).

The last interaction to be incorporated into the basic model was the exchange interaction. The effect of this interaction was to keep the moments in line with each other. This interaction had two parameters that governed its strength.  $C_1^*$  was associated with the strength of the exchange coupling within the grain and  $C_2^*$ , the strength of the exchange coupling across the grain boundaries. The effect of increasing  $C_1^*$  was studied first with respect to the remanence and coercivity values. There appeared to be no significant differences between the remanence values as this parameter was increased. The coercivity value, however, decreased initially and then remained at a steady value as the parameter was increased further.

The effects of  $C_2^*$  was then studied. As  $C_2^*$  was increased the remanence value increased slightly. There was an initial increase in the coercivity value as  $C_2^*$  was increased and then a sudden decrease to a steady value for higher values of  $C_2^*$ . This, however, did not agree with results found experimentally which suggest that coercivity should decrease as  $C_2^*$  is increased. The range of values studied for  $C_2^*$  was relatively broad. If the later part of the range was only observed, it could be said that the results did compare well to experimental findings.

The basic model had been studied and the effects on the hysteresis loops as each interaction was introduced was then observed. The remanence value increased as the

magnetostatic interaction was included and it increased further with the exchange interaction . The coercivity value decreased after the exchange interaction was included.

An enhanced approach to calculating the magnetostatic field within the system was then introduced and termed the exact calculation. It was based on volume and surface charges as used by Tako (thesis), but incorporated what was termed The Shift Method. This method was used on the problem triangles resulting from singularities discovered whilst using the exact calculation.

Initially the exchange interaction effect was removed from the model so that the magnetostatic effects were concentrated on. The exact calculation was incorporated to study the close range magnetostatic effects. The long range magnetostatic effects from the remaining triangles were approximated using the dipole calculation. The radius,  $r_1$ , containing the triangles contributing to the exact calculation was studied. As  $r_1$  was increased, the region using the dipole approximation decreased. The remanence and coercivity values decreased as more triangles contributed to the exact magnetostatic calculation. Vast differences between the basic and enhanced model were observed via hysteresis loops. The basic model had a higher remanence and coercivity value than the enhanced model and the shape appeared to be 'squarer'.

The difference between the two models was the calculation of the magnetostatic effects from the near neighbours. The long range magnetostatic effects were removed from the model and the near neighbour effects were calculated using the two models. Significant differences between the hysteresis loops were again observed. The study suggested that a more accurate close range magnetostatic calculation was required. The effects from the exact calculation were looked at more closely. The need for the inclusion of the problem triangles was observed by studying models with and without them. Again significant differences were observed between the two models and the problem triangles remained in the calculation.

The differences between the basic and enhanced model were also observed in the arrow plots. In the basic model, vortices were observed illustrating the strong magnetostatic effects over several grains. In the enhanced model, the magnitude of the magnetisation

within the grains was overall smaller. This illustrated the strong magnetostatic effects between the moments within the grains themselves.

The model suggested so far had contributions from an external field, anisotropy and both long and close range magnetostatic effects. The parameters that governed the magnetostatic effects were now  $h_{int}$  and  $h^*$  (exact calculation parameter) and were set equal in value. The effect on increasing the magnetostatic parameters was observed. The remanence and coercivity values were found decrease as the parameters increased. This illustrated the effect of the magnetostatic field on the system as it tried to achieved a demagnetised state.

The exchange effect was included in the enhanced model and compared to the basic model with exchange. In the enhanced model, the magnetostatic effects were calculated more accurately causing the remanence to be lower. The basic model appears to illustrate stronger exchange effects as the remanence was higher and the coercivity value was lower than observed in the enhanced model.

The work from this research study has been summarised. One point to note is that only one system of 40 grains was used in the simulation. Further work to the research presented in this thesis could involve applying the model to a different systems of 40 grains generated using the same technique. It has been found that the magnetic properties of thin films are affected by the microstructure of the film (Kojima *et al.*, 1995; Sato *et al.*, 1996). Micromagnetic models have studied and found differences between regular and irregular structures (Porter *et al.*, 1996; Walmsley *et al.*, 1999). Different sets of irregular structures could be compared to see if there was any significant differences in the hysteresis loops.

The model should also be applied to a larger system of say 100 grains, as 40 grains is still relatively small. The grains would be generated by randomly placing 100 seed points within a 1x1 cell and constructing Voronoi polygons around them as before. The grain size in the larger system would be smaller than in the system of 40. A detailed study between the effects of grain size on magnetic properties could be conducted. The only foreseeable problem with this increase would stem from the computer storage capability, especially when calculating the magnetostatic field.

Before considering any of the above, an improvement to the magnetostatic field should be developed. The results presented in this thesis have shown that there were vast differences between the two methods of calculating the magnetostatic field. When the exact calculation was incorporated in the model, it meant that fewer triangles were contributing to the dipole approximation. The region of  $r^2$  could be extended to 1 to include more triangles. Again, this may cause storage problems.

The main development from this research would be to find a more accurate solution to the problem discovered when using the exact calculation. The shift method was a basic technique and a more sophisticated and accurate method could be developed.

The question that should be asked now is whether it is viable to carry out further work on the 2D micromagnetic modelling of thin film media. Four years have passed since the start of this research and in that time the recording industry has been constantly changing.

One of the concerns of the industry is the physical limits on magnetic recording. The need to ever decrease the size of the bits has led to the problem of the superparamagnetic effect. This causes the moments in the material to spontaneously switch their orientation and effectively erasing the stored data. This problem has been discussed by O'Grady and Laidler (1999), Speliotis (1999) and White (2000). They all suggested that one way to overcome this problem was to return to perpendicular recording. In March 2000, Seagate Corporation (website) announced a storage density of  $45\text{Gb/in}^2$ . The media used for this achievement consisted of perpendicular, thin film multilayers.

To keep up with recent developments, the next step forward from the work carried out in this thesis would be to model a thin film multilayer. Research has shown that the films are composed of closely packed columns (Weir *et al.*, 1999). Micromagnetic models have been proposed by Zhu and Bertram (1988), Schrefl (1999) and Weir *et al.* (1999). In the model put forward by Schrefl, he uses the Voronoi Technique to simulate the grain structure of the media. The model by Weir *et al.* uses a model suggested by Zhu and Bertram (1988), where the media is represented by hexagonal columns.

The 2D model studied could be extended to a 3D model. Research into the magnetic interactions between the layers needs to be studied and incorporated into the model.

There is still the need to research into longitudinal thin films. The main reason is the economic factor which heavily influences the demand. A similar story could be told about flexible storage media since even with today's technology, tapes are still being used for backing up systems. Research is still being conducted on media such as MP tapes, for example.

The magnetic recording industry is constantly changing at an astonishing speed and no doubt within the next few years, new recording media will be available. With improved computer facilities, the micromagnetic modelling of such media will continue and contribute to the growth of the recording industry during this century.

# References

- A. Aharoni, "Magnetostatic Energy Calculation", *IEEE Trans. Magn.*, vol. 27, pp. 3539-3547, 1991.
- K. Atkinson, "Elementary Numerical Analysis", Wiley, 1993.
- T. C. Arnoldussen and L. L. Nunnolley, "Noise in Digital Magnetic Recording", World Scientific, 1992.
- G. Bertotti, "Hysteresis in Magnetism", Academic Press, 1998.
- W. F. Brown, "Approximate Calculation of Magnetostatic Energies", *J. Phys. Soc. Jap.*, vol. 17, sup. B-1, pp. 540-542, 1962.
- W. F. Brown, "Magnetostatic Principles in Ferromagnetism", North-Holland, Amsterdam, 1962.
- W. F. Brown, "Micromagnetics", Wiley-Interscience, New York, 1963.
- W. Chen, D. R. Fredkin and T. R. Koehler, "A New Finite Element Method in Micromagnetics", *IEEE Trans. Magn.*, vol. 29, no. 3, pp.2124-2128, 1994.
- R. W. J. Chia, C. C. Wang and J. J. K. Lee, "Effect of Adatom Mobity and Substrate Finish on Film Morphology and Porosity: Thin Chromium Film on Hard Disk", *J. Magn. Magn. Mater.*, vol. 209, pp. 45-49, 2000.
- S. Chikazumi, "Physics of Ferromagnetism", Oxford Science Publications, 1997.

G. Choe, S. J. Chung and R. M. Walser, "Correlation Between Grain Morphologies and Magnetic Properties of CoCrPt/Cr Thin Films", *Thin Solid Films*, vol. 259, pp. 231-236, 1995.

D. Craik, "Magnetism-Principles and Applications", Wiley, 1995.

B. D. Cullity, "Introduction to Magnetic Materials", Addison-Wesley, 1972.

C. Dean, "Micromagnetic Calculations of the Magnetic Properties of Thin Metallic Films", Ph. D. Thesis, University of Central Lancashire, 1993.

M. Futamo, N. Inaba, Y. Hirayama, K. Ito and Y. Honda, "Microstructure and Micromagnetics of Future Thin-Film Media", *J. Magn. Magn. Mater.*, vol. 193, pp. 36-43, 1999.

W. Gilbert, "De Magnete", (1600), Dover, 1958.

P. J. Grundy, "Thin Film Magnetic Recording Media", *J. Appl. Phys.*, vol. 31, pp. 2975-2990, 1998.

J. D. Hannay, N. S. Walmsley and R. W. Chantrell, "A Computational Model of Thermally Activated High Speed Magnetisation Reversal in Longitudinal Thin Film", *J. Magn. Magn. Mater.*, vol. 193, pp. 245-248, 1999.

D. Heerman, "Computer Simulation Methods in Theoretical Physics", Springer, 1990.

M. Imakawa, S. Ishibashi, M. Kuwabara, T. Shimatsu and M. Takahashi, "High Coercive Force and Low Intergranular Coupling in CoCrTa Thin-Film Recording Media Fabricated Under Ultra Clean Sputtering Process", *J. Magn. Magn. Mater.*, vol. 182, pp. 403-412, 1998.

J. P. Jakubovics, "Magnetism and Magnetic Materials", The Institute of Materials, 1994.

D. Jiles, "Magnetism and Magnetic Materials", Chapman and Hall, 1991.

G. E. Kay, "Three Dimensional Modelling of Metal Evapourated Tape", Ph. D. Thesis, University of Central Lancashire, 1999.

P. L. Kim, C. Lodder, N. H. Luong and T. D. Hien, "The Influence of Tantalum Content in Relation to Substrate Temperature on Magnetic and Structural Properties of Co-Cr-Ta Thin Films", *J. Magn. Magn. Mater.*, vol. 193, pp. 117-120, 1999.

T. R. Koehler and D. R. Fredkin, "Finite Element Methods For Micromagnetics", *IEEE Trans. Magn.*, vol. 28, no. 2, pp. 1239-1244, 1992.

S. Kojima, S. Fukaya, Y. Y. Yahisa, Y. Hosoe and N. Kodama, "Grain Size Effect on Noise Properties in CoCrTa Thin Film Media", *IEEE Trans. Magn.*, vol. 31, no. 6, pp. 2830-2832, 1995.

L. D. Landau and E. M. Lifschitz, "On the Theory of the Dispersion of Magnetic Permeability in Ferromagnetic Bodies", *Phys. Z. Sowjet.*, vol. 6, pp. 153-169, 1935.

P. Lu and S. Charap, "Angular Variation of Coercivity in Thin-Film Media by Micromagnetic Model", *IEEE Trans. Magn.*, vol. 28, no. 2, pp. 986-989, 1992.

J. C. Mallinson, "The Foundations of Magnetic Recording", Academic Press, 1993.

C. D. Mee and E. D. Daniel, "Magnetic Recording Volume 1:Technology", McGraw-Hill, 1987.

J. Nakai, E. Kusumoto, M. Kuwabara, T. Miyamoto, M. R. Visokay, K. Yoshikawa and K. Itayama, "Relation Between Microstructure of Grain Boundaries and the

Intergranular Exchange in CoCrTa Thin Film for Longitudinal Recording Media”, *IEEE Trans. Magn.*, vol. 30, no. 6, pp. 3969-3971, 1994.

K. O’Grady and H. Laidler, “The Limits to Magnetic Recording-Media Considerations”, *J. Magn. Magn. Mater.*, vol. 200, pp. 616-633, 1999.

A. Okabe, B. Boots, K. Sugihara, S. N. Chiu, M. Okabe, “Spatial Tessellations: Concepts and Applications of Voronoi Diagrams”, Wiley, 1992.

Y. Otani, H. Li, J. M. D. Coey, “Coercivity Mechanism of Melt-Spun Sm(Fe<sub>11</sub>Ti)”, *IEEE Trans. Magn.*, vol. 26, no. 3, pp. 2658-2660, 1990.

D. G. Porter, E. Glavinas, P. Dhagat, J. A. O’Sullivan, R. S. Indeck and M. W. Muller, “Irregular Grain Structure in Micromagnetic Simulation”, *J. Appl. Phys.*, vol. 79, pp. 4695-4697, 1996.

H. J. Richter, “Recent Advances in the Recording Physics of Thin Film Media”, *J. Appl. Phys.*, vol. 32, pp. R147-R168, 1999.

I. L. Sanders, T. Yogi, J. K. Howard, S. E. Lambert, G. L. Gorman and C. Hwang, “Magnetic and Recording Characteristics of Very Thin Metal-Film Media”, *IEEE Trans. Magn.*, vol. 25, no. 5, pp. 3869-3871, 1989.

H. Sato, A. Kikuchi, J. Nakai, H. Mitsuya, T. Shimatsu and M. Takahashi, “Effects of Grain Size and Intergranular Coupling on Recording Characteristics in CoCrTa Media”, *IEEE Trans. Magn.*, vol. 32, no. 5, pp. 3596-3598, 1996.

M. E. Schabes, “Micromagnetics of Small Ferromagnetic Particles”, Ph. D. Thesis, University of California, 1989.

M. E. Schabes, “Micromagnetic Theory of Non-Uniform Magnetisation Processes in Magnetic Recording Particles”, *J. Magn. Magn. Mater.*, vol. 95, pp. 249-288, 1991.

T. Schrefl and J. Fidler, "Numerical Simulation of Magnetisation Reversal in Hard Magnetic Materials Using Finite Element Method", *J. Magn. Magn. Mater.*, vol. 111, pp. 105-114, 1992.

T. Schrefl, "Finite Elements in Numerical Micromagnetics Part I: Granular Hard Magnets", *J. Magn. Magn. Mater.*, vol. 207, pp. 45-65, 1999.

Seagate Corporation, [www.seagate.com](http://www.seagate.com)

D. E. Speliotis, "Magnetic Recording Beyond the First 100 Years", *J. Magn. Magn. Mater.*, vol. 193, pp. 29-35, 1999.

E. C. Stoner, F. R. S. and E. P. Wohlfarth, "A Mechanism of Magnetic Hysteresis in Heterogeneous Alloys", *IEEE Trans. Magn.*, vol. 27, no. 4, pp. 3475-3517, 1991.

H. Suzuki, P. R. Bissell, R. W. Chantrell and N. Kodama, "Magnetisation Processes in Sputtered Co-Cr-Ta Thin Films Prepared by Transfer Deposition", *J. Magn. Magn. Mater.*, vol. 146, pp. 267-272, 1995.

M. Takahasahi and H. Shoji, "Physics of High Density Recording Thin Media Established by Ultra Clean Sputtering Process", *J. Magn. Magn. Mater.*, vol. 193, pp. 44-51, 1999.

K. M. Tako, "Micromagnetic Simulation of Polycrystalline 2-D Thin Films Using The Finite Element Method", Ph. D. Thesis, University of Keele, 1997.

R. S. Tebble, "Magnetic Domains", Methuen and Co. Ltd., 1969.

C. Tsai, J. Liang, H. H. Liang and C. M. Wang, "Sputtering Parameters Affecting the Corrosion Resistance of CoCrPtTa Thin Film Media", *J. Magn. Magn. Mater.*, vol. 209, pp. 157-159, 2000.

R. M. D. Vecchio, R. S. Hebbert and L. J. Schwee, "Micromagnetics Calculation for Two-Dimensional Thin-Film Geometries Using a Finite-Element Formulation", *IEEE Trans. Magn.*, vol. 25, no. 5, pp. 4322-4329, 1989.

R. H. Victora, "Quantitative Theory for Hysteretic Phenomina in CoNi Magnetic Thin Films", *Phys. Rev. Lett.*, vol. 58, pp. 1788-1791, 1987.

N. S. Walmsley, "Theoretical Studies of Stray Field Images of Magnetic Systems", Ph. D. Thesis, University of Central Lancashire, 1995.

N. S. Walmsley, R. W. Chantrell and J. J. Miles, "Microstructural Effects in Computer Simulations of the Magnetic and Recording Properties of Thin Film Media", *J. Magn. Magn. Mater.*, vol. 193, pp. 196-203, 1999.

I. S. Weir, J. N. Chapman, I. S. Molchanov, D. M. Titterington and J. Rose, "Observation and Modelling of Magnetisation Reversal in Multilayers Supporting Perpendicular Magnetisation", *J. Phys. D. Appl. Phys.*, vol. 32, no. 4, pp. 395-403, 1999.

P. Weiss, "La Variation du Ferromagnetisme avec la Temperature", *Compt. Rend.*, vol. 143, pp 1136-1139, 1906.

R. L. White, "The Physical Boundaries to High-Density Magnetic Recording", *J. Magn. Magn. Mater.*, vol. 209, pp. 1-5, 2000.

J. Zhu and H. N. Bertram, "Micromagnetic Studies of Thin Metallic Films", *J. Appl. Phys.*, vol.63, pp. 3248-3253, 1988.

J. Zhu and H. N. Bertram, "Magnetisation Reversal in CoCr Perpendicular Thin Films", *J. Appl. Phys.*, vol. 66, no. 3, pp. 1291-1307, 1989.

J. Zhu and H. N. Bertram, "Magnetisation Structures in Thin Film Recording Media",  
*IEEE Trans. Magn.*, vol. 27, no. 4, pp. 3553-3562, 1991.